Doctoral Dissertation

Averaging Methods and More Realistic Numerical Models Applied to Parametric Ship Roll

Masahiro Sakai

December 2018

Graduate School of Engineering,
Osaka University

CONTENTS

CHAPTER 1 INTRODUCTION 1

1.1 Introduction 1
1.2 Social Background 2
1.3 Preceding Researches 3
1.4 Aim and Composition of This Dissertation 6

CHAPTER 2 AVERAGING METHOD 8

2.1 Introduction 8
2.2 General Application of Averaging Method 9
2.2.1 Stability of Solutions 10
2.3 Governing Equation of Parametric Roll in Regular Waves 11
2.4 Parametric Roll in Regular Longitudinal Waves 12
2.4.1 Estimation Method proposed by Umeda et al. 12
2.4.2 Effect of Superharmonics 14
2.4.3 Effect of Approximation of Calm-Water GZ Curve 21
2.4.4 Effect of Vertical Motions 27
2.5 Application to Design Criteria 38
2.5.1 Parametric Roll in Irregular Waves 38
2.5.1.1 Grim's Effective Wave Concept 38
2.5.2 Estimation of Critical Ship Speed 39
2.5.2.1 Derivatives of Coefficients 42
2.5.3 Effect of Wave Encounter Frequency 43
2.6 Conclusions 48

CHAPTER 3 LOW SPEED MODEL 49

3.1 Introduction 49
3.2 Mathematical Model 49
3.3 Modeling of External Forces 50
3.3.1 Buoyancy and Froude Krylov Forces 51
3.3.2 Radiation and Diffraction Forces 51
3.3.3 Estimation of Roll Damping 54
3.3.4 Manoeuvring Hull and Rudder Forces 54
3.4 Model Experiment 56
3.5 Validation 59
3.6 Conclusions 64

CHAPTER 4 EFFECT OF ENCOUNTER FREQUENCY 66
4.1 Introduction 66
4.2 2:*n* Parametric Roll Region 67
4.3 Mathematical Model 70
4.4 Modelling of External Forces 70
4.4.1 Wave Induced Forces 71
4.4.2 Manoeuvring Hull and Rudder Forces 75
4.4.3 Thrust and Ship Resistance 76
4.5 Model Experiment 76
4.5.1 Roll Decay with Advance Speed 76
4.5.2 Speed Trial Test 79
4.5.3 Free Running Experiment 81
4.6 Ship Roll Response in Following Waves 86
4.6.1 Parametric Roll Region by the Nonlinear Mathieu Equation 86
4.6.2 Pure Loss of Stability Region by 4-degree-of-freedom Model 86
4.7 Conclusions 89

CHAPTER 5 CONCLUSIONS 90

ACKNOWLEDGEMENTS 92

APPENDIX SUBJECT SHIPS 93
A.1 Introduction 93
A.2 C11-Class Post-Panamax Container Ship 93
A.3 ITTC A-1 Container Ship 95
A.4 ONR Flare Topside Vessel 97
A.5 Pure Car Carrier 98

REFERENCE LIST 101

AUTHOR'S PAPER RELATED TO THIS DISSERTATION 107

CHAPTER 1 INTRODUCTION

1.1 Introduction

Supported by the continuous development of the global economy, the maritime trade volume grew from 2010 through 2017 and occupied more than 80% of the global trade volume in 2017 (United Nations Conference on Trade and Development, 2018). Hence, a ship still has a key role on the global economy. A ship is a vehicle that transports cargos and passengers by running on water surface. Hence, in case that a ship sinks, lives of crews and passengers may be lost. Although the number of ship losses is in decreasing trend in these years, 94 ships were still lost in 2017. 65% of the losses were due to sinking, and the rest 35% consists of grounding, fire, machinery damage, collision, and hull damage (Lloyd's Register, 2018). Since sinking of a ship is often driven by a water ingress or cargo shifting, large roll can be a trigger of sinking. No need to sink, large roll leads to damage or loss of cargos, so that large roll should be also prevented from the view point of economy and ecology. Then, the author focused on ship intact stability, especially on parametric roll, in this dissertation. This is because accidents related to parametric roll of merchant ships are still reported even in recent years (France et al., 2003; Hua et al., 2006; Danish Maritime Accident Investigation Board, 2014).

Ship intact stability treats large roll motion of intact ships. Metacentric height (GM), which is a basic index of ship stability, is mainly considered in the early design stage. GM is a linear slope of restoring moment against heel, so that it represents ship stability in her upright condition. GM can provide sufficient stability assessment when ship roll motion can be regarded as small, and the ship roll motion is enough small under usual weather conditions. However, ship stability inspection requires accurate estimation of heavy roll even if it hardly occurs because it must be based on probability or risk of casualty. In this case, nonlinear effects on ship motion are no longer negligible.

There are various critical roll motions of intact ships in waves. They can be categorized into four groups by a wave encounter frequency and wave direction. Well-known critical roll motions are categorized into the four groups as Tab. 1.1.1. The roll motions are briefly explained as an introduction to this dissertation of nonlinear roll motion. First, synchronous roll is a roll with the same frequency as the wave encounter one. Forcing with a frequency near the ship natural roll one excites heavy roll motion. Second, parametric roll is excited by periodic variation of restoring coefficients due to incident waves and ship vertical motions. Parametric roll with a frequency that is half the wave encounter one is likely to occur in longitudinal waves. Third, pure-loss of stability is a large roll caused by a small restoring moment at wave crests. Last, broaching-to is a large roll caused by abrupt yawing due to loss of manoeuvability after surf-riding. Third and last one happen only when a ship runs at high speed in following waves whose length is comparable to the ship length. Most critical roll motions in longitudinal waves were considered to happen only to small ships such as a fishing vessel. However, such accidents on larger ships were recently reported, and the threat of longitudinal waves are getting revealed (France et al., 2003; Hua et al., 2006; Danish Maritime Accident Investigation Board, 2014). This study mainly focuses on parametric roll in longitudinal

and quartering waves due to periodic variation of restoring coefficients.

Table 1.1.1 Categories of well-known roll modes.

		encounter frequency	
		comparable to a ship natural roll frequency	low
wave direction	beam waves	synchronous roll parametric roll	-
	longitudinal waves	parametric roll	pure-loss of stability broaching-to

1.2 Social Background

Parametric roll has long been known, and pioneering studies of parametric roll can be found in the literature (Watanabe, 1934; Kerwin, 1955). Watanabe (1934) showed that parametric roll is an unstable phenomenon in the Mathieu equation caused by GM variation due to incident longitudinal waves. Kerwin (1955) showed that the Mathieu equation with nonlinear damping can explain a finite amplitude of parametric roll. Moreover, He experimentally presumed that parametric roll rarely occurs in actual seas by using a fishing vessel. So, researchers of ship stability had regarded parametric roll as just a theoretical phenomenon. In the latter half of the 20th century, new-type of cargo ships were invented for more superior economy. This led to specialization and increasing size of cargo ships. In 1970s, Japanese researchers started focusing on intact stability problem under operational condition. Kan (1990) conducted free running model experiments with a container ship in following and quartering waves and pointed out that dangerous roll in following waves were mainly caused by pure loss of stability. Umeda et al. (1995a) also conducted free running model experiment and confirmed that the modern container ship could suffer parametric roll in short-crested irregular waves even when she complied with the Intact Stability Code of the International Maritime Organization (IMO). In 1998, a C11-class post-Panamax container ship suffered heavy roll with amplitude of over 40° under heave-to condition in actual sea. France et al. concluded that the accident was caused by parametric roll at the Society of Naval Architects and Marine Engineers (SNAME) annual meeting in 2001 (France et al., 2003). After the accident was revealed, accidents due to parametric roll started being reported for container ships and car careers. For example, Hua et al. (2006) reported that a pure truck and car career suffered parametric roll of about 50° in 2003, and Danish Maritime Accident Investigation Board (2014) reported that a 346.98 m-long container ship suffered parametric roll of 41° in 2014. Ikeda et al. (2013, p.133) supposed that no one simply had not been able to judge as parametric roll before the first report and there had been many accidents due to parametric roll.

Accidents due to parametric roll on recently-investigated ships forced the IMO to start developing the second generation intact stability criteria for critical roll motions including parametric roll in 2002. The existing intact stability criteria is based on statistical information of old ships that were built before 1950s. This means that the existing criteria might not always assess stability of recently-

investigated ships. Hence, in order to properly assess any ships, the new criteria should be based on physics. Since too complicated criteria shall hinder development of shipbuilding, the new criteria consists of three levels. The lower levels are simple but require enough safety margin. In contrast, the higher levels have lower safety margin but require more complicated procedure.

1.3 Preceding Researches

Parametric roll has long been discussed in the context of ship stability. There are pioneering studies of parametric roll in the literature (Watanabe, 1934; Grim, 1952; Kerwin, 1955; Paulling 1959; Ogawara & Miura, 1960). Watanabe (1934) focused on the fact that GM decreases due to trim or variation of relative wave elevation in longitudinal waves and a ship sometimes loses her stability. He proved that the instability is not a statistic one due to decrease of GM but a dynamical one due to periodic variation of GM by using stability criterion of the Mathieu equation with various parameters. Grim (1952) experimentally investigated a roll instability in regular longitudinal waves. Kerwin (1955) treated parametric roll as a phenomenon that appears in unstable region of the Mathieu equation as well. He showed that the Mathieu equation with nonlinear damping can estimate parametric roll with its finite amplitude. Furthermore, he conducted model experiment with a fishing vessel and confirmed that she easily suffers from parametric roll with an amplitude of 30° or more in regular waves. However, he finally presumed that parametric roll is not real threat in actual seas because the unstable region was very narrow and the growth of parametric roll required longer time. Paulling (1959) focused on GM variation due to heave and conducted forced-heave model experiment in calm water. He confirmed that the parametric roll due to heave can be qualitatively explained as an unstable phenomenon in an unstable region of the Mathieu equation. Ogawara and Miura (1960) also conducted model experiment with constant heel and observed parametric roll when the natural roll frequency divided by half the wave encounter frequency is near n (2:n parametric roll, where n = 1, 2, 3,…). Moreover, they confirmed that parametric roll amplitude in the experiment is well estimated by the nonlinear Mathieu equation proposed by Kerwin (1955) with experimentally obtained GM variation.

In 1970s, researchers focused on physics-based intact stability criteria. Kobylinski (1975) and Krappinger (1975) stated that the stability criteria have to separately manage various capsizing scenarios based on physics. Paulling et al. (1972) conducted model experiment in severe irregular waves in San Francisco bay and observed capsizing of the ship model. They grouped the capsizing scenarios into three modes: parametric roll, pure-loss of stability, and broaching-to. Moreover, they concluded that the vulnerability should be examined by the occurrence probability of critical waves. Based on these concepts, the second generation intact stability criteria are divided into five major scenarios of ship accidents (parametric roll, pure loss of stability, broaching-to, dead ship, and excessive acceleration) and the vulnerability in the level 2 of the new intact stability criteria is judged by using wave occurrence probability. In order to deal with probability of capsizing due to parametric roll, dynamic instability of ship roll motion started being investigated with more realistic approaches. Abicht (1975) addressed parametric roll in irregular longitudinal waves, proposed a way to convert irregular longitudinal waves to regular waves, and showed that the stability in irregular longitudinal waves can be estimated by the Mathieu equation. The reason why the conversion was

used was because general statistical method, in other words superposition of waves, cannot be applied to GM variation in longitudinal waves, although it can be applied to roll in irregular beam waves. Blocki (1980) estimated probability of capsizing due to parametric roll in irregular waves based on Y. Goda's wave group model. He conducted model experiment with cylindrical model in regular beam waves and observed capsizing due to parametric roll. The time series of capsizing due to parametric roll were well estimated by using the nonlinear Mathieu equation with cubic damping and restoring moment. In the calculation, the GM variation was induced by heave that was estimated based on a linear theory independently of roll.

Although nonlinear terms had been taken into account to estimate parametric roll amplitude in aforementioned studies and simple nonlinearities, such as fold bifurcation or jump phenomenon, had been already known (e.g. Bhattacharyya, 1978), nonlinear-dynamical ideas and approaches were introduced to the field of ship stability by Cardo et al. (1980; 1981; 1984) and Nayfeh and Khdeir (1986a; 1986b). Cardo et al. (1980; 1981; 1984) investigated damping effect on the steady-state nonlinear roll response in regular beam waves, such as subharmonics and superharmonics (or ultraharmonics), by applying approximately-analytical methods called a harmonic-balance method, averaging method, and multiple-scales method. Nayfeh and Khdeir (1986a; 1986b) intensively investigated nonlinear dynamical structure of roll motion in regular beam waves and found the nonlinear behaviors, such as jumps, subharmonics, superharmonics (ultraharmonics), loss of symmetry, period doubling, and chaos. Further, they applied a multiple-scales method to estimate approximate steady-state roll response. These ideas and approaches are also employed to estimate parametric roll. Sanchez and Nayfeh (1990a) used the nonlinear Mathieu equation with cubic damping and quintic restoring and applied second-order multiple scales method to the nonlinear ordinary differential equation in order to obtain approximate analytical periodic orbits. The response of the roll equation was well investigated by using nonlinear dynamical approaches and found many nonlinear behaviors, such as jump, loss of symmetry, period-doubling, chaos, and capsizing. They showed that when chaotic response that comes after infinite times of period-doubling loses its stability, the ship capsizes if her upright is unstable and the ship settles to upright if her upright is stable. Soliman and Thompson (1992) investigated the indeterminate subcritical bifurcations. Here, indeterminate means that the steady state to which the ship settles after subcritical pitchfork bifurcation cannot be determined because of fractal boundaries in the Poincare map of the phase plane. They revealed that the fractal boundaries is associated with a heteroclinic bifurcation in the phase plane between a saddle type unstable parametric roll and vanishing stability point of the GZ curve. Umeda et al. (2004) applied these nonlinear dynamical approaches to the uncoupled roll model with a more realistic restoring moment in waves. They found the similar nonlinear behaviors, such as jump, loss of symmetry, period-doubling, chaos, and capsizing.

The contributions related to the nonlinear dynamics suggested that very complex behaviors appears even in a simple single-degree-of-freedom (1-dof) model. The complexity shall confuse users of the new physics-based stability criteria because almost all of them are not familiar with nonlinear dynamics. The approximate analytical methods provides results according to the assumed form of solutions and the magnitudes of results are expressed as algebraic equations. Hence, all possible solutions can be obtained by solving the algebraic equations and the solution includes only

what are expected. This characteristic is very useful for the new stability criteria because only desired solutions are obtained without knowledge of nonlinear dynamics. For this reason, realistic roll models and their approximate analytical solutions are proposed (Umeda et al., 2004; Bulian, 2004). The method of Umeda et al. is used in the draft second check of the second generation intact stability criteria for parametric roll. In the draft, the ship vulnerability is judged based on dangerous wave occurrence probability and irregular waves are converted to a regular wave based on Grim's effective wave (Grim, 1961). Further, Maki et al. (2011) combined the approximate analytical solutions and wave stochastic theories, thereby estimating parametric roll in irregular waves.

Whereas researches based on uncoupled roll models are introduced in the above paragraphs, the researches aiming to investigate more precise response of parametric roll with multi-dof models are introduced in this paragraph. Hamamoto and Akiyoshi (1988) compared a 6-dof model based on the Froude Krylov assumption and a slender body theory and free running model experiment in regular following waves. Even though their calculation did not consider a diffraction effect, the calculated results showed good agreement with the experiment. de Kat and Paulling (1989) took diffraction forces into account and also showed good agreement with experimentally obtained roll motion. They focused on not only parametric roll but also pure loss of stability and broaching-to. Since parametric roll is caused by variation of restoring coefficients, estimation of the variation is much important to obtain accurate results. Boroday (1990) showed that the restoring variation can be precisely estimated by adding added mass terms based on a strip theory to the Froude Krylov forces by comparing calculation with a captive model experiment. Nowadays, almost all advanced simulation models for parametric roll take into account radiation and diffraction effects based on seakeeping theory. de Kat and Paulling (2001) proposed the 6-dof model FREDYN that estimates ship motion under wind and waves. For, the Froude Krylov force, the pressure is integrated over an instantaneous wetted surface. The radiation and diffraction forces are calculated based on a linear strip theory. Further, manoueuvring forces, rudder forces, propeller thrust, hull resistance, and wind forces are nonlinearly considered. Shin et al. (2003) described development and applications of the 6-dof model called LAMP (Large Amplitude Motion Program). In the model, the hydrodynamic forces related to waves are calculated based on a panel method, and the panel-based potential flow is solved over an instantaneous wetted hull surface. FREDYN and LAMP were developed to investigate ship dynamics on the ocean. On the other hand, Hashimoto and Umeda (2010) focused on only parametric roll in longitudinal waves and proposed a heave-roll-pitch coupled 3-dof model. The 3-dof model took radiation and diffraction effects as a function of an instantaneous heel angle into account. The results showed good agreement with towing model experiments. As a further improvement, Sadat-Hosseini et al. (2010) used CFD to estimate parametric roll and showed good agreement with free running model experiment. However, benchmark studies of parametric roll (Spanos & Papanikolaou, 2009; Reed, 2011) indicated that no simulation models could estimate parametric roll amplitude enough accurately under any situation.

Parametric roll can occur when a natural roll frequency ω_ϕ is almost equal to an integer multiple of half the encounter frequency ω_e, hence $\omega_e:\omega_\phi \approx 2:n$ (n is an integer.). This is estimated by using the Mathieu equation. In this dissertation, parametric roll in the Mathieu's unstable region of $\omega_e:\omega_\phi \approx 2:n$ is called 2:n parametric roll. Only the 2:1 parametric roll is often focused on mainly because the

Mathieu's unstable region decreases as n increases. Sanchez and Nayfeh (1990a) closely investigated the 2:1 and 2:2 parametric roll by using nonlinear dynamical approaches based on 1-dof roll model. Vilensky (1995) revealed that the 2:2 parametric roll is not so dangerous relative to the 2:1 parametric roll in purely following waves; however, the 2:2 parametric roll in stern quartering waves can cause a large roll motion due to the combination of the periodic GZ variation and direct exciting moment. Unfortunately, his study is not sufficiently accessible to the public. The 2:n parametric roll ($n > 2$), in other words, the higher advance speed region does not appear to have been investigated enough. Spyrou (2000) investigated the 2:1 and 2:2 parametric roll with different wave encounter frequencies by using the Mathieu-type nonlinear differential equation with a nonlinear roll damping. He defined very quick capsize events that occurred around a wave crest as a pure loss of stability. However, he mentioned that there was no practical reason to divide parametric roll and pure loss of stability. Moreover, Spyrou (2005) estimated that when n is greater than 2, 2:n parametric roll rarely happens mainly because the ship should run at high speed to achieve such a small encounter frequency and then the roll damping becomes too large to cause parametric roll. However, it is no more than a presumption based on the Mathieu-type equation.

As mentioned above, parametric roll has been investigated from various viewpoints. Simplified estimation models were sufficiently investigated by Umeda et al. (2004) and Bulian (2004). However, the estimation accuracy of intensive roll by the averaging method is sometimes insufficient due to absence of higher order effects in the model and averaging method. The method of Umeda et al. is used to estimate parametric roll amplitude in the draft second check of the second generation intact stability criteria for parametric roll. Since an averaging method yields an algebraic equation of amplitude, the algebraic equation may provide more useful information for the criteria than just an amplitude.

1.4 Aim and Composition of This Dissertation

This dissertation aims to: 1) estimate nonlinear response of parametric roll in regular waves by using averaging methods; 2) utilize simplified methods for the physics-based stability criteria against parametric roll; 3) estimate ship motions with low advance speed in regular oblique waves; 4) investigate qualitative transition of roll response in following waves.

In chapter 2, averaging methods are used to estimate nonlinear response of parametric roll with additional treatment of superharmonic components, actual GZ curve, and vertical motions. Moreover, the design criteria is considered by using the averaged equations (Umeda et al., 2004) and Grim's effective wave concept (Grim, 1961).

In chapter 3, a 5-dof model is proposed to estimate parametric roll in oblique waves. Since the C11-class post-Panamax container ship suffered parametric roll under a heave-to condition (France et al., 2003), the maoeuvrability when the ship speed is low is taken into account.

In chapter 4, effect of a wave encounter frequency on the roll response is investigated. Although parametric roll is known as a phenomenon that occurs in unstable regions of the Mathieu equation. The unstable regions cover a wide range of a wave encounter frequency because parametric roll might happen when $\omega_e:\omega_\phi \approx 2:n$. Here, ω_e is a wave encounter frequency, ω_ϕ is a ship natural roll

frequency, and n is a natural number. However, in the region of small wave encounter frequency, i.e. when a ship runs at high speed in following waves, pure loss of stability or broaching-to might happen.

In chapter 5, this dissertation is concluded with remarks.

CHAPTER 2 AVERAGING METHOD

2.1 Introduction

An averaging method is one of analytical approaches to estimate periodic orbits of nonlinear mechanics and is based on perturbation concept. It provides differential equations of parameters of the periodic orbits by assuming the parameters change slowly enough in time relative to the period of the solution. It is known as a strong method to obtain approximate periodic orbits of a weakly nonlinear system because it is widely applicable and the stability can be straightforwardly judged. The detailed procedures of an averaging method are available in sections 2.2. Averaging methods were proposed by researchers of celestial mechanics and Krylov and Bogoliubov established a general application of a first-order averaging method (Krylov & Bogoliubov, 1947). So, the first-order averaging method is sometimes called Krylov-Bogoliubov averaging method. Although there are other analytical approaches, such as a harmonic balance method and multiple scales method, the first-order solutions appear to be the same. On the other hand, the second- or higher-order solutions do not so. A harmonic balance method is based on a rather simple idea that the solutions can be expanded in Fourier series, so that higher-order approximate solutions can be easily obtained by the Galerkin-Urabe method (Urabe, 1965). However, this method does not provide differential equations of parameters, so that a variational equation should be derived to judge the stability of solutions. A multiple scales method provides the differential equations of parameters but the procedure is a little more complicated than an averaging method. By contrast, the higher-order solutions of multiple-scales method can be obtained a little more easily than that of an averaging method. These analytical approaches can provide all solutions as a set of algebraic equations. On the other hand, nonlinear differential equation can be solved nowadays by a numerical integration method, such as the Runge-Kutta method; however, it is known that a nonlinear differential system has various coexisting steady states, and a derived solution depends on initial values of numerical integration. Hence, theoretically speaking, obtaining all solutions by numerical integration requires to calculate for all possible initial values. This does not deny the efficiency of the numerical integration methods because they easily provide an accurate solution indeed. Similarly, an analytical approach has a drawback that they can provide only solutions having an assumed form of solutions. This means that analytical investigation requires rough knowledge of the global structure beforehand. These indicate the necessity of recognizing both the analytical and numerical approaches and combining them efficiently in order to know the nonlinear mechanics.

As shown in chapter 1, parametric roll is caused by a GM variation in waves and the GM varies due to variation of water plane area that is fluctuated by incident waves and vertical motions of a ship. Parametric roll has been known as an unstable phenomenon which occurs in an unstable region of the Mathieu equation since Watanabe (1934) was published. The steady state can be estimated by the Mathieu equation with nonlinear terms (Kerwin, 1955). Hence, nonlinear effects have to be taken into account in order to estimate parametric roll amplitude. However, since an exact solution of even single-degree-of-freedom (1-dof) ordinary differential equation has not been found yet, an approximate analytical approach or numerical integration method should be used. Moreover, since

multiple-dof model is too complicated to investigate a global response of parametric roll, 1-dof models have been widely used in field of ship stability.

Francescutto (2001) proposed to apply an averaging method to simple 1-dof parametric roll model. Umeda et al. (2004) applied an averaging method to a 1-dof parametric roll model with more realistic restoring moment in waves. Bulian (2004) introduced more complicated restoring variation into 1-dof model and applied an averaging method to the model. In this chapter, the equation proposed by Umeda et al. (2004) is mainly used because the equation was well validated by comparing with model experiments.

In section 2.2, a general application of an averaging method is introduced including stability of the solutions. In section 2.3, a 1-dof model for parametric roll is introduced. In section 2.4, parametric roll in regular longitudinal waves are discussed. In subsection 2.4.1, the method of Umeda et al. (2004) is introduced, which is based on a GM variation due to longitudinal waves, assuming that heave and pitch trace their static equilibria in the waves. In subsection 2.4.2, the necessity of superharmonic components to obtain more accurate solutions is shown. In subsection 2.4.3, how to reflect actual GZ curve in calm water is shown. In the previous methods (Francescutto, 2001; Umeda et al., 2004; Bulian, 2004), the calm-water GZ was approximated by polynomials to obtain algebraic equations of parametric roll amplitude, so that some information was lost at the process of polynomial fitting. In subsection 2.4.4, effect of vertical motions are taken into account and apply an averaging method because GM varies due to heave and pitch as well and, actually, heave and pitch change dynamically when a ship runs at low speed in longitudinal waves whose length is comparable to the ship length. In section 2.5, design criteria for parametric roll is discussed. Since the vulnerability have to treat parametric roll in irregular waves, Grim's effective wave concept (Grim, 1961), which is adopted in the draft second check of the second generation intact stability criteria (IMO, 2016), is introduced. In subsection 2.5.2, how to find the peak of parametric roll resonance by using the averaged equations (Umeda et al., 2004) is proposed. In subsection 2.5.3, the simplification on the wave encounter frequency in the draft second check is verified by using the mean encounter frequency of Grim's effective wave spectrum. Finally, the remarks o this chapter is concluded in section 2.6.

2.2 General Application of Averaging Method

The procedures of an averaging method are as follows (e.g. Sato, 1977). The averaging method is applied to a nonlinear differential equation that has a periodic solution and is expressed as Eq. 2.2.1:

$$\ddot{x} + x = \varepsilon f\left(x,\ \dot{x},\ t\right) \quad \left(0 < \varepsilon \ll 1\right). \tag{2.2.1}$$

Here, the function f in the right hand is periodic in time with a period 2π. Based on a general solution of Eq. 2.2.1 when ε is zero, the solution is assumed as following form in Eq. 2.2.2:

$$x = A\cos\left(t - \varphi\right), \quad \dot{x} = -A\sin\left(t - \varphi\right). \tag{2.2.2}$$

This is introduced by van der Pol (van der Pol, 1926) and is called "Van der Pol rotation transformation." This converts a problem of obtaining a periodic steady state of differential

equations into that of solving algebraic equations of the amplitude and phase of the assumed sinusoidal function. Applying the relationship of trigonometric functions to Eq. 2.2.2, we obtain

$$A^2 = x^2 + \dot{x}^2, \quad \tan(t-\varphi) = -\frac{\dot{x}}{x}. \tag{2.2.3}$$

Differentiating Eq. 2.2.3 with respect to *t*, we obtain

$$\dot{A} = \frac{\dot{x}}{A}(\ddot{x} + x), \quad \dot{\phi} = \frac{x}{A^2}(\ddot{x} + x). \tag{2.2.4}$$

Substituting Eq. 2.2.1 and 2.2.2 in Eq. 2.2.4, we obtain

$$\dot{A} = -\varepsilon \sin(t-\varphi)\, f\left(A\cos(t-\varphi), -A\sin(t-\varphi), t)\right), \tag{2.2.5}$$

$$\dot{\varphi} = \frac{\varepsilon}{A}\cos(t-\varphi)\; f\left(A\cos(t-\varphi), -A\sin(t-\varphi), t\right). \tag{2.2-6}$$

Assuming *A* and φ change slowly with time and averaging Eq. 2.2.5 and 2.2.6 over one period, we obtain

$$\begin{aligned}\dot{A} &= -\varepsilon \frac{1}{2\pi}\int_0^{2\pi} \sin(t-\varphi)\, f\left(A\cos(t-\varphi), -A\sin(t-\varphi), t)\right) dt \\ &= \varepsilon \Phi(A, \varphi),\end{aligned} \tag{2.2.7}$$

$$\begin{aligned}\dot{\phi} &= \frac{\varepsilon}{2\pi A}\int_0^{2\pi} \cos(t-\varphi)\; f\left(A\cos(t-\varphi), -A\sin(t-\varphi), t\right) dt \\ &= \varepsilon \psi(A, \varphi).\end{aligned} \tag{2.2.8}$$

Here, Eq. 2.2.7 and 2.2.8 are no longer nonautonomous dynamical system but autonomous dynamical system, which does not explicitly depend on time. They are called averaged equations. A steady state periodic solution is expressed as just an equilibrium point on (*A*, φ)-plane. The averaging method is very useful because we can easily check the stability of the steady state by using the Taylor expansion of the averaged equations around the equilibrium point. The procedure can be available in subsection 2.2.1.

2.2.1 Stability of Solutions

Stability of solution means an asymptotic behavior of a perturbation around the solution. The definition of Lyapunov stable (Hayashi, 1985), which means stable equilibrium of an autonomous dynamical system, is as follows: if for every $\varepsilon > 0$, there exists a $\delta > 0$ such that the orbit that starts form a point within a distance δ from the equilibrium point at $t = 0$ stays within a distance ε from the equilibrium point for every positive *t*. A Lyapunov stable point which tends to the equilibrium point when $t \to \infty$ is defined as asymptotically stable. Setting an equilibrium point of Eq. 2.2.7 and 2.2.8 as (A_0, φ_0), we obtain

$$\dot{A} = \varepsilon \Phi\left(A_0,\, \varphi_0\right) = 0\,, \tag{2.2.1.1}$$

$$\dot{\phi} = \varepsilon \psi\left(A_0,\, \varphi_0\right) = 0\,. \tag{2.2.1.2}$$

Giving a small enough perturbations (ξ, η) as Eq. 2.2.1.3:

$$\left(A,\, \varphi\right) = \left(A_0 + \xi,\, \varphi_0 + \eta\right), \tag{2.2.1.3}$$

we obtain variational equations as Eq. 2.2.1.4 and 2.2.1.5:

$$\dot{\xi} = \varepsilon \frac{\partial \Phi\left(A_0,\, \varphi_0\right)}{\partial A} \xi + \varepsilon \frac{\partial \Phi\left(A_0,\, \varphi_0\right)}{\partial \phi} \eta\,, \tag{2.2.1.4}$$

$$\dot{\eta} = \varepsilon \frac{\partial \Psi\left(A_0,\, \varphi_0\right)}{\partial A} \xi + \varepsilon \frac{\partial \Psi\left(A_0,\, \varphi_0\right)}{\partial \phi} \eta\,. \tag{2.2.1.5}$$

Using a matrix form, we obtain

$$\begin{Bmatrix} \dot{\xi} \\ \dot{\eta} \end{Bmatrix} = \varepsilon \begin{bmatrix} \dfrac{\partial \Phi\left(A_0,\, \varphi_0\right)}{\partial A} & \dfrac{\partial \Phi\left(A_0,\, \varphi_0\right)}{\partial \varphi} \\ \dfrac{\partial \Psi\left(A_0,\, \varphi_0\right)}{\partial A} & \dfrac{\partial \Psi\left(A_0,\, \varphi_0\right)}{\partial \varphi} \end{bmatrix} \begin{Bmatrix} \xi \\ \eta \end{Bmatrix}. \tag{2.2.1.6}$$

This is called the Jacobian matrix. The equilibrium point (A_0, φ_0) is asymptotically stable only when all eigenvalues of the matrix have a negative real part.

2.3 Governing Equation of Parametric Roll in Regular Waves

Since parametric roll is excited by a periodic variation of restoring coefficients, it is governed by nonautonomous dynamical system, which has terms that explicitly depends on the time. A 1-dof parametric roll model is expressed as Eq. 2.3.1:

$$\begin{aligned} &\ddot{\phi} + 2\alpha\left(\phi,\, \dot{\phi}\right)\dot{\phi} + \omega_\phi{}^2 \frac{GM_{vari}\left(t,\, \phi\right)}{GM} \phi \\ &\quad + \omega_\phi{}^2 \frac{GZ_{calm}\left(\phi\right)}{GM} = \zeta_a\, r\, k\, \omega_\phi{}^2 \sin\chi \sin\omega_e t\ . \end{aligned} \tag{2.3.1}$$

Here, ϕ is roll, α is a roll damping coefficient, and ω_ϕ and ω_e are a natural roll frequency and wave encounter frequency, respectively. The term GM is a metacentric height, GM_{vari} and GZ_{calm} are a GM variation in waves and a calm-water GZ curve, respectively, and the frequency of GM variation is equal to ω_e. The restoring moment is calculated by assuming that heave and pitch always stay in their equilibrium points under the concerned ship and wave condition. The right-hand side is an external moment due to incident oblique waves, ζ_a is the amplitude, r is the effective wave slope coefficient, k is the wave number, and χ is the ship course from the wave propagating direction (χ = 0 means that the ship runs in following waves). Here, assuming that the ship runs at a constant speed U towards the direction χ and she does not drift at all, the wave encounter frequency is expressed as

Eq. 2.3.2 by using the wave frequency ω and the gravitational acceleration g, based on the deep-water linear wave theory:

$$\omega_e = \omega - \frac{\omega^2}{g} U \cos\chi \,. \tag{2.3.2}$$

2.4 Parametric Roll in Regular Longitudinal Waves

Parametric roll amplitude can be estimated by taking into account nonlinearities of GZ and/or roll damping. Kerwin (1955) modeled roll damping as nonlinear which increases with parametric roll amplitude and this equation was often used in the early stage of the research of parametric roll (Ogawara & Miura, 1960; Abicht, 1975). Sanchez and Nayfeh (1990a) intensively investigated parametric roll by applying nonlinear dynamical approaches to a 1-dof roll model with nonlinear GZ and roll damping.

Francescutto (2001) applied an averaging method to a 1-dof parametric roll model. He assumed that the roll damping and calm-water GZ curve could be approximated by cubic curves and the GM variation decreased proportionally with the square of roll. However, a calm-water GZ of a ship increases proportionally with the heel (the ratio is called GM) when the heel is small, after that the increasing ratio becomes larger than the GM, and starts to decrease after a weather deck submerges or a bottom emerges. In addition, the GM variation does not always decrease proportionally with the square of the roll even within a small wave steepness because it depends on the ship flare. This indicates that at least quintic approximation is necessary to approximate the nature of GZ. Umeda et al. (2004) applied an averaging method to roll equation with quintic GZ and nonlinear GM variation in waves. Further, they confirmed that this model showed good agreement with model experiment, so that parametric roll amplitude and characteristics are investigated based on this model in this study.

As further improvement about parametric roll estimation by an averaging method, Bulian (2004) applied it to a nonlinear Mathieu equation with cubic damping, nonic restoring moment, and higher order effect of GM variation.

2.4.1 Estimation Method proposed by Umeda et al.

Umeda et al. used following coefficients (Umeda et al., 2004):

$$2\alpha\left(\phi, \dot{\phi}\right) = 2\alpha + \gamma\dot{\phi}^2 \,, \tag{2.4.1.1}$$

$$\frac{GM_{vari}\left(t, \phi\right)}{GM} = \left(\frac{GM_{mean}}{GM} + \frac{GM_{amp}}{GM}\cos\omega_e t\right)\left(1 - \frac{1}{\pi^2}\phi^2\right), \tag{2.4.1.2}$$

$$\frac{GZ_{calm}\left(\phi\right)}{GM} = \phi + l_3\phi^3 + l_5\phi^5 \,, \tag{2.4.1.3}$$

$$\ddot{\phi} + 2\alpha\dot{\phi} + \gamma\dot{\phi}^3 + \omega_\phi{}^2\left(\frac{GM_{mean}}{GM} + \frac{GM_{amp}}{GM}\cos\omega_e t\right)\left(\phi - \frac{1}{\pi^2}\phi^3\right)$$

$$+\omega_\phi{}^2\left(\phi+l_3\phi^3+l_5\phi^5\right)=0. \tag{2.4.1.4}$$

Here, the roll damping and calm-water *GZ* curve are approximated by cubic and quintic polynomials, respectively. The GM variation is modeled to take account of the upside-down condition so that the GM variation becomes zero when $\phi = \pi$. The form of solutions is as Eq. 2.4.1.5:

$$\phi = A\cos\left(\hat{\omega}t-\varepsilon\right),\ \ \dot{\phi}=-\hat{\omega}A\sin\left(\hat{\omega}t-\varepsilon\right). \tag{2.4.1.5}$$

Here, A is the roll amplitude, $\hat{\omega}$ is the parametric roll frequency and is equal to half the wave encounter frequency, and ε is the phase lag. The time derivatives of A and ε are expressed as Eq. 2.4.1.6:

$$\dot{A}=\frac{\dot{\phi}}{\hat{\omega}^2 A}\left(\ddot{\phi}+\hat{\omega}^2\phi\right),\ \ \dot{\varepsilon}=\frac{\phi}{\hat{\omega}A^2}\left(\ddot{\phi}+\hat{\omega}^2\phi\right). \tag{2.4.1.6}$$

Substituting Eq. 2.4.1.4 and 2.4.1.5 into Eq. 2.4.1.6, the averaged equations are obtained as Eq. 2.4.1.7 and 2.4.1.8:

$$\dot{A}=-\alpha A-\frac{3}{8}\gamma\hat{\omega}^2A^3-\frac{1}{4}\frac{\omega_\phi{}^2}{\hat{\omega}}MA\left(1-\frac{1}{2\pi^2}A^2\right)\sin 2\varepsilon, \tag{2.4.1.7}$$

$$\dot{\varepsilon}=\frac{1}{2}\hat{\omega}-\frac{1}{2}\frac{\omega_\phi{}^2}{\hat{\omega}}\left[1+F\left(1-\frac{3}{4\pi^2}A^2\right)+\frac{3}{4}l_3A^2+\frac{5}{8}l_5A^4\right]$$
$$-\frac{1}{4}\frac{\omega_\phi{}^2}{\hat{\omega}}M\left(1-\frac{1}{\pi^2}A^2\right)\cos 2\varepsilon, \tag{2.4.1.8}$$

where

$$F=\frac{GM_{mean}}{GM},\ \ M=\frac{GM_{amp}}{GM}. \tag{2.4.1.9}$$

Setting the time derivatives are zero and eliminating the term with ε provide:

$$\sum_{k=0}^{12}a_k A^k=0, \tag{2.4.1.10}$$

where

$$a_0=\frac{64\pi^4}{25l_5{}^2\omega_\phi{}^4}\left\{4\hat{\omega}^4-8\hat{\omega}^2\left[-2\alpha^2+\omega_\phi{}^2\left(F+1\right)\right]\right.$$
$$\left.+\omega_\phi{}^4\left[4\left(F+1\right)^2-M^2\right]\right\}, \tag{2.4.1.11}$$

$$a_2=\frac{64\pi^2}{25l_5{}^2\omega_\phi{}^4}\left\{4\hat{\omega}^4\left(3\pi^2\alpha\gamma-1\right)\right.$$

$$+2\hat{\omega}^2\left[\omega_\phi{}^2\left(7F+4-3\pi^2 l_3\right)-16\alpha^2\right]$$
$$+\omega_\phi{}^4\left[6\pi^2 l_3(F+1)+3M^2-2(F+1)(5F+2)\right]\Big], \tag{2.4.1.12}$$

$$a_4=\frac{16}{25 l_5{}^2\omega_\phi{}^4}\Big\{9\pi^4\gamma^2\hat{\omega}^6+4\hat{\omega}^4\left(-24\pi^2\alpha\gamma+1\right)$$
$$+4\hat{\omega}^2\left[\omega_\phi{}^2\left(6\pi^2 l_3-5\pi^4 l_5-8F-2\right)+16\alpha^2\right]$$
$$+\omega_\phi{}^4\left[9\pi^4 l_3{}^2-6\pi^2 l_3(7F+4)\right.$$
$$\left.+20\pi^4 l_5(F+1)-13M^2+F(37F+32)+4\right]\Big\}, \tag{2.4.1.13}$$

$$a_6=\frac{16}{25\pi^2 l_5{}^2\omega_\phi{}^4}\Big\{-18\pi^4\gamma^2\hat{\omega}^6+48\pi^2\alpha\gamma\hat{\omega}^4$$
$$+2\omega_\phi{}^2\hat{\omega}^2\left(-3\pi^2 l_3+10\pi^4 l_5+3F\right)+\omega_\phi{}^4\left[-9\pi^4 l_3{}^2\right.$$
$$+3\pi^2 l_3(5\pi^4 l_5+8F+2)-5\pi^4 l_5(7F+4)+6M^2$$
$$\left.-3F(5F+2)\right]\Big\}, \tag{2.4.1.14}$$

$$a_8=\frac{4}{25\pi^4 l_5{}^2\omega_\phi{}^4}\Big\{36\pi^4\gamma^2\hat{\omega}^6-20\pi^4 l_5\omega_\phi{}^2\hat{\omega}^2$$
$$+\omega_\phi{}^4\left[25\pi^8 l_5{}^2-20\pi^4 l_5(3\pi^2 l_3-4F-1)\right.$$
$$\left.+9\left(F-\pi^2 l_3\right)^2-4M^2\right]\Big\}, \tag{2.4.1.15}$$

$$a_{10}=\frac{4}{5\pi^2 l_5}\left(3\pi^2 l_3-5\pi^4 l_5-3F\right), \tag{2.4.1.16}$$

$$a_{12}=1, \tag{2.4.1.17}$$

$$a_k=0 \quad \text{for } k=1, 3, ..., 11. \tag{2.4.1.18}$$

This algebraic equation of A can be found in Maki et al. (2011).

2.4.2 Effect of Superharmonics

In the method of Umeda et al. (2004) as shown in subsection 2.4.1, the existence of superharmonics is not assumed, thereby being neglected in the averaging processes. Actually, there should be a certain effect of superharmonics at least due to the nonlinearity of the differential equation. Based on the method of Umeda et al., the effect of superharmonics are considered in this subsection. Firstly, in order to confirm the error of the method of Umeda et al., a comparison between the method of Umeda et al. and numerically integrated solution of Eq. 2.4.1.4 is shown in Fig. 2.4.2.1 by using the C11-class post-Panamax container ship (used data are listed in appendix subject ships for detailed data), which suffered heavy parametric roll in 1998 (France et al., 2003). In the calculation, the roll damping is estimated by Ikeda's simplified method (Kawahara et al., 2012)

with the lift component of Ikeda's original method (Ikeda, 2004), the natural roll frequency and roll inertia moment are estimated from roll decay test by using a ship model of the C11-class post-Panamax container ship, and the restoring moment is estimated hydrostatically based on the Froude Krylov assumption by assuming that heave and pitch change quasi-statically. The experiment was conducted at the towing tank of Osaka University (Hashimoto & Umeda, 2010). The horizontal axis shows a ship speed in Froude number, and the vertical axis does a parametric roll amplitude in degrees. Figure 2.4.2.1 shows good agreement except around *Fn* of 0.00 to 0.05. Assuming that the discrepancy is derived from the absence of superharmonic components, the numerically integrated solution at *Fn* of 0.015 is expanded in Fourier series in Fig. 2.4.2.2. It shows that the second largest superharmonic component is three times as frequent as parametric roll. The discrepancy in Fig. 2.4.2.1 appears regardless of parametric roll amplitude; therefore, this can be said that the superharmonic effect is derived not only from the nonlinearity of the differential equation but also from characteristics of the Mathieu equation.

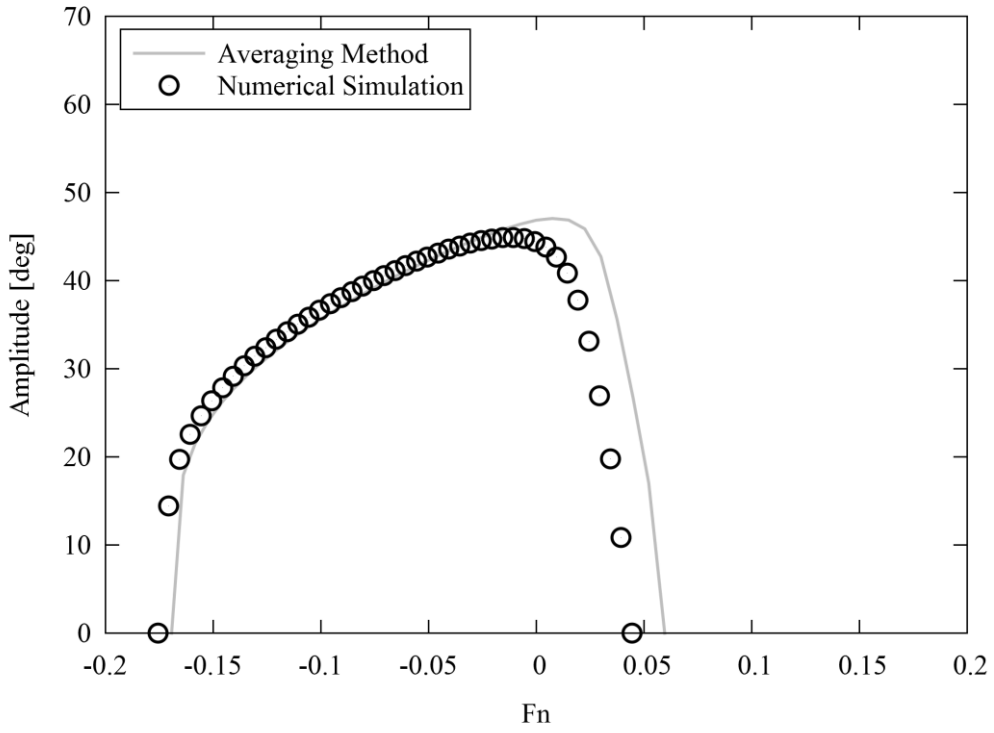

Figure 2.4.2.1 Parametric roll amplitude with λ/L_{pp} of 1.0 and H/λ of 0.03.

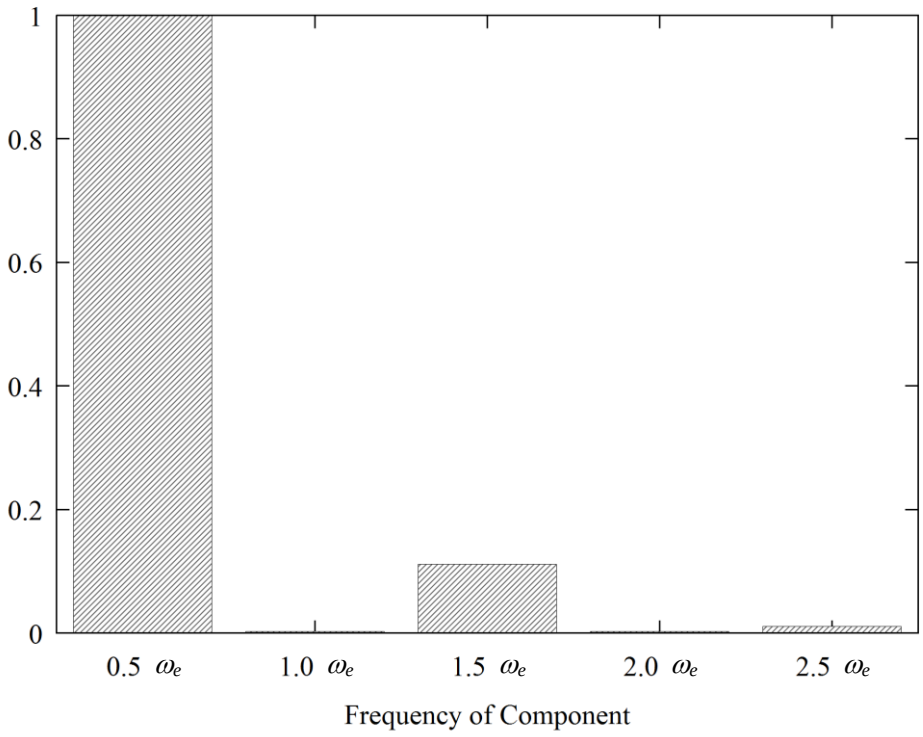

Figure 2.4.2.2 Amplitude ratio of each frequency component with Froude number of 0.015, λ/L of 1.0, and H/λ of 0.03.

Here, using the same coefficients as the method of Umeda et al. as shown in subsection 2.4.1 as follow:

$$\ddot{\phi}+2\alpha\dot{\phi}+\gamma\dot{\phi}^3+\omega_\phi{}^2\left(\frac{GM_{mean}}{GM}+\frac{GM_{amp}}{GM}\cos\omega_e t\right)\left(\phi-\frac{1}{\pi^2}\phi^3\right)+\omega_\phi{}^2\left(\phi+l_3\phi^3+l_5\phi^5\right)=0. \tag{2.4.2.1}$$

The form of solutions with the third superharmonic components is as Eq. 2.4.2.2:

$$\phi=\phi_1+\phi_3,\ \ \phi_1=A_1\cos\left(\hat{\omega}t-\varepsilon_1\right),\ \ \dot{\phi}_1=-\hat{\omega}A_1\sin\left(\hat{\omega}t-\varepsilon_1\right),$$
$$\phi_3=A_3\cos\left(3\hat{\omega}t-\varepsilon_3\right),\ \ \dot{\phi}_3=-3\hat{\omega}A_3\sin\left(3\hat{\omega}t-\varepsilon_3\right). \tag{2.4.2.2}$$

Here, A_1 and A_3 are the roll amplitudes, $\hat{\omega}$ is the parametric roll frequency and is equal to half the wave encounter frequency, and ε_1 and ε_3 are phase lags. The two components are defined as ϕ_1 and ϕ_3, respectively. The time derivatives of A_1, A_3, ε_1, and ε_3 are expressed as Eq. 2.4.2.3 and 2.4.2.4:

$$\dot{A}_1=\frac{\dot{\phi}_1}{\hat{\omega}^2A_1}\left(\ddot{\phi}_1+\hat{\omega}^2\phi_1\right),\ \ \dot{\varepsilon}_1=\frac{\phi_1}{\hat{\omega}A_1{}^2}\left(\ddot{\phi}_1+\hat{\omega}^2\phi_1\right), \tag{2.4.2.3}$$

$$\dot{A}_3=\frac{\dot{\phi}_3}{9\hat{\omega}^2A_3}\left(\ddot{\phi}_3+9\hat{\omega}^2\phi_3\right),\ \ \dot{\varepsilon}_3=\frac{\phi_3}{9\hat{\omega}A_3{}^2}\left(\ddot{\phi}_3+9\hat{\omega}^2\phi_3\right). \tag{2.4.2.4}$$

Here, Eq. 2.4.2.1 can be rewritten as Eq. 2.4.2.5:

$$\ddot{\phi} + \omega^2 \phi = g\left(\phi, \dot{\phi}, t\right), \tag{2.4.2.5}$$

where

$$\omega^2 = {\omega_\phi}^2 \left(1 + \frac{GM_{mean}}{GM}\right). \tag{2.4.2.6}$$

Substituting $\phi = \phi_1 + \phi_3$ into Eq. 2.4.4.5 provides:

$$\begin{aligned} &\left(\ddot{\phi}_1 + \hat{\omega}^2 \phi_1\right) + \left(\ddot{\phi}_3 + 9\hat{\omega}^2 \phi_3\right) \\ &= \left(\hat{\omega}^2 - \omega^2\right)\phi_1 + \left(9\hat{\omega}^2 - \omega^2\right)\phi_3 + g\left(\phi_1 + \phi_3, \dot{\phi}_1 + \dot{\phi}_3, t\right). \end{aligned} \tag{2.4.2.7}$$

The assumed solutions of ϕ_1 and ϕ_3 are determined as following the left-hand side of Eq. 2.4.2.7 by assuming the right-hand side of Eq. 2.4.2.7 as negligibly small. We need an additional assumption that the first and second parentheses on the left-hand side of Eq. 2.4.2.7 are sinusoidal functions with frequency of $\hat{\omega}$ and $3\hat{\omega}$, respectively. This is an assumption related to the second derivatives with time. Then, while averaging with one of the frequencies, the second derivative with another frequency can be zero. In order to apply the averaging method by using the assumed solution as Eq. 2.4.2.2, the first and second term of the right-hand side of Eq. 2.4.2.7 should be negligibly small; however, the second term is not small and the value is almost equal to $8\hat{\omega}$ when the first term can be regarded as small. This does not agree with the fact that the solution is expressed as a sum of sinusoidal functions with frequency of $\hat{\omega}$ and $3\hat{\omega}$ as shown in Fig. 2.4.2.2. Hence, the third term of the right-hand side should have the term that is proportional to ϕ_3 and the sum of them can be regarded as small. Using above assumptions and substituting Eq. 2.4.2.1 and 2.4.2.2 into Eq. 2.4.2.3 and 2.4.2.4, the averaged equations are obtained as Eq. 2.4.2.8 to 2.4.2.11:

$$\begin{aligned} \dot{A}_1 = &-\alpha A_1 - \frac{3}{8}\gamma\hat{\omega}^2 {A_1}^3 - \frac{27}{4}\gamma\hat{\omega}^2 A_1 {A_3}^2 \\ &+ M\sin\left(2\varepsilon_1\right)\left(\frac{{\omega_\phi}^2}{\hat{\omega}}\right)\left(\frac{1}{8\pi^2}{A_1}^3 + \frac{3}{8\pi^2}A_1 {A_3}^2 - \frac{1}{4}A_1\right) \\ &+ M\sin\left(\varepsilon_1 - \varepsilon_3\right)\left(\frac{{\omega_\phi}^2}{\hat{\omega}}\right)\left(\frac{3}{16\pi^2}{A_1}^2 A_3 + \frac{3}{16\pi^2}{A_3}^3 - \frac{1}{4}A_3\right) \\ &+ \sin\left(3\varepsilon_1 - \varepsilon_3\right)\left(\frac{{\omega_\phi}^2}{\hat{\omega}}\right)\left(-\frac{3}{8}l_3 {A_1}^2 A_3 - \frac{15}{32}l_5 {A_1}^4 A_3 - \frac{15}{16}l_5 {A_1}^2 {A_3}^3\right) \\ &+ \cos\left(3\varepsilon_1 - \varepsilon_3\right)\left(\frac{9}{8}\gamma\hat{\omega}^2 {A_1}^2 A_3\right), \end{aligned} \tag{2.4.2.8}$$

$$\dot{\varepsilon}_1 = \frac{1}{2\hat{\omega}}\left(\hat{\omega}^2 - {\omega_\phi}^2 - {\omega_\phi}^2 F\right)A_1 + \frac{3}{8}\left(\frac{{\omega_\varphi}^2}{\hat{\omega}}\right)\left(\frac{F}{\pi^2} - l_3\right){A_1}^3$$

$$
\begin{aligned}
&-\frac{5}{16}\left(\frac{\omega_\varphi^{\,2}}{\hat{\omega}}\right) l_5 A_1^{\,5} - \frac{15}{16}\left(\frac{\omega_\varphi^{\,2}}{\hat{\omega}}\right) l_5 A_1 A_3^{\,4} \\
&+\frac{3}{4}\left(\frac{\omega_\varphi^{\,2}}{\hat{\omega}}\right)\left(\frac{F}{\pi^2}-l_3\right) A_1 A_3^{\,2} - \frac{15}{8}\left(\frac{\omega_\varphi^{\,2}}{\hat{\omega}}\right) l_5 A_1^{\,3} A_3^{\,2} \\
&+M\cos(2\varepsilon_1)\left(\frac{\omega_\varphi^{\,2}}{\hat{\omega}}\right)\left(\frac{1}{4\pi^2}A_1^{\,3}+\frac{3}{8\pi^2}A_1 A_3^{\,2}-\frac{1}{4}A_1\right) \\
&+M\cos(\varepsilon_1-\varepsilon_3)\left(\frac{\omega_\varphi^{\,2}}{\hat{\omega}}\right)\left(\frac{9}{16\pi^2}A_1^{\,2}A_3+\frac{3}{16\pi^2}A_3^{\,3}-\frac{1}{4}A_3\right) \\
&+\cos(3\varepsilon_1-\varepsilon_3)\left(\frac{\omega_\varphi^{\,2}}{\hat{\omega}}\right) \\
&\quad\cdot\left(-\frac{25}{32}l_5 A_1^{\,4} A_3 - \frac{15}{16}l_5 A_1^{\,2} A_3^{\,3} + \frac{3}{8}\left(\frac{F}{\pi^2}-l_3\right) A_1^{\,2} A_3\right) \\
&+\sin(3\varepsilon_1-\varepsilon_3)\left(-\frac{9}{8}\gamma\hat{\omega}^2 A_1^{\,2} A_3\right),
\end{aligned}
\tag{2.4.2.9}
$$

$$
\begin{aligned}
\dot{A}_3 = &-\alpha A_3 - \frac{27}{8}\gamma\hat{\omega} A_3^{\,3} - \frac{3}{4}\gamma\hat{\omega} A_1^{\,2} A_3 \\
&+M\sin(\varepsilon_1-\varepsilon_3)\left(\frac{\omega_\varphi^{\,2}}{\hat{\omega}}\right)\left(-\frac{1}{16\pi^2}A_1^{\,3}-\frac{3}{16\pi^2}A_1 A_3^{\,3}+\frac{1}{12}A_1\right) \\
&+\sin(3\varepsilon_1-\varepsilon_3)\left(\frac{\omega_\phi^{\,2}}{\hat{\omega}}\right)\left[\frac{5}{96}l_5 A_1^{\,5}+\frac{5}{48}l_5 A_1^{\,3} A_3^{\,2}-\frac{1}{24}\left(\frac{F}{\pi^2}-l_3\right)A_1^{\,3}\right] \\
&+\cos(3\varepsilon_1-\varepsilon_3)\left(\frac{1}{24}\gamma\hat{\omega}^2 A_1^{\,3}\right),
\end{aligned}
\tag{2.4.2.10}
$$

$$
\begin{aligned}
\dot{\varepsilon}_3 = &\frac{1}{6\hat{\omega}}\left(9\hat{\omega}^2-\omega_\varphi^{\,2}-\omega_\varphi^{\,2}F\right)A_3 - \frac{15}{16}\left(\frac{\omega_\varphi^{\,2}}{\hat{\omega}}\right) l_5 A_1^{\,4} A_3 \\
&-\frac{5}{8}\left(\frac{\omega_\varphi^{\,2}}{\hat{\omega}}\right) l_5 A_1^{\,2} A_3^{\,3} - \frac{5}{48}l_5\left(\frac{\omega_\varphi^{\,2}}{\hat{\omega}}\right) A_3^{\,5} \\
&+\frac{1}{4}\left(\frac{\omega_\varphi^{\,2}}{\hat{\omega}}\right)\left(\frac{F}{\pi^2}-l_3\right)A_1^{\,2} A_3 + \frac{1}{8}\left(\frac{\omega_\varphi^{\,2}}{\hat{\omega}}\right)\left(\frac{F}{\pi^2}-l_3\right)A_3^{\,3} \\
&+M\cos(2\varepsilon_1)\left(\frac{\omega_\varphi^{\,2}}{\hat{\omega}}\right)\left(\frac{1}{8\pi^2}A_1^{\,2}A_3\right) \\
&+M\cos(\varepsilon_1-\varepsilon_3)\left(\frac{\omega_\varphi^{\,2}}{\hat{\omega}}\right)\left(\frac{1}{16\pi^2}A_1^{\,3}+\frac{3}{16\pi^2}A_1 A_3^{\,2}-\frac{1}{12}A_1\right)
\end{aligned}
$$

$$+\cos\left(3\varepsilon_1-\varepsilon_3\right)\left(\frac{{\omega_\varphi}^2}{\hat{\omega}}\right)$$
$$\cdot\left[-\frac{5}{96}l_5 A_1^5-\frac{5}{16}l_5 A_1^3 A_3^2+\frac{1}{24}\left(\frac{F}{\pi^2}-l_3\right)A_1^3\right]$$
$$+\sin\left(3\varepsilon_1-\varepsilon_3\right)\left(\frac{1}{24}\gamma\hat{\omega}^2 A_1^3\right), \qquad (2.4.2.11)$$

where

$$F=\frac{GM_{mean}}{GM},\quad M=\frac{GM_{amp}}{GM} \qquad (2.4.2.12)$$

Next, sample calculations of the averaged equations are shown for the C11-class post-Panamax container ship (used data are listed in appendix subject ships). Figures 2.4.2.3, 2.4.2.4, and 2.4.2.5 show that comparisons between the newly-proposed method, the method of Umeda et al. and numerically integrated solution of Eq. 2.4.2.1. The results of the newly-proposed method are obtained by using the Newton method with appropriate initial conditions. This is because the averaged equations are nonlinear simultaneous equations with four independent variables A_1, A_3, ε_1, and ε_3, so that it is very difficult to obtain equations which includes only one variable like the method of Umeda et al.

Figure 2.4.2.3 shows the results of the same condition as Fig. 2.4.2.1 and the newly-proposed method clearly shows much better agreement with the numerically integrated solution than the method of Umeda et al. Figure 2.4.2.4 shows that the method of Umeda et al. disagrees with the numerically integrated solution but the newly-proposed method agrees well with the numerically integrated solution. Since a difference between the two is just the wave heights, it can be said that parametric roll is much more affected by superhrmonics in the case of larger GM variation. In addition, experimental results are plotted in this figure. The 1-dof roll model conservatively predict the results of the experiments. This is because heave and pitch effects on a roll restoring moment are neglected, and because the restoring variation is represented only by the GM variation based on the Froude Krylov assumption. The effect of heave and pitch is investigated in subsection 2.4.4, and the effect of GZ variation was investigated by Hashimoto and Umeda (2004) and Hashimoto et al. (2008) based on model experiment and calculation. Figure 2.4.2.5 shows that the time series of parametric roll estimated by the three methods under the same condition as Fig. 2.4.2.3, in which the method of Umeda et al. does not show good agreement. The importance of the third superharmonic components can be clearly understood in Fig. 2.4.2.5.

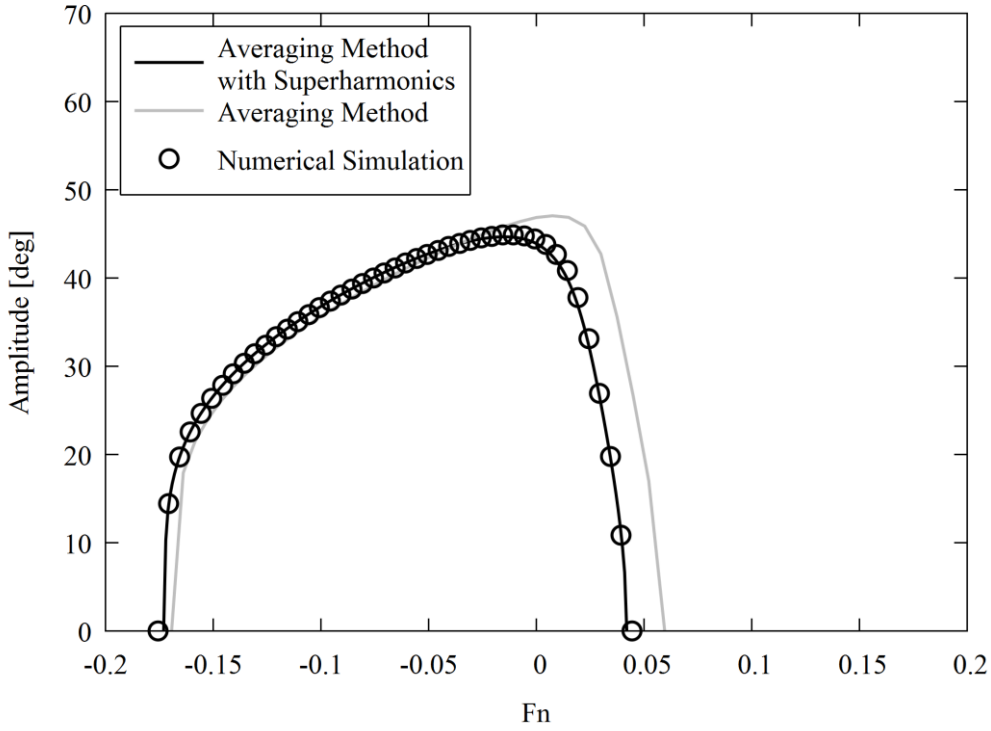

Figure 2.4.2.3 Parametric roll amplitude with λ/L of 1.0 and H/λ of 0.03.

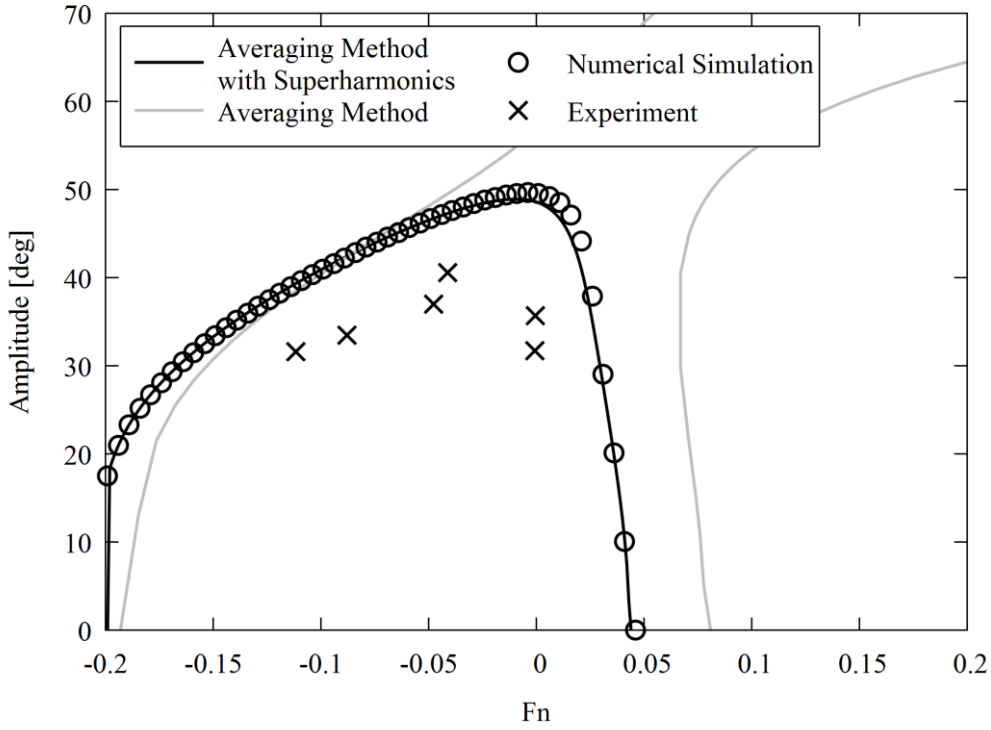

Figure 2.4.2.4 Parametric roll amplitude with λ/L of 1.0 and H/λ of 0.04.

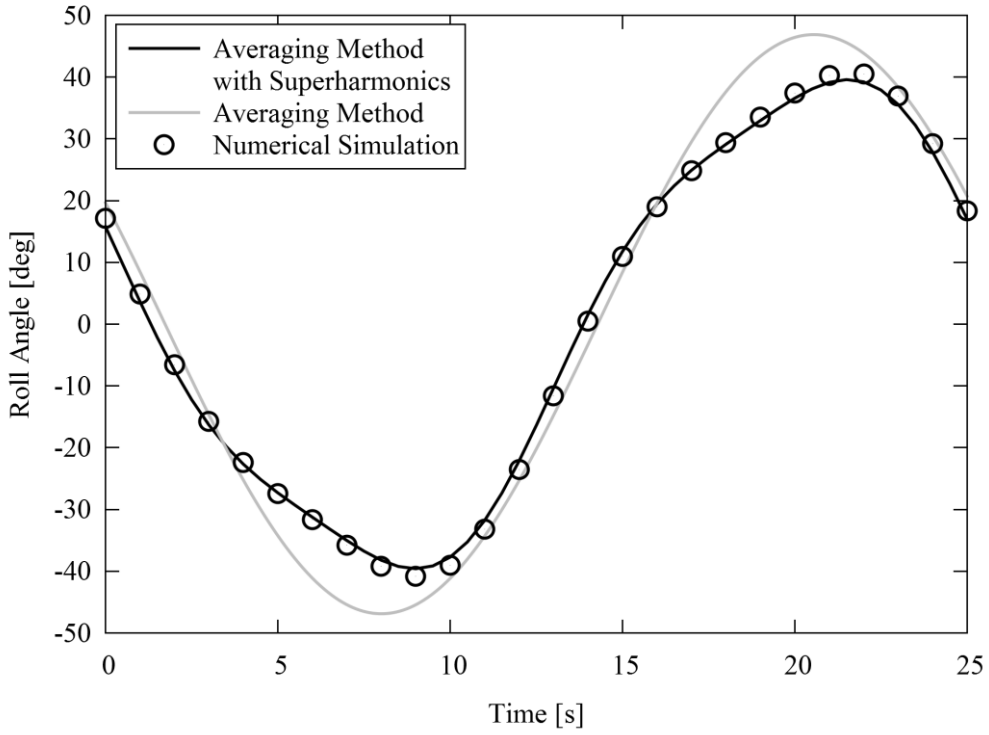

Figure 2.4.2.5 Time series with Froude number of 0.015, λ/L of 1.0 and H/λ of 0.03.

2.4.3 Effect of Approximation of Calm-Water GZ Curve

The calm-water GZ curve is approximated by a quintic polynomial in subsection 2.4.1 and 2.4.2 in order to obtain polynomial expression of averaged equations with amplitudes. However, a quintic polynomial is sometimes insufficient to approximate a calm-water GZ curve. In this subsection, an averaging method is applied to a 1-dof parametric roll model without calm-water GZ approximation. Further, the effect of accuracy of calm-water GZ approximation is investigated by using the obtained averaged equations.

The coefficients of the damping and GM variation are the same as the method of Umeda et al. (2004) as shown in section 2.4.1. By contrast, the calm-water GZ curve is not approximated by a quintic polynomial, so that the roll equation is as Eq. 2.4.3.1.:

$$\ddot{\phi}+2\alpha\dot{\phi}+\gamma\dot{\phi}^3+\omega_\phi{}^2\left(\frac{GM_{mean}}{GM}+\frac{GM_{amp}}{GM}\cos\omega_e t\right)\left\{\phi-\left(1/\pi^2\right)\phi^3\right\} + \omega_\phi{}^2\frac{GZ_{calm}(\phi)}{GM}=0. \qquad (2.4.3.1)$$

Following the same procedure as the method of Umeda et al., averaged equations are derived as Eq. 2.4.3.2 and 2.4.3.3:

$$\dot{A}=-\alpha A-\frac{3}{8}\gamma\hat{\omega}^2A^3-\frac{1}{4}\frac{\omega_\phi{}^2}{\hat{\omega}}MA\left(1-\frac{1}{2\pi^2}A^2\right)\sin 2\varepsilon$$

$$+\frac{\omega_\phi^{\,2}}{2\pi GM}\int_0^{\frac{2\pi}{\hat{\omega}}} GZ_{calm}\left(A\cos\left(\hat{\omega}t-\varepsilon\right)\right)\sin\left(\hat{\omega}t-\varepsilon\right)dt\,, \tag{2.4.3.2}$$

$$\begin{aligned}\dot{\varepsilon} = {} & \frac{1}{2}\hat{\omega}-\frac{1}{2}\frac{\omega_\phi^{\,2}}{\hat{\omega}}F\left(1-\frac{3}{4\pi^2}A^2\right)\\ & -\frac{1}{4}\frac{\omega_\phi^{\,2}}{\hat{\omega}}M\left(1-\frac{1}{\pi^2}A^2\right)\cos 2\varepsilon\\ & -\frac{\omega_\phi^{\,2}}{2\pi GM\,A}\int_0^{\frac{2\pi}{\hat{\omega}}} GZ_{calm}\left(A\cos\left(\hat{\omega}t-\varepsilon\right)\right)\cos\left(\hat{\omega}t-\varepsilon\right)dt\,,\end{aligned} \tag{2.4.3.3}$$

where

$$F=\frac{GM_{mean}}{GM}\ ,\ \ M=\frac{GM_{amp}}{GM}\,. \tag{2.4.3.4}$$

The integration term in Eq. 2.4.3.2 is calculated as Eq. 2.4.3.5:

$$\begin{aligned}&\int_0^{\frac{2\pi}{\hat{\omega}}} GZ_{calm}\left(A\cos\left(\hat{\omega}t-\varepsilon\right)\right)\sin\left(\hat{\omega}t-\varepsilon\right)dt\\ &=-\frac{1}{\hat{\omega}A}\int_0^{\frac{2\pi}{\hat{\omega}}} GZ_{calm}\left(A\cos\left(\hat{\omega}t-\varepsilon\right)\right)\frac{d}{dt}\left[A\cos\left(\hat{\omega}t-\varepsilon\right)\right]dt\\ &=-\frac{1}{\hat{\omega}A}\left[P_{calm}\left(A\cos\left(\hat{\omega}t-\varepsilon\right)\right)\right]_0^{\frac{2\pi}{\hat{\omega}}}\\ &=0\,.\end{aligned} \tag{2.4.3.5}$$

Here, P_{calm} is an indefinite integral of GZ_{calm}. However, there is still an integration term left in 2.4.3.3, so that it is impossible to obtain analytical solutions of the amplitude and phase difference. In this study, the Newton method is used to obtain solutions from initial values that are obtained from the existing averaged equations proposed by Umeda et al. (2004) according to Eq. 2.4.1.7 to 2.4.1.18.

Figure 2.4.3.1 shows validation of the averaged equations by using the ONR Flare topside vessel, C11-class post-Panamax container ship, and ITTC A-1 container ship. In the calculation, the roll damping is estimated by Ikeda's simplified method (Kawahara et al., 2012) with the lift component of Ikeda's original method (Ikeda, 2004), the natural roll frequency and roll inertia moment are estimated from roll decay tests by using the ship models, and the restoring moment is hydrostatically estimated in longitudinal waves based on the Froude Krylov assumption by assuming that heave and pitch change quasi-statically. (See appendix subject ships about the ships, coefficients, and experiments.) The averaging method without the polynomial approximation of the calm-water GZ curve (ave_GZ) is compared with the averaging method with the polynomial approximation proposed by Umeda et al. (the existing averaging method, ave_exg), numerical solutions of the uncoupled roll equation without the polynomial approximation (sim_1), and experiments (exp) as shown in Fig. 2.4.3.1. Positive and negative Froude numbers indicate that the ship runs in following

and heading waves, respectively. All methods here conservatively predict the results of the experiments. This is because heave and pitch effects on a roll restoring moment are neglected, and because the GZ variation is represented only by the GM variation based on the Froude Krylov assumption. The effect of heave and pitch is investigated in subsection 2.4.4, and the effect of GZ variation was investigated by Hashimoto and Umeda (2004) and Hashimoto et al. (2008) based on model experiment and calculation. The ave_GZ gives almost the same results as those of both ave_exg and sim_1 for the ONR Flare topside vessel and the C11-class post-Panamax container ship. However, this is not so for the ITTC A-1 container ship; the ave_GZ well agree only with sim_1 in that case. This is because the accuracy of the fitted GZ curves is unsatisfactory only for the ITTC A-1 container ship, as shown in Fig. 2.4.3.2. Hence, the method using the original GZ curves can be recommended only if the fitted GZ is not satisfactory.

Figure 2.4.3.1 (e) shows that the parametric roll amplitude estimated by the method of Umeda et al. (ave_exg) shifts towards the right relative to the averaging method with actual GZ curve. In order to investigate how the discrepancy of calm-water GZ curve affects the estimated amplitude, an equation of steady state parametric roll amplitude is derived from Eq. 2.4.3.2-3. Although the integration term in Eq. 2.4.3.3 appears to be a function of ε, it is independent of ε and just a function of A because the interval of the integration is over one period. Setting the time derivatives of Eq. 2.4.3.2-3 to zero and eliminating the term with ε from them provides:

$$\begin{aligned}
&\frac{\hat{\omega}}{2\pi}\frac{2}{GM\,A}\int_0^{\frac{2\pi}{\hat{\omega}}} GZ_{calm}\left(A\cos\left(\hat{\omega}t-\varepsilon\right)\right)\cos\left(\hat{\omega}t-\varepsilon\right)dt \\
&=\frac{\hat{\omega}^2}{{\omega_\phi}^2}-F\left(1-\frac{3}{4\pi^2}A^2\right) \\
&\pm\frac{1}{2}M\left(1-\frac{1}{\pi^2}A^2\right)\sqrt{1-\left[\frac{\frac{\hat{\omega}}{{\omega_\phi}^2}\left(\alpha+\frac{3}{8}\gamma\hat{\omega}^2A^2\right)}{\frac{1}{4}M\left(1-\frac{1}{2\pi^2}A^2\right)}\right]^2}\,.
\end{aligned} \tag{2.4.3.6}$$

Setting $\tau=\hat{\omega}t$, the left-hand side of Eq. 2.4.3.6 is rewritten as:

$$\begin{aligned}
&\frac{\hat{\omega}}{2\pi}\frac{2}{GM\,A}\int_0^{\frac{2\pi}{\hat{\omega}}} GZ_{calm}\left(A\cos\left(\hat{\omega}t-\varepsilon\right)\right)\cos\left(\hat{\omega}t-\varepsilon\right)dt \\
&=\frac{1}{2\pi}\frac{2}{GM\,A}\int_0^{2\pi} GZ_{calm}\left(A\cos\tau\right)\cos\tau\,d\tau\,.
\end{aligned} \tag{2.4.3.7}$$

Here, since the integration interval is the same as the period of the integrand $2\pi/\hat{\omega}$, shifting the phase of integrand does not change the result. Thus, the left-hand side depends only on parametric roll amplitude and GZ in calm water. When GZ_{calm} is fitted by a quintic curve, Eq. 2.4.3.7 is expressed as Eq. 2.4.3.8:

$$\frac{1}{2\pi}\frac{2}{GM\,A}\int_0^{2\pi} GZ_{calm}\left(A\cos\tau\right)\cos\tau\,d\tau$$
$$=\frac{1}{2\pi}\frac{2}{A}\int_0^{2\pi}\left[\left(A\cos\tau\right)+l_3\left(A\cos\tau\right)^3+l_5\left(A\cos\tau\right)^5\right]\cos\tau\,d\tau$$
$$=1+\frac{3}{4}l_3\,A^2+\frac{5}{8}l_5\,A^4. \qquad (2.4.3.8)$$

Here, the linear coefficient is GM in calm water. Of course, substituting Eq. 2.4.3.7-8 into Eq. 2.4.3.6 yields an equivalent equation to Eq. 2.4.1.10. The solutions of Eq. 2.4.3.6 are expressed as crossing points when the curves of the both sides are drawn as functions of parametric roll amplitude. For the ITTC A-1 container ship, the left and right-hand side of Eq. 2.4.3.6 are plotted on Fig. 2.4.3.3 in case of *Fn* of -0.117 and -0.170. The left-hand sides of ave_GZ and ave_exg are calculated as following Eq. 2.4.3.7 and Eq. 2.4.3.8, respectively, and represented by the black and gray solid lines, respectively. The dashed lines are the value of the right-hand side. Since the left-hand side is calculated only with the calm-water GZ curve, the difference between ave_GZ and ave_exg is purely derived from the accuracy of calm-water GZ approximation. On the other hand, the right-hand side are not affected by the nonlinear calm-water GZ component because the natural roll frequency is directly depends on GM in calm-water, and GM variations are nondimensionalized by GM in calm-water. The value of horizontal axis of the crossing point between the solid and dashed lines represents steady state parametric roll amplitude. According to Eq. 2.4.3.6, when the ship speed increases, the right hand side move to the downward in case that *A* is not so large. That can be clearly confirmed in Fig. 2.4.3.3. From the above, for the ITTC ship A-1 container ship, the cubic coefficient of her approximated calm-water GZ curve is underestimated, so that the left-hand side of Eq. 2.4.3.6 becomes smaller, and the parametric roll amplitude shifts towards the right.

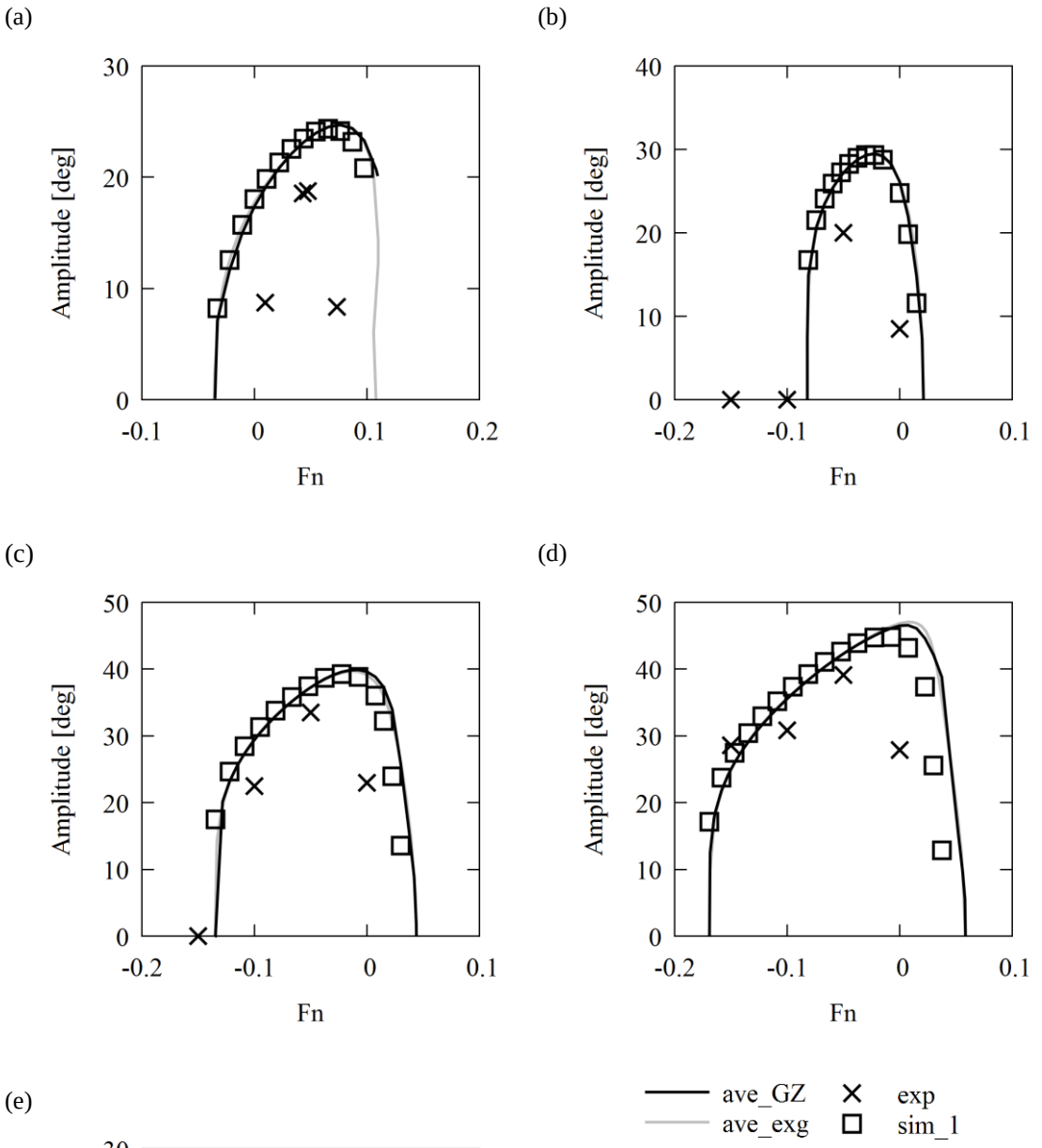

Figure 2.4.3.1
Comparison of parametric roll amplitudes from the averaging methods with and without the polynomial approximation of the calm-water GZ curves in longitudinal waves:

(a) ONR flare topside vessel with a wave steepness of 0.04;
(b) C11-class post-Panamax container ship with a wave steepness of 0.01;
(c) C11-class post-Panamax container ship with a wave steepness of 0.02;
(d) C11-class post-Panamax container ship with a wave steepness of 0.03;
(e) ITTC A-1 container ship with a wave steepness of 0.03.

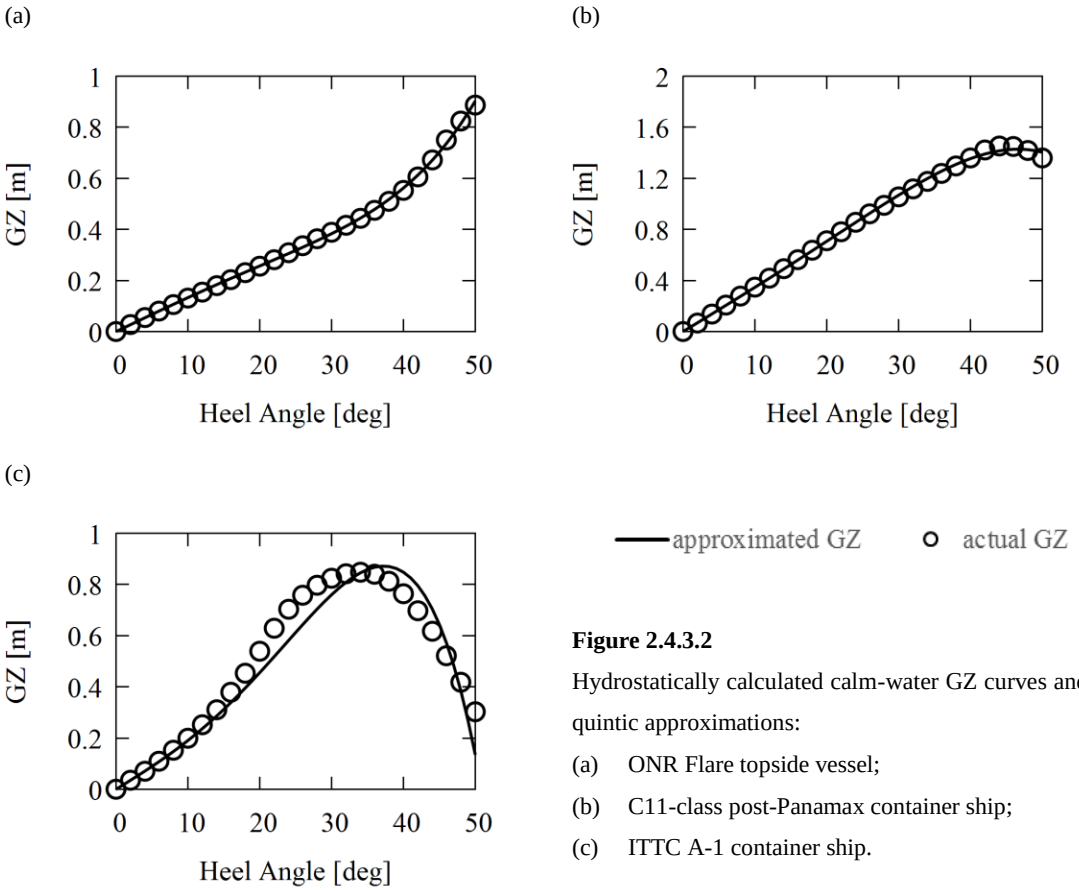

Figure 2.4.3.2

Hydrostatically calculated calm-water GZ curves and their quintic approximations:

(a) ONR Flare topside vessel;

(b) C11-class post-Panamax container ship;

(c) ITTC A-1 container ship.

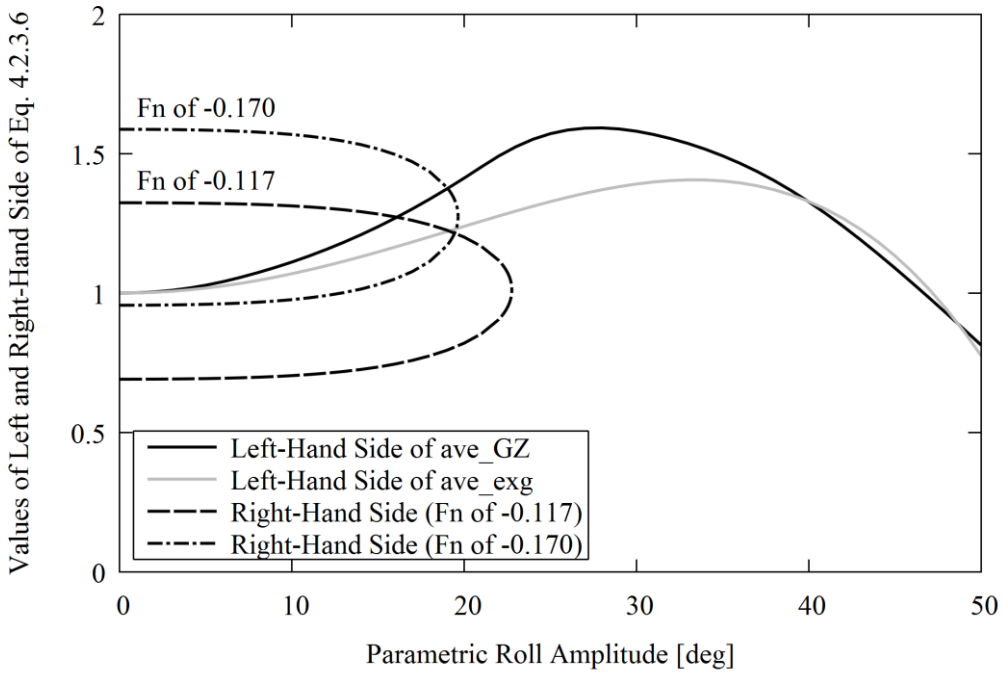

Figure 2.4.3.3 Values of the left- and right-hand side of Eq. 2.4.3.6.

2.4.4 Effect of Vertical Motions

In subsections 2.4.1, 2.4.2, and 2.4.3, the GM variation is caused by change of water-area due to longitudinal waves, and heave and pitch are assumed to quasi-statically trace their equilibria in waves. Since the GM can be changed by ship vertical motions, i.e. heave and pitch, heave and pitch should be estimated more accurately. Neves and Rodriguez (2006) showed that their third-order nonlinear heave-roll-pitch coupled model agreed well with model experiment in regular heading waves. Taguchi et al. (2006) added the GM variation due to linearly estimated heave and pitch to a 1-dof roll model and confirmed that the 1-dof roll model could estimate the property of parametric roll by comparing the estimated amplitudes with those of free running model experiment. In this subsection, the effect of vertical motions on the GM variation is considered apart from the effect of an incident wave profile and how the heave and pitch affect parametric roll is investigated.

The roll equation here is also based on the method of Umeda et al. (2004) in subsection 2.4.1 but restoring moment is calculated without changing sinkage and trim. Comparing estimated parametric roll amplitude with and without the vertical motions with free running model experiment shows the importance of GM variation due to the vertical motions. Since roll-heave-pitch coupled motion equations are too complicated to apply an averaging method, linearly-estimated heave and pitch motion are used to estimate the GM variation due to vertical motion. The linear heave-pitch coupled equations are as Eq. 2.4.4.1 and 2.4.4.2:

$$\begin{aligned}&\left(m+A_{33}\right)\ddot{z}+B_{33}\,\dot{z}+\left(\rho g\,A_w+C_{33}\right)z\\&+A_{35}\,\ddot{\theta}+B_{35}\,\dot{\theta}+\left(\rho g\,A_w\,L_{CB}+C_{35}\right)\theta\\&\quad=\left|F_3^{FK}\right|\cos\left(\omega_e t+\varepsilon_3^{FK}\right)+\left|F_3^{D}\right|\cos\left(\omega_e t+\varepsilon_3^{D}\right),\end{aligned}\tag{2.4.4.1}$$

$$\begin{aligned}&\left(I_{yy}+A_{55}\right)\ddot{\theta}+B_{55}\,\dot{\theta}+\left(\rho g W GM_L+C_{55}\right)\theta\\&+A_{53}\,\ddot{z}+B_{53}\,\dot{z}+\left(\rho g\,A_w\,L_{CB}+C_{53}\right)z\\&\quad=\left|F_5^{FK}\right|\cos\left(\omega_e t+\varepsilon_5^{FK}\right)+\left|F_5^{D}\right|\cos\left(\omega_e t+\varepsilon_5^{D}\right).\end{aligned}\tag{2.4.4.2}$$

Here, z and θ are heave and pitch displacement, m and I_{yy} are a ship mass and pitch inertia, ρ is density of fluid, and g is gravitational acceleration. The term A_w is water-plane area in calm water, L_{CB} is a longitudinal position of centre of buoyancy from ship gravitational centre, and W is ship displacement. The terms A_{ij}, B_{ij} and C_{ij} are the added mass, wave damping coefficient and restoring coefficient, respectively, and subscripts 3 and 5 indicate heave and pitch, respectively. The absolute values of F are amplitudes of external forces, ε is a phase lag of the external force, and the superscripts FK and D indicate the Froude Krylov force and diffraction force, respectively. The derived heave and pitch are expressed as Eq. 2.4.4.3 and 2.4.4.4:

$$z=z_{am}\sin\left(\omega_e t+\varepsilon_z\right),\tag{2.4.4.3}$$

$$\theta=\theta_{am}\sin\left(\omega_e t+\varepsilon_\theta\right).\tag{2.4.4.4}$$

GM is a function of heave, pitch, wave amplitude ζ_a, and relative position between the ship and

wave ξ_G as Eq. 2.4.4.5:

$$GM = GM\left(z, \theta, \zeta_a, \xi_G\right). \tag{2.4.4.5}$$

Then, GM variation due to heave GM_z and pitch GM_θ are defined as Eq. 2.4.4.6 and 2.4.4.7:

$$\begin{aligned} GM_z &= \frac{\partial GM}{\partial z}\left(z, \theta, \zeta_a, \xi_G\right)\Big|_{z=0, \theta=0, \zeta_a=0} \\ &\equiv \frac{GM\left(z_{am}, 0, 0, \xi_G\right) - GM\left(-z_{am}, 0, 0, \xi_G\right)}{2\, z_{am}}, \end{aligned} \tag{2.4.4.6}$$

$$\begin{aligned} GM_\theta &= \frac{\partial GM}{\partial \theta}\left(z, \theta, \zeta_a, \xi_G\right)\Big|_{z=0, \theta=0, \zeta_a=0} \\ &\equiv \frac{GM\left(0, \theta_{am}, 0, \xi_G\right) - GM\left(0, -\theta_{am}, 0, \xi_G\right)}{2\, \theta_{am}}. \end{aligned} \tag{2.4.4.7}$$

Since the GM variations are calculated in calm water, the relative position does not affect the result. The roll equation is as Eq. 2.4.4.8:

$$\begin{aligned} &\ddot{\phi} + 2\alpha\,\dot{\phi} + \gamma\,\dot{\phi}^3 + \omega_\phi{}^2\left(\frac{GM_{mean}}{GM} + \frac{GM_{amp}}{GM}\cos\omega_e t\right)\left(\phi - \frac{1}{\pi^2}\phi^3\right) \\ &\quad + \omega_\phi{}^2\left(\phi + l_3\phi^3 + l_5\,\phi^5\right) + \omega_\phi{}^2\left(\frac{GM_z}{GM}\,z + \frac{GM_\theta}{GM}\,\theta\right)\phi = 0. \end{aligned} \tag{2.4.4.8}$$

Here, restoring moment in calm water and waves are calculated without changing sinkage and trim. Applying an averaging method as the same procedure of subsection 2.4.1 provides following averaged equations and an algebraic equation of parametric roll amplitude:

$$\begin{aligned} \dot{A} = &-\alpha A - \frac{3}{8}\gamma\hat{\omega}^2 A^3 - \frac{1}{4}\frac{\omega_\varphi{}^2}{\hat{\omega}} MA\left(1 - \frac{1}{2\pi^2}A^2\right)\sin 2\varepsilon \\ &+ \frac{1}{4}\frac{\omega_\phi{}^2}{\hat{\omega}} M_z\, z_{am}\, A\cos\left(2\varepsilon + \varepsilon_z\right) + \frac{1}{4}\frac{\omega_\phi{}^2}{\hat{\omega}} M_\theta\, \theta_{am}\, A\cos\left(2\varepsilon + \varepsilon_\theta\right), \end{aligned} \tag{2.4.4.9}$$

$$\begin{aligned} \dot{\varepsilon} = &\frac{1}{2}\hat{\omega} - \frac{1}{2}\frac{\omega_\phi{}^2}{\hat{\omega}}\left[1 + F\left(1 - \frac{3}{4\pi^2}A^2\right) + \frac{3}{4}l_3 A^2 + \frac{5}{8}l_5 A^4\right] \\ &- \frac{1}{4}\frac{\omega_\phi{}^2}{\hat{\omega}} M\left(1 - \frac{1}{\pi^2}A^2\right)\cos 2\varepsilon, \\ &- \frac{1}{4}\frac{\omega_\phi{}^2}{\hat{\omega}}\frac{GM_z}{GM} z_{am}\sin\left(2\varepsilon + \varepsilon_z\right) - \frac{1}{4}\frac{\omega_\phi{}^2}{\hat{\omega}}\frac{GM_\theta}{GM}\theta_{am}\sin\left(2\varepsilon + \varepsilon_\theta\right), \end{aligned} \tag{2.4.4.10}$$

$$\sum_{k=0}^{12} b_k\, A^k = 0\ , \tag{2.4.4.11}$$

$$
\begin{aligned}
b_0 = a_0 &+ \frac{256\pi^4}{25M^2 l_5^{\,2}\omega_\phi^{\,4}}\left(M_z^{\,2} z_{am}^{\,2} + M_\theta^{\,2}\theta_{am}^{\,2}\right)\left\{\hat{\omega}^4\right. \\
&\left. +2\hat{\omega}^2\left[2\alpha^2 - \omega_\phi^{\,2}(1+F)\right] + \omega_\phi^{\,4}(F-M+1)(F+M+1)\right\} \\
&- \frac{64\pi^4}{25M^2 l_5^{\,2}}\left(M_z^{\,4} z_{am}^{\,4} + 4M_z^{\,2} z_{am}^{\,2} M_\theta^{\,2}\theta_{am}^{\,2} + M_\theta^{\,4}\theta_{am}^{\,4}\right) \\
&+ \frac{256\pi^4}{25M l_5^{\,2}\omega_\phi^{\,4}}\left\{2\hat{\omega}^4 + 4\hat{\omega}^2\left[2\alpha^2 - \omega_\phi^{\,2}(F+1)\right]\right. \\
&\left. +\omega_\phi^{\,4}\left[2(F+1)^2 - M^2\right]\right\}\left[M_z z_{am}\sin(\varepsilon_z) + M_\theta\theta_{am}\sin(\varepsilon_\theta)\right] \\
&- \frac{256\pi^4}{25M l_5^{\,2}}\left[\left(M_z^{\,2} z_{am}^{\,2} + 2M_\theta^{\,2}\theta_{am}^{\,2}\right)M_z z_{am}\sin(\varepsilon_z)\right. \\
&\qquad \left. +\left(2M_z^{\,2} z_{am}^{\,2} + M_\theta^{\,2}\theta_{am}^{\,2}\right)M_\theta\theta_{am}\sin(\varepsilon_\theta)\right] \\
&+ \frac{256\pi^4}{25M^2 l_5^{\,2}\omega_\phi^{\,4}}\left\{2\hat{\omega}^4 + 4\hat{\omega}^2\left[2\alpha^2 - \omega_\phi^{\,2}(F+1)\right] + \omega_\phi^{\,4}\left[2(F+1)^2\right.\right. \\
&\qquad \left.\left. -2M^2 - M_z^{\,2} z_{am}^{\,2} - M_\theta^{\,2}\theta_{am}^{\,2}\right]\right\} M_z z_{am} M_\theta\theta_{am}\cos(\varepsilon_z - \varepsilon_z) \\
&+ \frac{256\pi^4}{25 l_5^{\,2}} M_z z_{am} M_\theta\theta_{am}\cos(\varepsilon_z + \varepsilon_z) \\
&+ \frac{128\pi^4}{25 l_5^{\,2}}\left[M_z^{\,2} z_{am}^{\,2}\cos(2\varepsilon_z) + M_\theta^{\,2}\theta_{am}^{\,2}\cos(2\varepsilon_\theta)\right] \\
&- \frac{128\pi^4}{25M^2 l_5^{\,2}} M_z^{\,2} z_{am}^{\,2} M_\theta^{\,2}\theta_{am}^{\,2}\cos\left[2(\varepsilon_z - \varepsilon_\theta)\right] \\
&+ \frac{256\pi^4}{25 l 5^2 M} M_z z_{am} M_\theta\theta_{am} \\
&\qquad \cdot\left[M_z z_{am}\sin(2\varepsilon_z - \varepsilon_\theta) + M_\theta\theta_{am}\sin(2\varepsilon_\theta - \varepsilon_z)\right], \qquad (2.4.4.12)
\end{aligned}
$$

$$
\begin{aligned}
b_2 = a_2 &+ \frac{384\pi^2}{25M^2 l_5^{\,2}\omega_\phi^{\,4}}\left(M_z^{\,2} z_{am}^{\,2} + M_\theta^{\,2}\theta_{am}^{\,2}\right)\left\{2\pi^2\alpha\gamma\hat{\omega}^4\right. \\
&\left. +\left(F - \pi^2 l_3\right)\omega_\phi^{\,2}\hat{\omega}^2 + \omega_\phi^{\,2}\left[-F(F+1) + M^2 + (F+1)\pi^2 l_3\right]\right\} \\
&+ \frac{512\pi^2\alpha\left[\hat{\omega}^3 - \omega_\phi^{\,2}\hat{\omega}(F+1)\right]}{25M l_5^{\,2}\omega_\phi^{\,4}} \\
&\qquad \cdot\left[M_z z_{am}\cos(\varepsilon_z) + M_\theta\theta_{am}\cos(\varepsilon_\theta)\right] \\
&+ \frac{64}{25M l_5^{\,2}\omega_\phi^{\,4}}\left\{\left(24\pi^2\alpha\gamma - 4\right)\hat{\omega}^4 + \omega_\phi^{\,2}\hat{\omega}^2\left[4\left(5F + 2 - 3\pi^2 l_3\right)\right.\right. \\
&\left.\left. -32\alpha^2\right] + \omega_\phi^{\,4}\left[9M^2 + 12\pi^2(F+1)l_3 - 4(F+1)(4F+1)\right]\right\}
\end{aligned}
$$

$$\cdot\left[M_z\, z_{am}\sin(\varepsilon_z)+M_\theta\,\theta_{am}\sin(\varepsilon_\theta)\right]$$

$$+\frac{192\pi^2}{25M\,l_5^{\,2}}\left[\left(M_z^{\,2}\,z_{am}^{\,2}+2M_\theta^{\,2}\,\theta_{am}^{\,2}\right)M_z\,z_{am}\sin(\varepsilon_z)\right.$$

$$\left.+\left(2M_z^{\,2}\,z_{am}^{\,2}+M_\theta^{\,2}\,\theta_{am}^{\,2}\right)M_\theta\,\theta_{am}\sin(\varepsilon_\theta)\right]$$

$$+\frac{768\pi^2}{25M^2\,l_5^{\,2}\,\omega_\phi^{\,4}}\left\{2\pi^2\,\alpha\,\gamma\,\hat{\omega}^4+\omega_\phi^{\,2}\,\hat{\omega}^2\left(F-\pi^2\,l_3\right)\right.$$

$$\left.+\omega_\phi^{\,2}\left[M^2-(F+1)\left(F-\pi^2\,l_3\right)\right]\right\}M_z\,z_{am}\,M_\theta\,\theta_{am}\cos(\varepsilon_z-\varepsilon_z)$$

$$-\frac{384\pi^2}{25l_5^{\,2}}M_z\,z_{am}\,M_\theta\,\theta_{am}\cos(\varepsilon_z+\varepsilon_z)$$

$$-\frac{192\pi^2}{25l_5^{\,2}}\left[M_z^{\,2}\,z_{am}^{\,2}\cos(2\varepsilon_z)+M_\theta^{\,2}\,\theta_{am}^{\,2}\cos(2\varepsilon_\theta)\right]$$

$$+\frac{192\pi^2}{25M\,l_5^{\,2}}M_z\,z_{am}\,M_\theta\,\theta_{am}$$

$$\cdot\left[M_z\,z_{am}\sin(2\varepsilon_z-\varepsilon_\theta)+M_\theta\,\theta_{am}\sin(2\varepsilon_\theta-\varepsilon_z)\right], \qquad (2.4.4.13)$$

$$b_4=a_4-\frac{8}{25M^2\,l_5^{\,2}\,\omega_\phi^{\,2}}\left(M_z^{\,2}\,z_{am}^{\,2}+M_\theta^{\,2}\,\theta_{am}^{\,2}\right)\left\{18\pi^4\,\gamma^2\,\hat{\omega}^6\right.$$

$$\left.-40\pi^4\,l_5\,\hat{\omega}^2+\omega_\phi^{\,2}\left[17M^2-40\pi^4\,l_5\,(F+1)-18\left(F-\pi^2\,l_3\right)^2\right]\right\}$$

$$+\frac{192\left[\pi^2\,\gamma\,\hat{\omega}^5-\pi^2\,\gamma\,\omega_\phi^{\,2}\,\hat{\omega}^3\,(F+1)+2\alpha\,\omega_\phi^{\,2}\,\hat{\omega}\left(F-\pi^2\,l_3\right)\right]}{25M\,l_5^{\,2}\,\omega_\phi^{\,4}}$$

$$\cdot\left[M_z\,z_{am}\cos(\varepsilon_z)+M_\theta\,\theta_{am}\cos(\varepsilon_\theta)\right]$$

$$+\frac{32}{25M\,l_5^{\,2}\,\omega_\phi^{\,4}}\left\{9\pi^4\,\gamma^2\,\hat{\omega}^6-48\pi^2\,\alpha\,\gamma\,\hat{\omega}^4\right.$$

$$-4\omega_\phi^{\,2}\,\hat{\omega}^2\left(3F-3\pi^2\,l_3+5\pi^4\,l_5\right)$$

$$\left.+\omega_\phi^{\,4}\left[9\pi^4\,l_3^{\,2}-6\pi^2\,l_3\,(5F+2)+3F\,(7F+4)-13M^2\right]\right\}$$

$$\cdot\left[M_z\,z_{am}\sin(\varepsilon_z)+M_\theta\,\theta_{am}\sin(\varepsilon_\theta)\right]$$

$$+\frac{16}{25M^2\,l_5^{\,2}\,\omega_\phi^{\,2}}\left(18\pi^4\,\gamma^2\,\hat{\omega}^6-40\pi^4\,l_5\,\omega_\phi^{\,2}\,\hat{\omega}^2+40\pi^4\,l_5\,\omega_\phi^{\,4}\right)$$

$$\cdot M_z\,z_{am}\,M_\theta\,\theta_{am}\cos(\varepsilon_z-\varepsilon_z)$$

$$+\frac{144}{25M^2\,l_5^{\,2}}M_z\,z_{am}\,M_\theta\,\theta_{am}\cos(\varepsilon_z+\varepsilon_z)$$

$$+\frac{72}{25l_5^{\,2}}\left[M_z^{\,2}\,z_{am}^{\,2}\cos(2\varepsilon_z)+M_\theta^{\,2}\,\theta_{am}^{\,2}\cos(2\varepsilon_\theta)\right], \qquad (2.4.4.14)$$

$$
\begin{aligned}
b_6 = a_6 &- \frac{48\pi^2\left(F-\pi^2 l_3\right)}{5M^2 l_5}\left(M_z{}^2 z_{am}{}^2 + M_\theta{}^2 \theta_{am}{}^2\right) \\
&+ \frac{16}{25M l_5{}^2 \omega_\phi{}^2}\left[9\gamma\left(F-\pi^2 l_3\right)\hat{\omega}^3 - 20\pi^2 \alpha l_5 \hat{\omega}\right] \\
&\qquad \cdot\left[M_z z_{am}\cos\left(\varepsilon_z\right) + M_\theta \theta_{am}\cos\left(\varepsilon_\theta\right)\right] \\
&+ \frac{16}{25\pi^2 M l_5{}^2 \omega_\phi{}^4}\left\{-18\pi^4\gamma^2\hat{\omega}^6 + 20\pi^4 l_5 \omega_\phi{}^2 \hat{\omega}^2\right. \\
&\quad \left. + \omega_\phi{}^4\left[10\pi^4 l_5\left(-2-5F+3\pi^2 l_3\right) + 6M^2 - 9\left(F-\pi^2 l_3\right)^2\right]\right\} \\
&\qquad \cdot\left[M_z z_{am}\sin\left(\varepsilon_z\right) + M_\theta \theta_{am}\sin\left(\varepsilon_\theta\right)\right] \\
&- \frac{96\pi^2}{5M^2 l_5}\left(F-\pi^2 l_3\right) M_z z_{am} M_\theta \theta_{am}\cos\left(\varepsilon_z - \varepsilon_z\right), \qquad (2.4.4.15)
\end{aligned}
$$

$$
\begin{aligned}
b_8 = a_8 &+ \frac{4\pi^4}{M^2}\left(M_z{}^2 z_{am}{}^2 + M_\theta{}^2 \theta_{am}{}^2\right) \\
&- \frac{24\pi^2\gamma\hat{\omega}^3}{5l_5 M \omega_\phi{}^2}\left[M_z z_{am}\cos\left(\varepsilon_z\right) + M_\theta \theta_{am}\cos\left(\varepsilon_\theta\right)\right] \\
&+ \frac{8}{5M l_5}\left(6F - 6\pi^2 l_3 + 5\pi^4 l_5\right) \\
&\qquad \cdot\left[M_z z_{am}\sin\left(\varepsilon_z\right) + M_\theta \theta_{am}\sin\left(\varepsilon_\theta\right)\right] \\
&+ \frac{8\pi^4}{M^2} M_z z_{am} M_\theta \theta_{am}\cos\left(\varepsilon_z - \varepsilon_z\right), \qquad (2.4.4.16)
\end{aligned}
$$

$$
b_{10} = a_{10} - \pi^6 M l_5{}^2\left[M_z z_{am}\sin\left(\varepsilon_z\right) + M_\theta \theta_{am}\sin\left(\varepsilon_\theta\right)\right], \qquad (2.4.4.17)
$$

$$
b_{12} = 1, \qquad (2.4.4.18)
$$

$$
b_k = 0 \quad \text{for } k = 1, 3, ..., 11, \qquad (2.4.4.19)
$$

where

$$
F = \frac{GM_{mean}}{GM}, \quad M = \frac{GM_{amp}}{GM}, \quad M_z = \frac{GM_z}{GM}, \quad M_\theta = \frac{GM_\theta}{GM}. \qquad (2.4.4.20)
$$

The terms a_k are available in Eq. 2.4.1.11 to 2.4.1.18, which are the coefficients of parametric roll amplitude in longitudinal waves estimated by an averaging method without taking the effect of vertical motion into account. Figure 2.4.4.1 shows a comparison between the 1-dof averaging method proposed by Umeda et al., 3-dof averaging method, and experiment. In the calculation, the added mass, wave damping coefficient, restoring coefficient, and diffraction force of heave and pitch are derived by a linear ordinary strip method (OSM), which is introduced in subsection 3.3.2. The roll damping is estimated by Ikeda's simplified method (Kawahara et al., 2012) with the lift

component of Ikeda's original method (Ikeda, 2004), the natural roll frequency and roll inertia moment are estimated from roll decay test by using a ship model of the C11-class post-Panamax container ship, and the restoring moment is estimated hydrostatically based on the Froude Krylov assumption by assuming that heave and pitch change quasi-statically. (See appendix subject ships about the ships, coefficients, and experiments.) The experimental results in regular heading waves are obtained from free running model experiment at the national research institute of fisheries engineering (NRIFE) (Morimoto, 2012). The 1-dof averaging method overestimates the experiment especially around *Fn* of zero. On the other hand, the 3-dof averaging method can explain the decrease of amplitude.

In order to analyze the reason why the estimation of the parametric roll amplitude is improved, the GM variations in the calculations are shown in Fig. 2.4.3.2-3. Figure 2.4.3.2 shows that the GM variation in the 3-dof averaging method is smaller than that of the 1-dof averaging method. This decrease of GM variation is the reason of the good agreement around *Fn* of 0.0. Figure 2.4.3.3 shows the GM variation of each component used in the 3-dof averaging method. The GM variation due to pitch clearly decreases the GM variation in total. The heave and pitch motions in both calculations are shown in Fig. 2.4.3.4-5. They clearly show the difference of the vertical motions taken into account in each model. In the 1-dof averaging method, which is based on the quasi-static vertical motions, the heave motion is heavy but the pitch motion is not so. On the other hand, in the 3-dof averaging method, which is based on the dynamic vertical motions, no significant heave motion can be seen but the pitch motion is relatively large. Furthermore, the phase of the pitch motions are almost opposite in the two cases. These differences are the reason of the GM variation.

Figure 2.4.4.1 also shows that the amplitude estimated by the 3-dof averaging method asymptotically approaches that of the 1-dof averaging method in higher speed cases. Firstly, comparisons of the GM variation, heave, and pitch in the case of *Fn* of –0.15 are shown in Fig. 2.4.4.6-8. They show almost the same quantities with those of *Fn* of 0.0 as shown in Fig. 2.4.4.2, 4-5. The total GM variations considered in both models are shown with *Fn* in Fig. 2.4.4.9. The GM_{amp} of the 3-dof averaging method is calculated as a sum of wave, heave, and pitch components with taking the phases into account. Although it clearly shows that the amplitude of the GM variation in the 3-dof averaging method decreases in higher speed as shown in Fig. 2.4.4.9, the response curve of the 3-dof approaches to the 1-dof as shown in Fig. 2.4.4.1. This can be explained by the nonlinearity of parametric roll responses. Figure 2.4.4.10 shows parametric roll amplitude calculated with changing GM_{amp} and *Fn* based on the method of Umeda et al. Here, the value of GM_{mean} is the same as that of the 3-dof averaging method with λ/L of 1.0 and H/λ of 0.04 and GM_{amp} is changed from 2.3 to 3.0 [m], in which the GM_{amp} in the 3-dof shown in Fig. 2.4.4.9 is included. This figure shows that the parametric roll amplitude strongly depends on the GM_{amp} around *Fn* of 0.0. This is because the peak of parametric roll shifts towards the right as shown in Fig. 2.4.4.10 due to a hard-type GZ curve of the C11-class post-Panamax containership as shown in appendix subject ships. In this sense, it is very difficult to estimate parametric roll around the right part of unstable region (or a left part of an unstable region for a ship with a soft-type GZ curve).

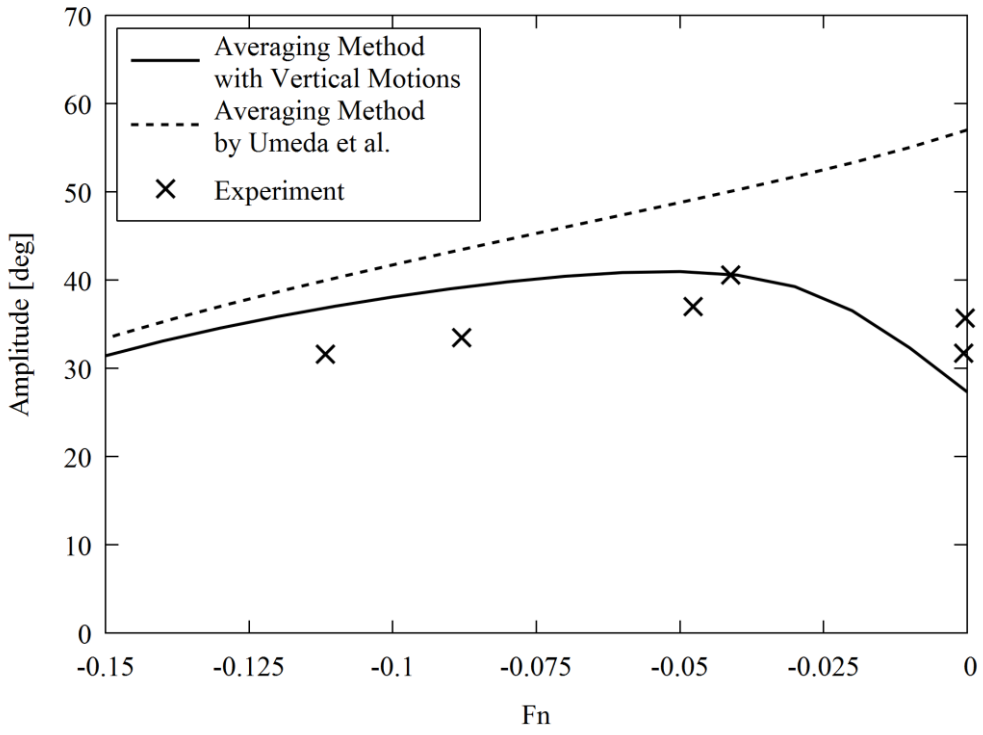

Figure 2.4.4.1 Parametric roll amplitude with λ/L of 1.0 and H/λ of 0.04 in heading waves.

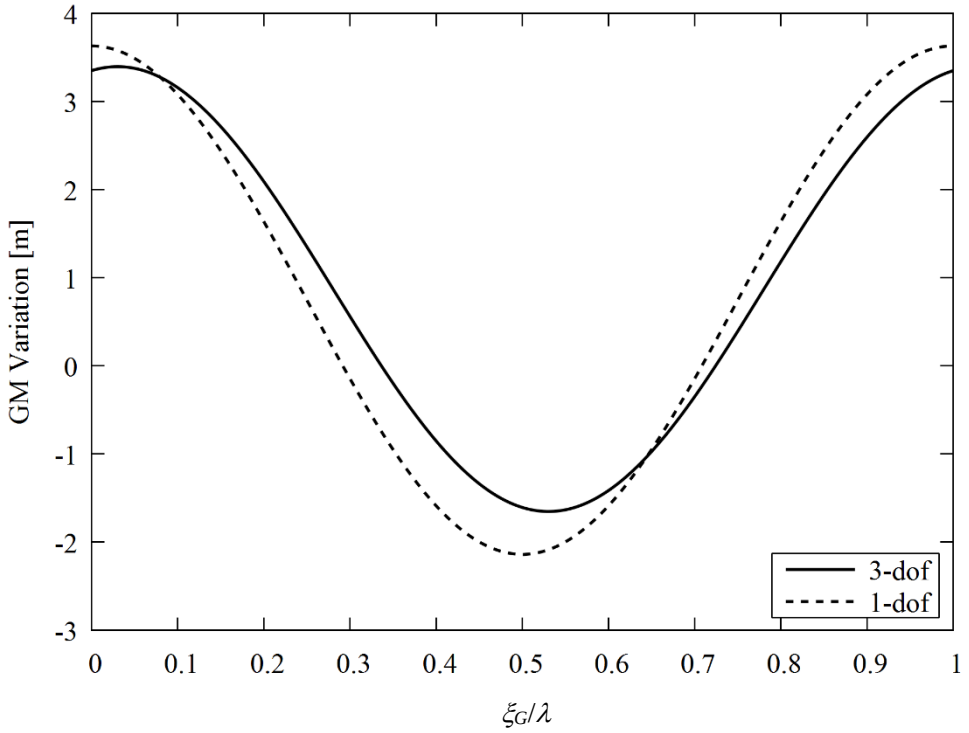

Figure 2.4.4.2 Comparison of the GM variation in the two calculations with λ/L of 1.0, H/λ of 0.04, and Fn of 0.0.

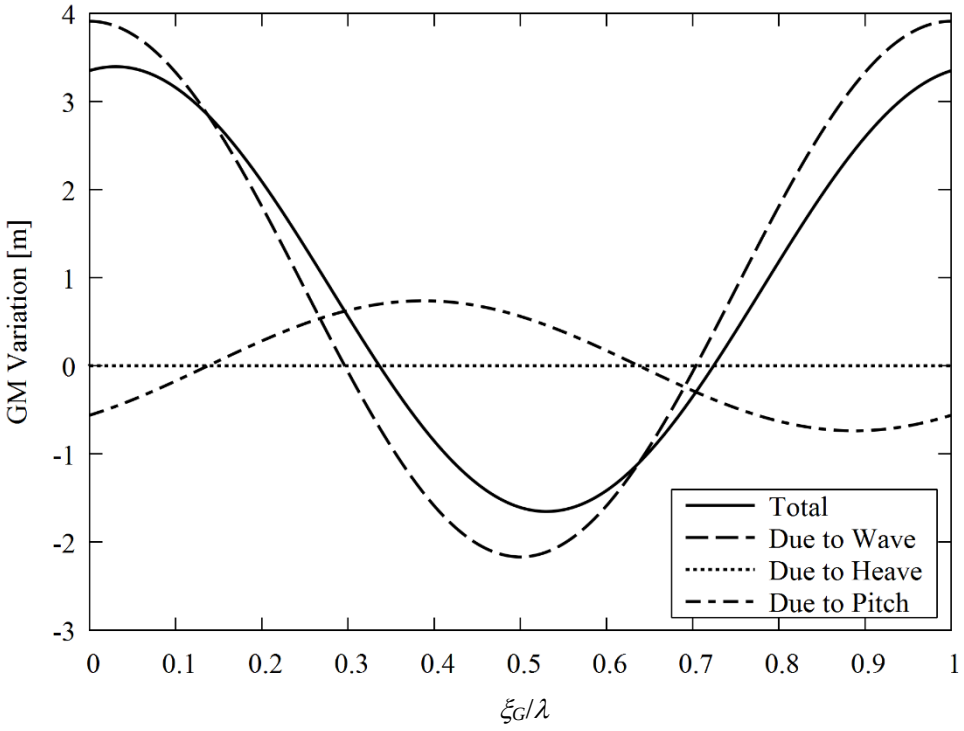

Figure 2.4.4.3 GM variation of each component with λ/L of 1.0, H/λ of 0.04, and *Fn* of 0.0.

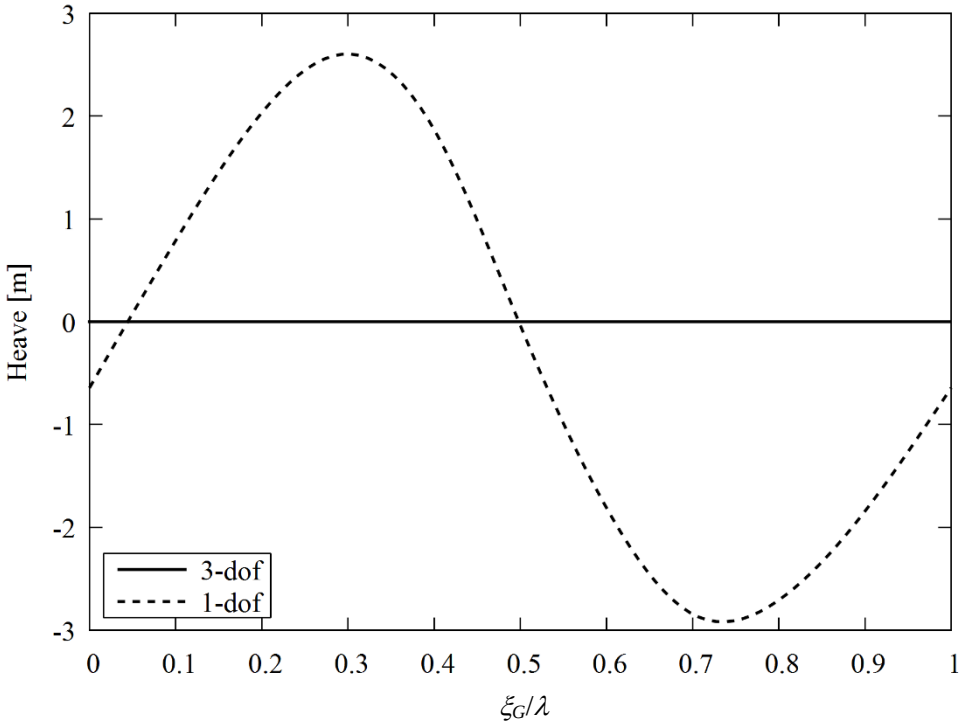

Figure 2.4.4.4 Comparison of the heave in the two calculations with λ/L of 1.0, H/λ of 0.04, and *Fn* of 0.0.

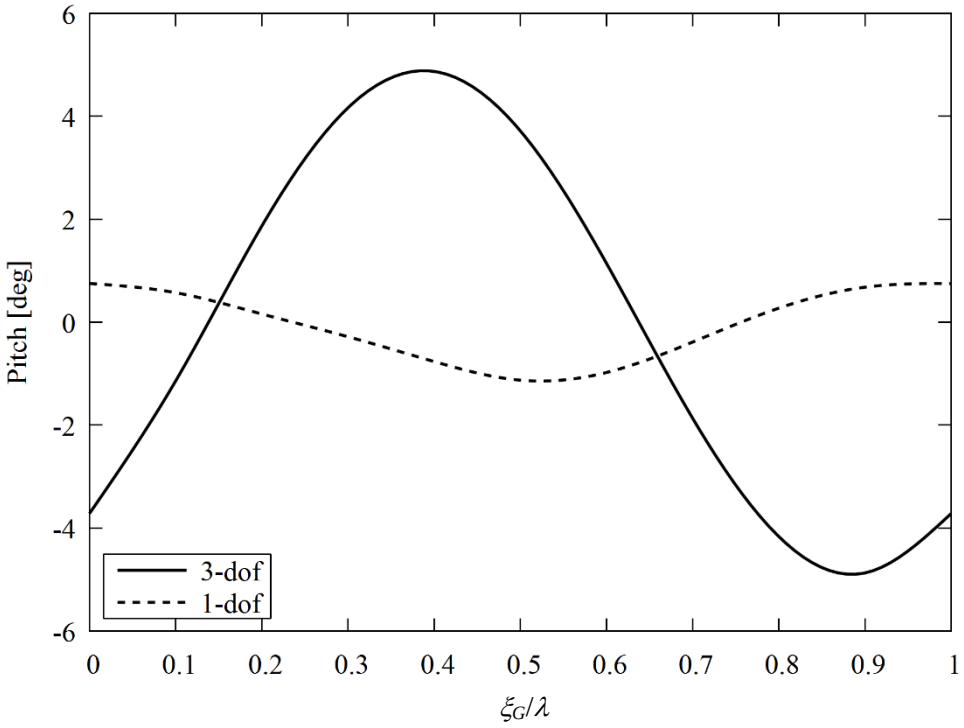

Figure 2.4.4.5 Comparison of the pitch in the two calculations with λ/L of 1.0, H/λ of 0.04, and *Fn* of 0.0.

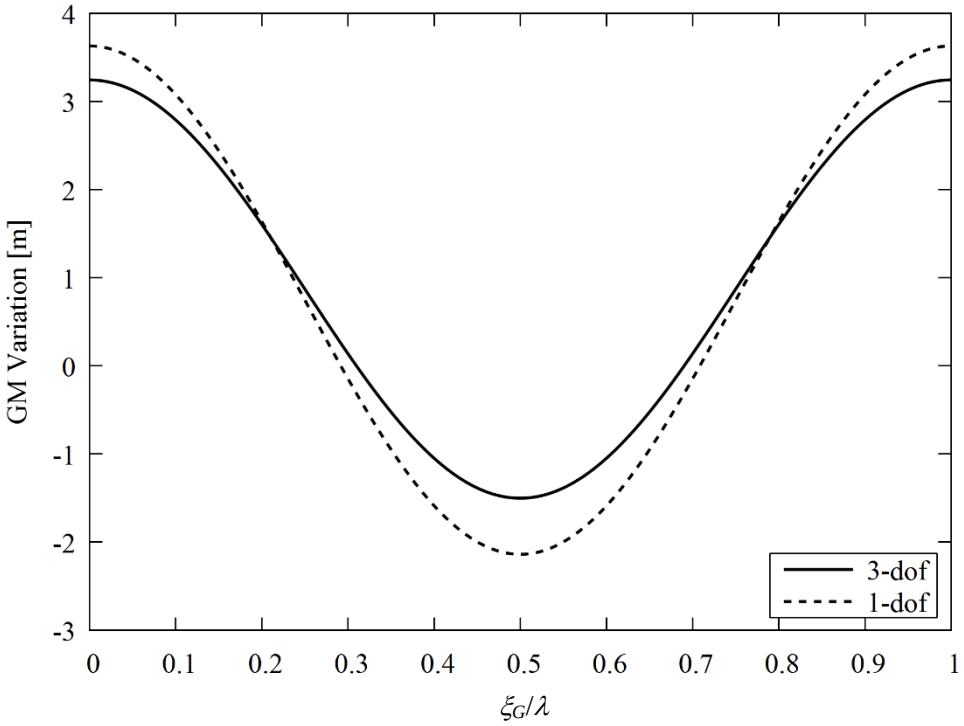

Figure 2.4.4.6 Comparison of the GM variation in the two calculations with λ/L of 1.0, H/λ of 0.04, and *Fn* of –0.15.

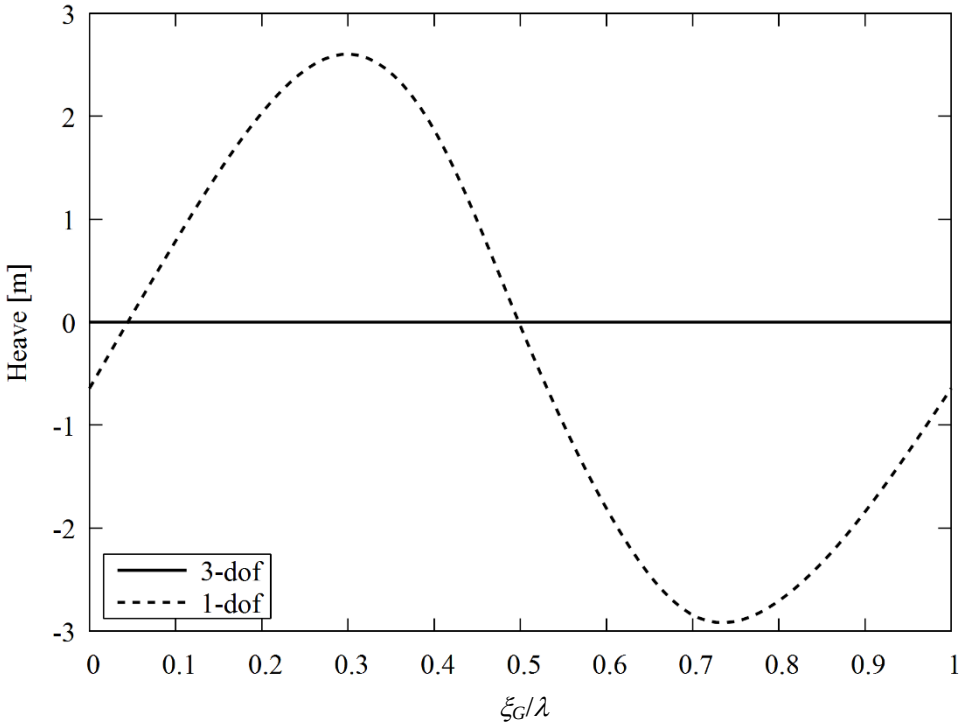

Figure 2.4.4.7 Comparison of the heave in the two calculations with λ/L of 1.0, H/λ of 0.04, and Fn of –0.15.

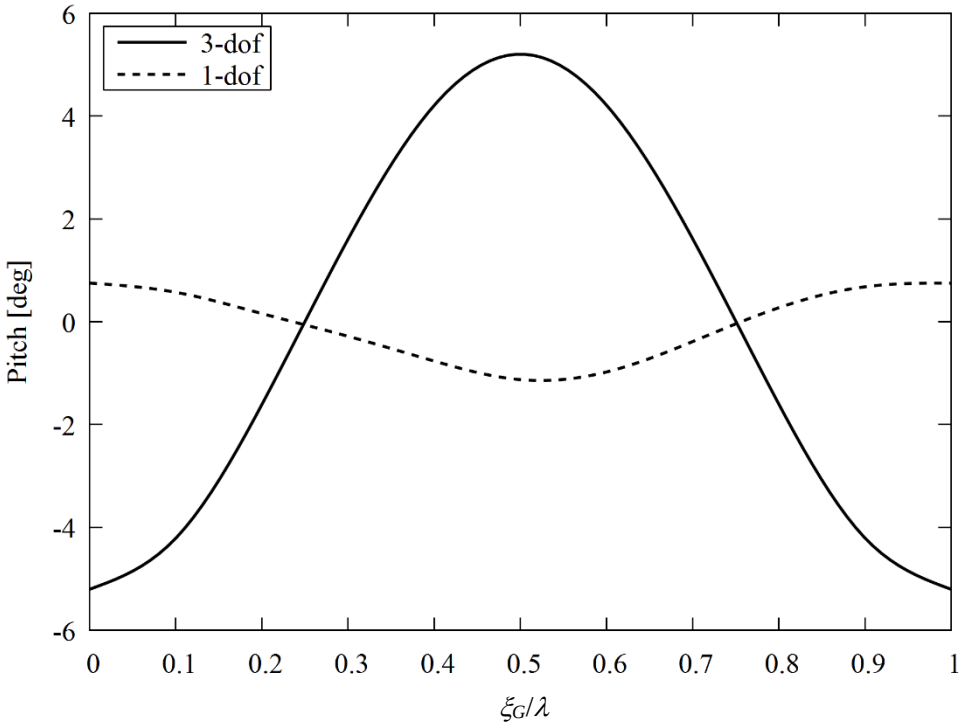

Figure 2.4.4.8 Comparison of the pitch in the two calculations with λ/L of 1.0, H/λ of 0.04, and Fn of –0.15.

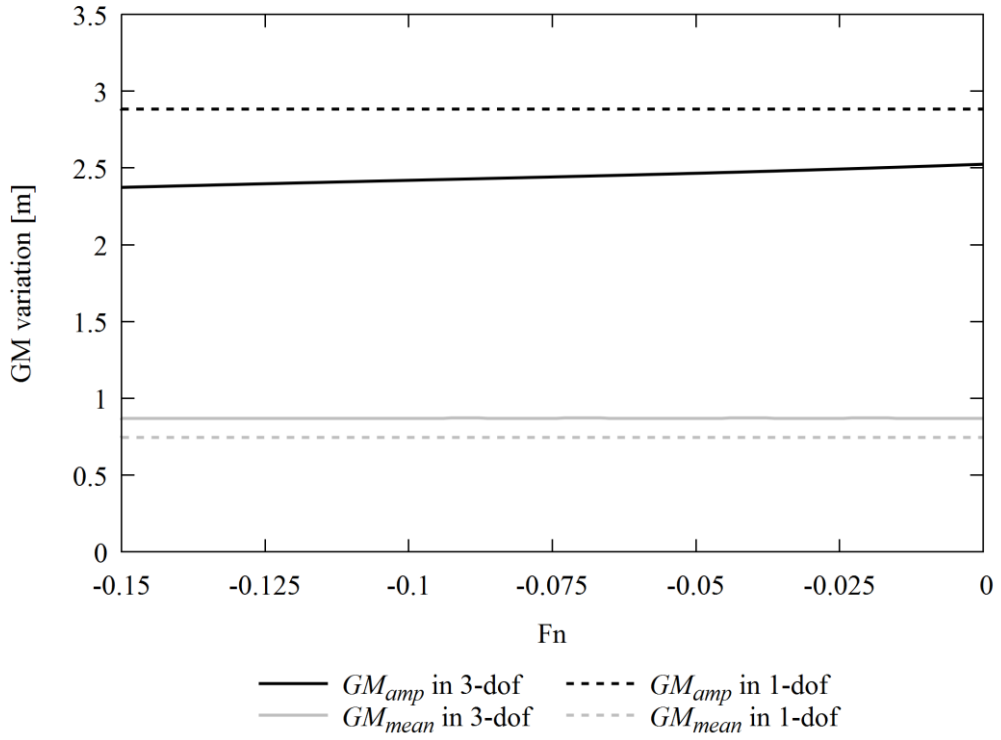

Figure 2.4.4.9 Comparison of the GM variations in the two calculations with λ/L of 1.0 and H/λ of 0.04.

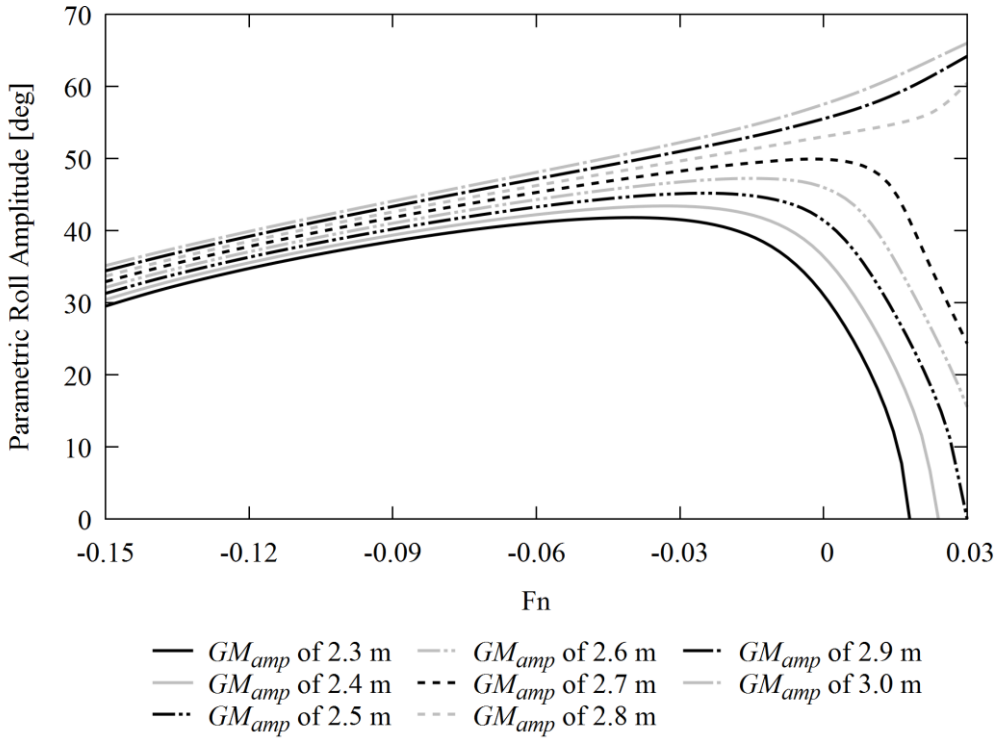

Figure 2.4.4.10 Parametric roll amplitude with various GM_{amp} and Fn.

2.5 Application to Design Criteria

As Paulling (1972) stated, the vulnerability for parametric roll is examined by the occurrence probability of critical waves in the draft second check of the second generation intact stability criteria (IMO, 2015). The draft second check adopted the Grim's effective wave (1961) to convert irregular incident waves to regular longitudinal waves.

2.5.1 Parametric Roll in Irregular Waves

In order to deal with parametric roll in irregular waves, Grim's effective wave concept is useful. Generally speaking, since parametric roll is a resonance, three or more waves are required to grow the parametric roll amplitude and the required number of waves depends on the roll damping and magnitude of restoring variation. Hence, the important point is to estimate how high and frequent "continuous" waves can be expected in the irregular waves. In other words, a "single" steep wave is not so dangerous for parametric roll. In the draft second check, the Grim's wave height is determined as a significant wave height of Grim's effective wave spectrum as shown in subsection 2.5.1.1. Once the height of incident waves is determined, the parametric roll amplitude is obtained according to the roll model in regular waves.

2.5.1.1 Grim's Effective Wave Concept

In the section 2.3, the governing equation of parametric roll in regular waves are introduced. In this section, how to convert short-crested irregular waves into an equivalent regular longitudinal wave is introduced based on the extended Grim's effective wave concept (Umeda & Yamakoshi, 1992). Grim proposed that how to convert long-crested irregular waves into an equivalent regular longitudinal wave (Grim, 1961), and Umeda and Yamakoshi (1992) expanded the concept to short-crested irregular waves.

The length of the equivalent regular longitudinal wave is equal to the ship length between perpendiculars L_{pp}. The effective wave amplitude ζ_{ae} is calculated by the least squares method as Eq. 2.5.1.1.1:

$$\zeta_{ae} = G\left(\omega, L_{pp}, \chi\right) \cdot \zeta_a , \tag{2.5.1.1.1}$$

$$G\left(\omega, L_{pp}, \chi\right) = \frac{2\pi \frac{L_{pp}}{\lambda}\cos\left(\chi\right)\sin\left(\pi \frac{L_{pp}}{\lambda}\cos\left(\chi\right)\right)}{\pi^2 - \left(\pi \frac{L_{pp}}{\lambda}\cos\left(\chi\right)\right)^2}, \tag{2.5.1.1.2}$$

where λ is the wavelength and ζ_a is the wave amplitude. Then, a spectrum of irregular waves is converted to Grim's effective wave spectrum as Eq. 2.5.1.1.3:

$$S\eta_{eff}\left(\omega, L_{pp}, \alpha\right) = \left[G\left(\omega, L_{pp}, \chi\right)\right]^2 S_w\left(\omega, \alpha\right), \tag{2.5.1.1.3}$$

where α is a wave propagating direction for each individual wave and $S_w(\omega, \alpha)$ and $S\eta_{eff}(\omega, L_{pp}, \alpha)$ are an incident wave spectrum and Grim's effective wave spectrum, respectively. Here, the

significant effective wave height based on the ITTC spectrum is derives as Eq. 2.5.1.1.4 (IMO, 2016):

$$H_{eff} = 4.0043\sqrt{m_0}\ ,\ \ m_n = \int_{\alpha=-\pi/2}^{\alpha=\pi/2}\int_{\omega=0}^{\omega=\infty} \omega^n\, S\eta_{eff}\left(\omega, L_{pp}, \alpha\right) d\omega\, d\alpha\ ,$$
$$S_w(\omega) = \left(173 H_s{}^2\, T_{01}{}^{-4}\right)\omega^{-5} \exp\left(-\left(691 T_{01}{}^{-4}\right)\omega^{-4}\right),\ \ T_{01} = 1.086 T_z\ , \qquad (2.5.1.1.4)$$

where H_{eff} is the Grim's effective wave height, m_n is n-th moment of Grim's effective wave spectrum, H_s is a significant wave height [m] and T_z is a zero-crossing mean wave period [s]. The terms H_s and T_z are given from a wave scatter diagram in the North Atlantic Ocean in the draft second check. The zero-upcrossing mean wave encounter frequency, $\bar{\omega}_e$, is defined as a zero-upcrossing mean frequency as Eq. 2.5.1.1.5:

$$\bar{\omega}_e = \sqrt{\frac{\int_0^\infty \left(\omega - \frac{\omega^2}{g} u\cos\chi\right)^2 S\eta_{eff}\left(\omega, L_{pp}, \chi\right) d\omega}{\int_0^\infty S\eta_{eff}\left(\omega, L_{pp}, \chi\right) d\omega}}\ . \qquad (2.5.1.1.5)$$

where u is the ship speed. On the other hand, the current draft uses Eq. 2.5.1.1.6 instead of Eq. 2.5.1.1.5:

$$\omega_e = \omega_L - \frac{\omega_L{}^2}{g} u\cos\chi\ , \qquad (2.5.1.1.6)$$

where

$$\omega_L = \sqrt{\frac{2\pi g}{L_{pp}}}\ . \qquad (2.5.1.1.7)$$

Equation 2.5.1.1.7 is the dispersion relationship of deep water wave whose length is equal to the ship length.

2.5.2 Estimation of Critical Ship Speed

In above sections, averaging methods are treated as a tool to calculate parametric roll amplitude under a certain condition. However, the averaged equations can be regarded as equations that include all the solutions of parametric roll under all conditions, so that the averaged equations can provide more useful information than just an amplitude under a certain condition. In this section, critical ship speed is estimated by using the method of Umeda et al. (2004), Eq. 2.4.1.10 to 2.4.1.18. Here, the critical ship speed is defined as the ship speed with which parametric roll amplitude is maximized in a certain wave. The maximum parametric roll can appear when a partial derivative of parametric roll amplitude with a ship speed is zero. Then, the critical speed is obtained by solving the averaged equations under the condition that the partial derivative is zero. Let the equation of the amplitude, eq. 2.4.1.10, be rewritten as Eq. 2.5.2.1:

$$\sum_{k=0}^{12} a_k A^k = 0 \ . \tag{2.5.2.1}$$

Differentiating Eq. 2.5.2.1 with respect to a ship speed U yields:

$$\sum_{k=0}^{12} \frac{\partial a_k}{\partial U} A^k + \frac{\partial A}{\partial U} \sum_{k=0}^{12} a_k \, k \, A^{k-1} = 0 \, . \tag{2.5.2.2}$$

Applying a condition of stationary (i.e., that the partial derivative of A with respect to the ship speed is zero) yields:

$$\sum_{k=0}^{12} \frac{\partial a_k}{\partial U} A^k = 0 \, . \tag{2.5.2.3}$$

The only coefficients included in Eq. 2.5.2.1 that depend on the ship speed are the linear damping coefficient and the wave-encounter frequency. The partial derivatives of a_k with respect to the ship speed are given in subsection 2.5.2.1. Solving Eq. 2.5.2.1 and 2.5.2.3 simultaneously gives the critical ship speed.

Figure 2.5.2.1 shows validation of the critical speed for parametric roll by using ONR Flare topside vessel, a C11-class post-Panamax container ship, and ITTC A-1 container ship (used data are listed in appendix subject ships). In the calculation, the roll damping is estimated by Ikeda's simplified method (Kawahara et al., 2012) with the lift component of Ikeda's original method (Ikeda, 2004), the natural roll frequency and roll inertia moment are estimated from roll decay test by using ship models, and the restoring moment is hydrostatically estimated in longitudinal waves based on Froude Krylov assumption by assuming that heave and pitch change quasi-statically. (See appendix subject ships about the ships, coefficients, and experiments.) Each calculated critical speed is the relevant peak value of the existing averaging method, so that the critical speed is not overlooked by using this method.

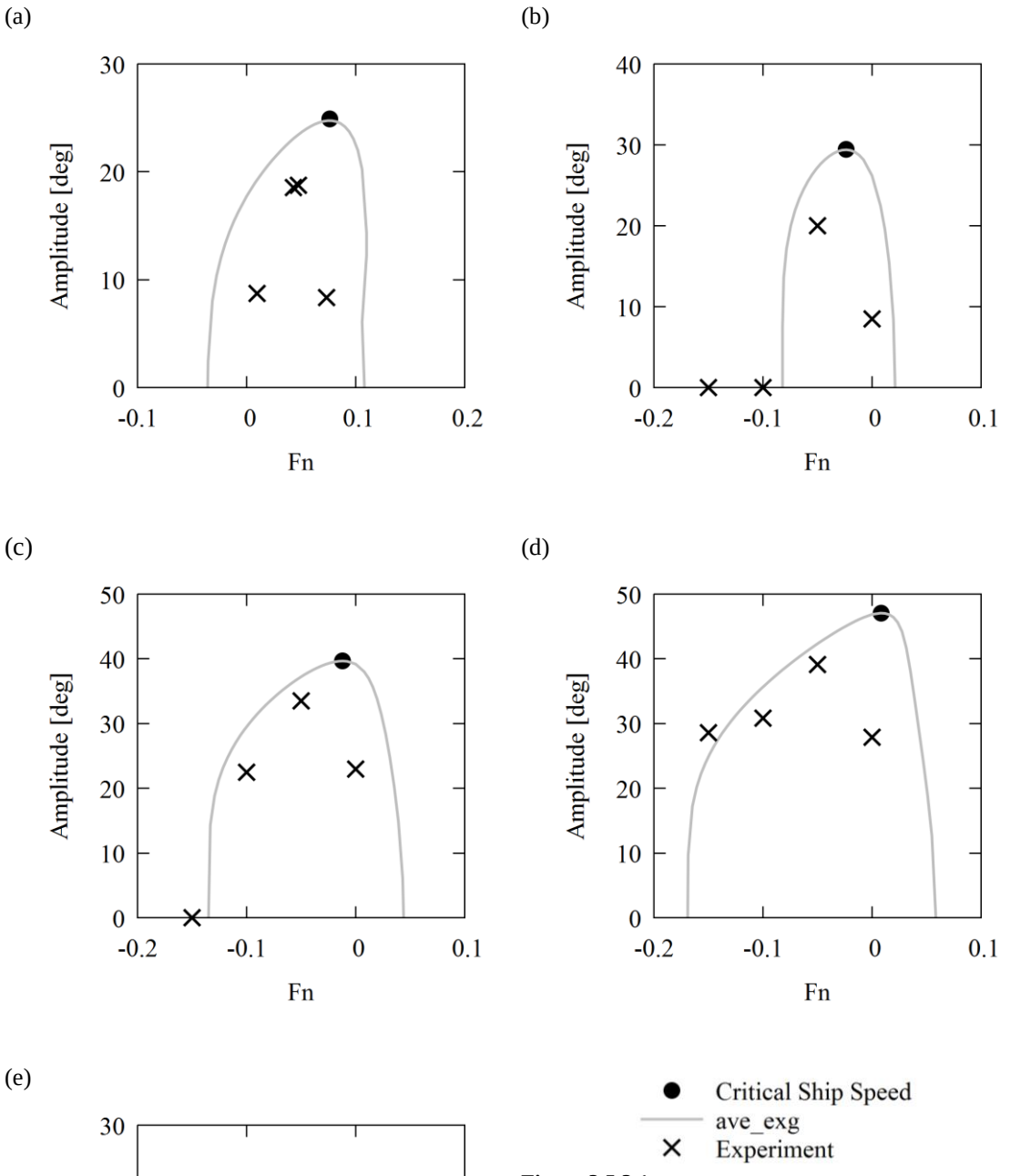

Figure 2.5.2.1
Comparison of parametric roll amplitudes and the critical ship speed in longitudinal waves:

(a) ONR flare topside vessel with a wave steepness of 0.04;
(b) C11-class post-Panamax container ship with a wave steepness of 0.01;
(c) C11-class post-Panamax container ship with a wave steepness of 0.02;
(d) C11-class post-Panamax container ship with a wave steepness of 0.03;
(e) ITTC A-1 container ship with a wave steepness of 0.03.

2.5.2.1 Derivatives of Coefficients

The coefficients that depend on the ship speed are the parametric roll frequency and the linear damping coefficient. Their derivatives with respect to the ship speed are as Eq. 2.5.2.1.1-2:

$$\frac{\partial}{\partial U}(\hat{\omega}) = \frac{\partial}{\partial U}\left(\frac{1}{2}\omega_e\right)$$
$$= \frac{\partial}{\partial U}\left\{\frac{1}{2}\left(\omega_k - \frac{2\pi}{\lambda}U\cos(\chi)\right)\right\} = -\frac{\pi}{\lambda}\cos(\chi), \tag{2.5.2.1.1}$$

$$\frac{\partial}{\partial U}(\alpha) = \frac{\partial}{\partial U}(C_1 U + C_2) = C_1. \tag{2.5.2.1.2}$$

Here, ω_k is the wave frequency. The roll damping consists of a term that is proportional to the ship speed $C_1 U$ and ship-speed-independent term C_2. Then, the partial derivatives of a_k with respect to the ship speed are as Eq. 2.5.2.1.3 to 2.5.2.1.10:

$$\frac{\partial a_0}{\partial U} = \frac{1024\pi^4}{25 l_5^{\,2}\,\omega_\phi^{\,4}}\left\{-\hat{\omega}^3\frac{\pi}{\lambda}\cos(\chi) + 2\hat{\omega}^2\alpha C_1 + \hat{\omega}\frac{\pi}{\lambda}\cos(\chi)\left[-2\alpha^2 + \omega_\varphi^{\,2}(1+F)\right]\right\}, \tag{2.5.2.1.3}$$

$$\frac{\partial a_2}{\partial U} = \frac{256\pi^2}{25 l_5^{\,2}\,\omega_\phi^{\,4}}\left\{3\pi^2\hat{\omega}^4 C_1\gamma - 4\hat{\omega}^3\frac{\pi}{\lambda}\cos(\chi)\left(3\pi^2\alpha\gamma - 1\right) - 16\hat{\omega}^2\alpha C_1 - \hat{\omega}\frac{\pi}{\lambda}\cos(\chi)\left[-16\alpha^2 + \omega_\phi^{\,2}\left(-3\pi^2 l_3 + 7F + 4\right)\right]\right\}, \tag{2.5.2.1.4}$$

$$\frac{\partial a_4}{\partial U} = \frac{32}{25 l_5^{\,2}\,\omega_\phi^{\,4}}\left\{27\pi^4\hat{\omega}^5\frac{\pi}{\lambda}\cos(\chi)\gamma^2 - 24\pi^2\hat{\omega}^4 C_1 - 8\hat{\omega}^3\frac{\pi}{\lambda}\cos(\chi)\left(-24\pi^2\alpha\gamma + 1\right) + 64\hat{\omega}^2\alpha C_1 - 4\hat{\omega}\frac{\pi}{\lambda}\cos(\chi)\left[16\alpha^2 + \omega_\phi^{\,2}\left(6\pi^2 l_3 - 5\pi^4 l_5 - 8F - 2\right)\right]\right\}, \tag{2.5.2.1.5}$$

$$\frac{\partial a_6}{\partial U} = \frac{64}{25\pi^2 l_5^{\,2}\,\omega_\phi^{\,4}}\left[27\pi^4\hat{\omega}^5\gamma^2\frac{\pi}{\lambda}\cos(\chi) + 12\pi^2\hat{\omega}^4 C_1\gamma - 48\pi^2\hat{\omega}^3\frac{\pi}{\lambda}\cos(\chi)\alpha\gamma - \hat{\omega}\frac{\pi}{\lambda}\cos(\chi)\omega_\phi^{\,2}\left(-3\pi^2 l_3 + 10\pi^4 l_5 + 3F\right)\right], \tag{2.5.2.1.6}$$

$$\frac{\partial a_8}{\partial U} = \frac{32}{25\pi^4 l_5^{\,2}\,\omega_\phi^{\,4}}\left[-27\pi^4\hat{\omega}^5\frac{\pi}{\lambda}\cos(\chi)\gamma^2 + 5\hat{\omega}\frac{\pi}{\lambda}\cos(\chi)\omega_\phi^{\,2}\pi^4 l_5\right], \tag{2.5.2.1.7}$$

$$\frac{\partial a_{10}}{\partial U} = 0\,, \tag{2.5.2.1.8}$$

$$\frac{\partial a_{12}}{\partial U} = 0\,, \text{ and} \tag{2.5.2.1.9}$$

$$\frac{\partial a_k}{\partial U} = 0 \quad \text{for } k = 1,\ 3,\ ...,\ 11. \tag{2.5.2.1.10}$$

2.5.3 Effect of Wave Encounter Frequency

The amplitude of the wave-induced GM variation in irregular waves cannot be expressed as a superposition of GM variation due to each individual wave, so that Grim's effective wave (Grim, 1961) was introduced to the current draft second check of the second generation intact stability criteria for parametric roll. GM variation in irregular waves is converted to that in equivalent regular waves. By using this concept, the vulnerability for parametric roll is estimated in regular longitudinal waves with changing her speed. For a simple criterion, the GM variation frequency is assumed to be equal to a wave encounter frequency that is estimated by using ship speed and wave frequency as Eq. 2.5.1.1.6 and 2.5.1.1.7. Since Grim's effective wave has the same length as the ship length, the wave frequency is calculated by the dispersion relationship of deep water waves whose length is equal to the ship length. However, the Grim's effective wave is not propagating waves. It is just a variation of wave surface whose profile is always along a cosine function. Thus, theoretically, the dispersion relationship cannot be applied to Grim's effective wave and a mean value of wave-encounter frequency should be calculated by using Grim's effective wave spectrum. In order to examine the frequency effect, parametric roll amplitude is estimated by using the mean frequencies of Grim's effective waves and the vulnerabilities derived by using the mean frequency and the current draft are compared. Finally, the results show good agreement, therefore it is shown that the assumption of the wave frequency is appropriate. In addition, it is shown that number of samples of operational conditions for ship courses should be at least 24. The above calculations are conducted based on the method of Umeda et al. (2004) as shown in section 2.4.1.

The current draft criteria of the second check of the level 2 of the second generation intact stability criteria for parametric roll adopts the 1-dof roll model as Eq. 2.4.1.4. Parametric roll is one of the roll resonance, so that the wave encounter frequency governs the amplitude, which depends on the ship speed and course. For simple criteria, the IMO adopted calculation only in irregular-longitudinal waves with several ship speeds u_k as Eq. 2.5.3.1:

$$u_k = u_{max} \cos\left(\frac{k}{n} \pi \right) \left(k = 0,1,2,...,n \right). \tag{2.5.3.1}$$

Here, u_{max} is the ship service speed and a positive and negative u_k indicates that the ship runs in following and heading waves, respectively. The ship speeds in the current draft are estimated as component speeds of her service speed in the wave propagating direction based on the assumption that a ship runs with her service speed in different directions and each course is chosen with the same probability. The reason why only a longitudinal wave is considered is that GM variation due to

waves has almost its maximum value in longitudinal waves. The wave properties are estimated by Grim's effective wave concept as shown in subsection 2.5.1.1. Therefore, vulnerability for parametric roll is examined in regular longitudinal waves by systematically changing her speed as Eq. 2.5.3.1 (IMO, 2015):

$$C2 = \frac{1}{n+1}\sum_{k=0}^{n} C2_k\left(u_k\right), \tag{2.5.3.2}$$

where

$$C2_k\left(u_k\right) = \sum_{i=1}^{N} W_i\, C_i\left(u_k\right). \tag{2.5.3.3}$$

Here, $C2$ is an occurrence probability of irregular wave case that is judged as dangerous and is to be used an index of the vulnerability criteria. The term n is a number of samples of operational conditions. The term W_i is the occurrence probability of i-th wave case and N is the number of wave cases. The term $C_i(u_k)$ is one when the parametric roll amplitude exceeds 25° in i-th case of waves with ship speed u_k and otherwise is zero.

The subject ship is the C11-class post-Panamax which suffered parametric roll in actual seas (France et al., 2003) and the ship data and calculation conditions are shown in appendix subject ships. Figures 2.5.3.1 and 2.5.3.2 show the comparison of $C2$ in Eq. 2.5.3.2 and $C2_k(u_k)$ in Eq. 2.5.3.3 derived by using the mean frequency of Grim's effective wave and wave frequency used in the draft second check. Here, the circles indicate results derived by using the mean frequency of Grim's effective wave and the x-marks do those derived by using the current draft second check. Figure 2.5.3.1 shows good agreement between the two for larger n. It clarifies that n = 6, which was tentatively adopted by the IMO (IMO, 2015), is not sufficient because the $C2$ value is clearly larger than the $C2$ values of more larger n, which can be more reliable. For n = 12 and 18, the discrepancy appears large, so that it is finally concluded that n should be at least 24 and the index of 0.06 for $C2$ should be reduced since this ship has to fail to pass the level 2. Figure 2.5.3.2 shows a slight shift of the peak of the current draft second check towards lower speed but it can be said that the difference between the two is not significant.

In order to investigate the reason why the simple assumption provides satisfactory approximations shown in Fig. 2.5.3.1 and 2.5.3.2, the mean frequencies of Grim's effective waves and the frequency assumed in the draft second check are compared in Fig. 2.5.3.3-5. Here, the significant wave heights and mean wave frequencies of Grim's effective waves are calculated for all sea states appearing in the North Atlantic. Calculated conditions in Fig. 2.5.3.3-5 are zero forward speed, the service speed in heading waves and the service speed in following waves. The horizontal axis indicates the nondimensionalized frequency with the encounter frequency assumed in the draft second check for each calculated condition. So, the gray vertical line, which is located at one in the horizontal axis, indicates the frequency assumed in the draft second check. For more than 2.0 [m] height effective waves in Fig. 2.5.3.3-5, the mean frequency is distributed only near that of the draft second check. This guarantees that the simple assumption that the wave frequency of λ/L_{pp} = 1 can represent the GM variation frequency. The reason of the agreement of encounter frequency shown in Fig. 2.5.3.3-

5 can be explained by Fig. 2.5.3.6. It indicates that the transfer function, $[G(\omega, L_{pp}, \chi]^2$, has the largest peak around the wave frequency of λ/L_{pp} = 1 and can also explain the groups around nondimensionalized wave encounter frequencies of 1.5, 2.0, and 2.5 in Fig. 2.5.3.3-5.

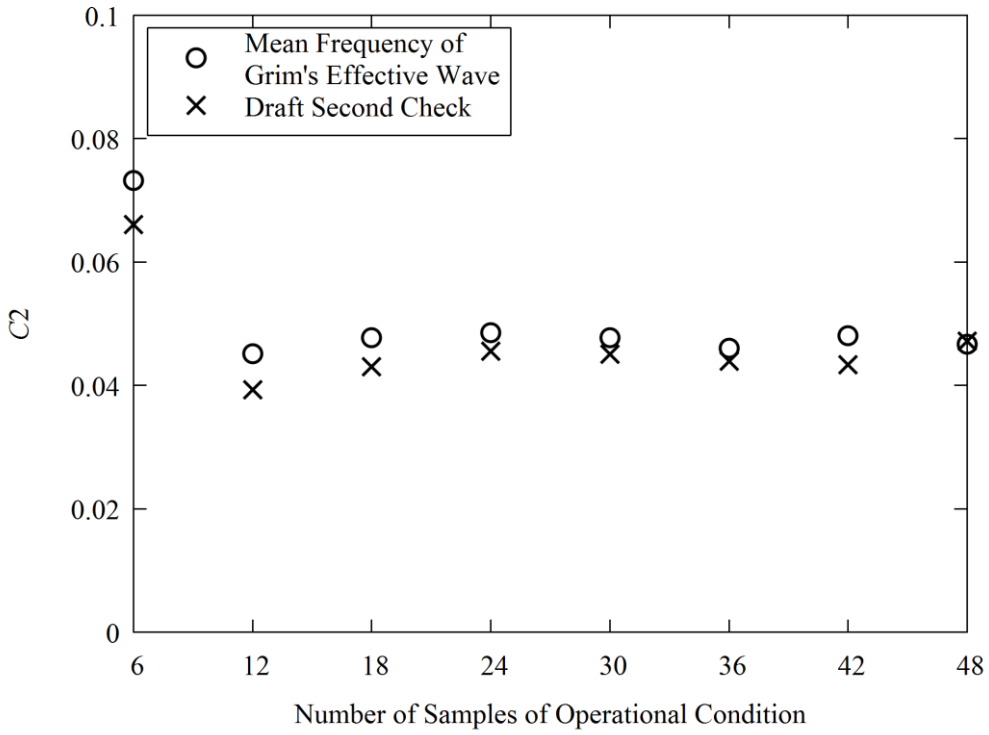

Figure 2.5.3.1 Comparison of *C*2 with number of samples of operational condition.

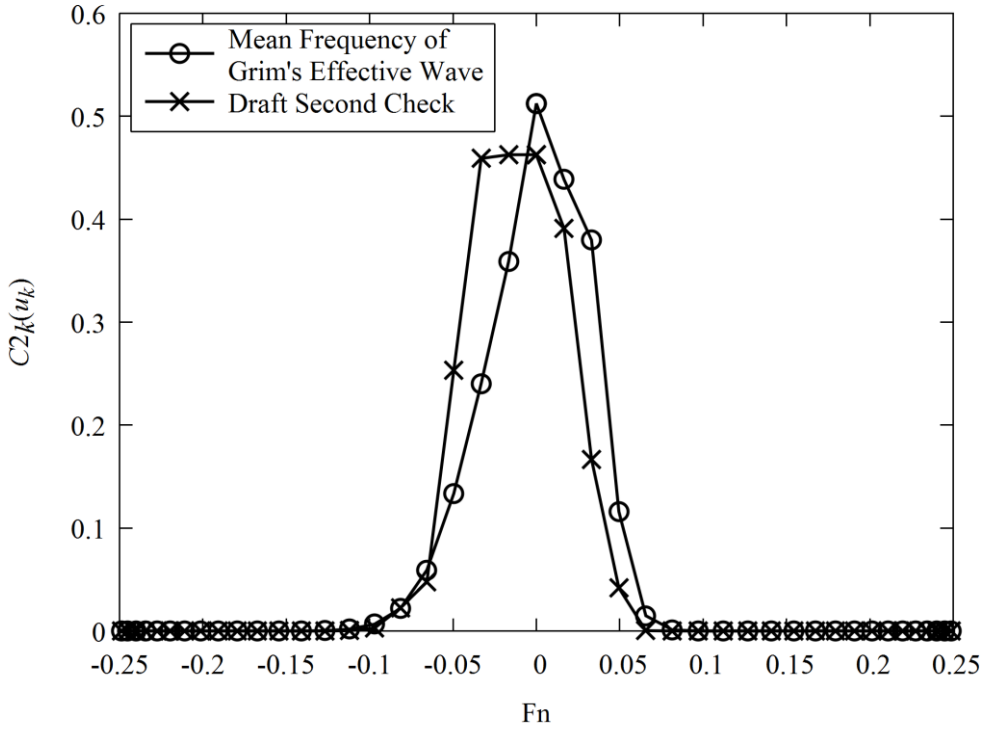

Figure 2.5.3.2 Comparison of $C2_k(u_k)$ when n = 48.

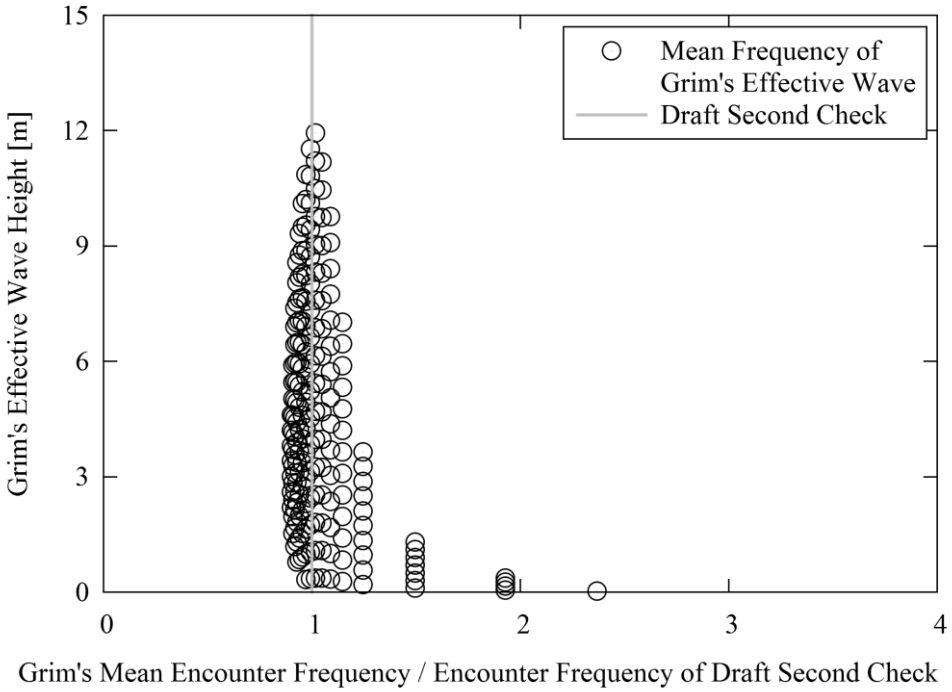

Figure 2.5.3.3 Relationship between the mean wave frequency and wave height of Grim's effective wave with zero forward speed.

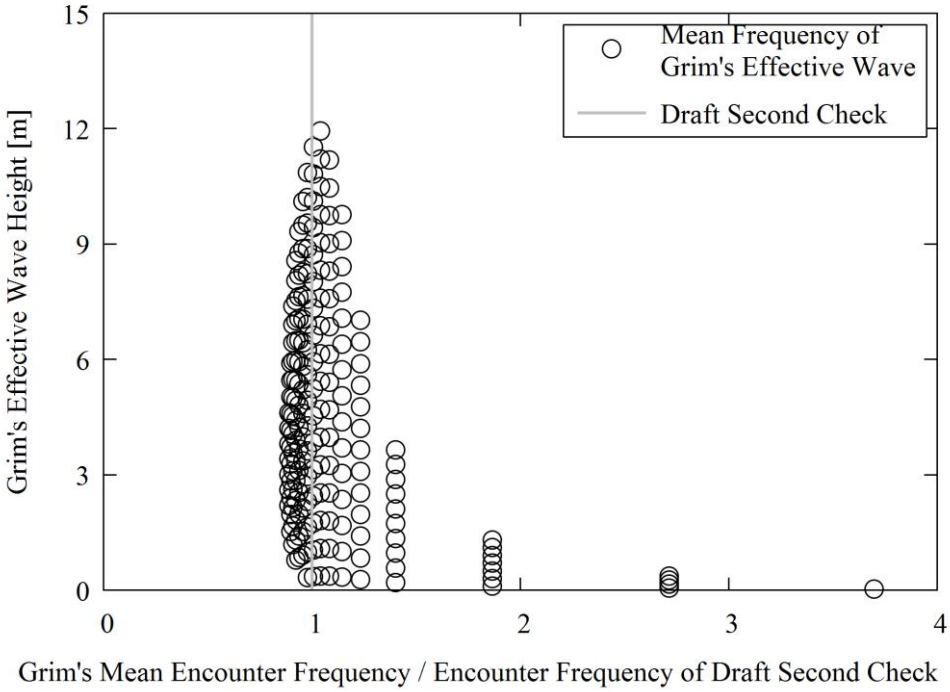

Figure 2.5.3.4 Relationship between the mean wave frequency and wave height of Grim's effective wave with service speed in heading waves.

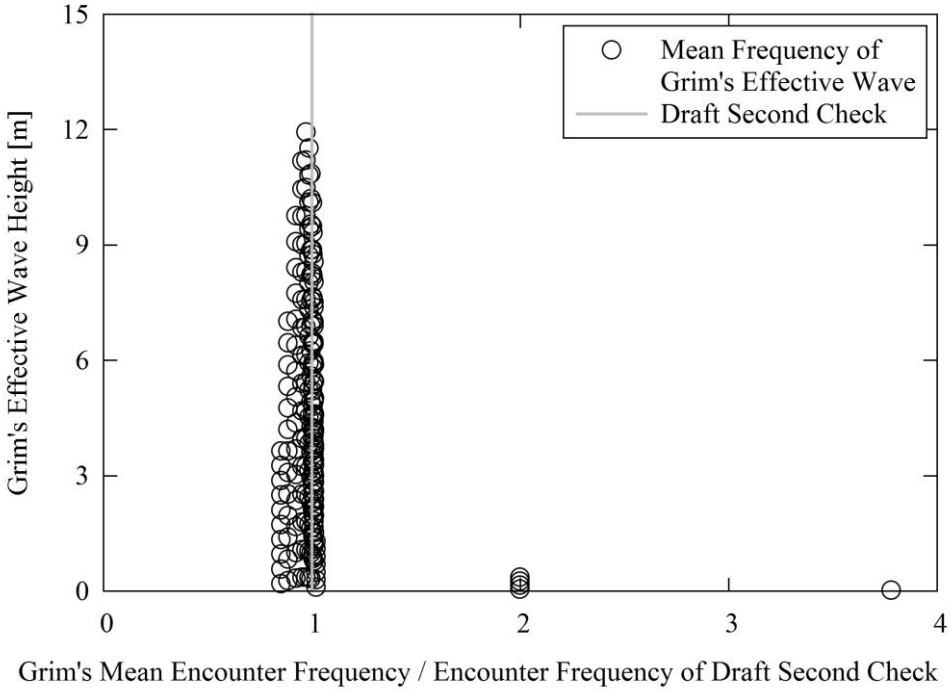

Figure 2.5.3.5 Relationship between the mean wave frequency and wave height of Grim's effective wave with service speed in following waves.

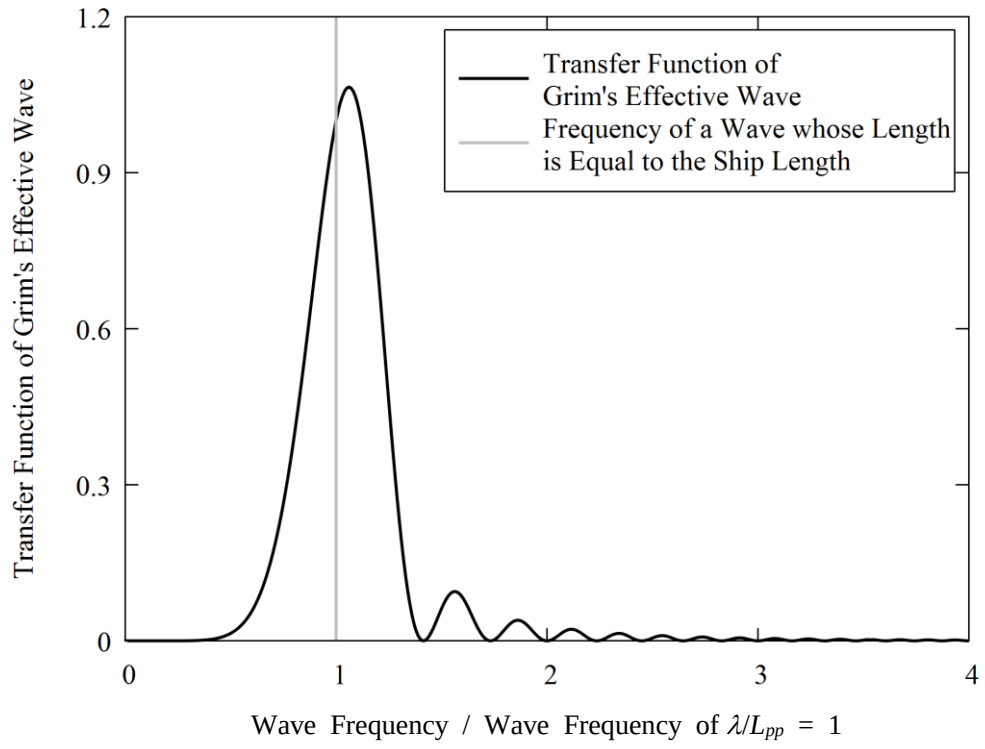

Figure 2.5.3.6 Transfer function of Grim's effective wave spectrum.

2.6 Conclusions

In this chapter, parametric roll is investigated by using an averaging method. The conclusions are:

1. Adding superharmonic components to the assumed form of solution in the averaging method improves the estimation accuracy;
2. Averaged equations is derived by using the actual GZ curve in calm water, and the effect of calm-water GZ on parametric roll response is revealed;
3. Taking account of linearly-estimated vertical motions resolves overestimation of the model experiment especially around low speed region;
4. The critical ship speed for parametric roll is estimated by using averaging method;
5. The wave encounter frequency used in the draft second check of the second generation intact stability criteria (IMO, 2015) is verified by using the mean encounter frequency of Grim's effective wave spectrum.

CHAPTER 3 LOW SPEED MODEL

3.1 Introduction

In chapter 2, a simplified 1-dof parametric roll model is used. To investigate more precise response of parametric roll, multi-degree-of-freedom models is proposed in this chapter. For example, Hamamoto and Akiyoshi (1988) proposed the 6-dof model based on Froude Krylov assumption and slender body theory, De Kat and Paulling (1989) took diffraction forces into account. They focused on not only parametric roll but also pure loss of stability and broaching-to, so that their models were not specialized ones to estimate parametric roll.

Since parametric roll is caused by the variation of restoring coefficients, estimation of the variation is essential to obtain accurate results. Boroday (1990) showed that the restoring variation could be estimated by adding added mass terms based on a strip theory to the Froude Krylov forces by comparing with a captive model experiment. From this point of view, Hashimoto and Umeda (2010) proposed a heave-roll-pitch coupled 3-dof to estimate parametric roll in longitudinal waves. The 3-dof model took radiation and diffraction effects as a function of an instantaneous heel angle into account. The results showed good agreement with towing model experiments.

However, a ship encounters waves from various directions in actual seas, so that coupling with sway and yaw motions should not be neglected. Thus, parametric roll in oblique waves have to be investigated. Based on the well validated 3-dof model (Hashimoto & Umeda, 2010), a sway-heave-roll-pitch-yaw coupled 5-dof model is proposed in this chapter. For oblique waves, validation efforts for existing numerical models (Sanchez & Nayfeh, 1990b; Neves & Valerio, 2000) have not been sufficient so far, partly because a model experiment requires a seakeeping and manoeuvring basin and partly because coupling with manoeuvring motion including rudder actions are unavoidable. Further, the C11-class post-Panamax container ship suffered parametric roll under heave-to condition (France et al., 2003), so that manoeuvring with low speed should be considered.

Based on these understandings, in this study, the 5-dof model is proposed based on a low-speed manoeuvring model in oblique waves and is validated with newly executed model experiment in the seakeeping and manoeuvring basin of National Research Institute of Fisheries Engineering (NRIFE). The comparison between the 5-dof model and experiment in regular oblique waves is performed in section 3.5, while validation with experiment in irregular oblique waves will be a subject of future work.

3.2 Mathematical Model

The coordinate systems are shown in Fig. 3.2.1. The space-fixed coordinate system is denoted by O_1-$\xi\eta\zeta$, the coordinate system moving with a constant speed of U and course of χ is denoted by O_2-XYZ and the body-fixed coordinate system is denoted by G-xyz. Here, we assume that a wave propagates in the direction of the $O_1\xi$ axis and the ship oscillates around O_2-XYZ. The point G indicates the centre of ship mass and O_1G_0 indicates the initial depth of the centre of ship mass. The ship's motions around O_2-XYZ are denoted by x_i: surge (i = 1), sway (i = 2), heave (i = 3), roll (i = 4),

pitch (i = 5) and yaw (i = 6). The coupled sway-heave-roll-pitch-yaw motions are modelled as Eq. 3.2.1:

$$\begin{cases} m\ddot{x}_2 = F_2(x_2, x_3, x_4, x_5, x_6, \dot{x}_2, \dot{x}_3, \dot{x}_4, \dot{x}_5, \dot{x}_6, \ddot{x}_2, \ddot{x}_3, \ddot{x}_4, \ddot{x}_5, \ddot{x}_6, t) \\ m\ddot{x}_3 = F_3(x_2, x_3, x_4, x_5, x_6, \dot{x}_2, \dot{x}_3, \dot{x}_4, \dot{x}_5, \dot{x}_6, \ddot{x}_2, \ddot{x}_3, \ddot{x}_4, \ddot{x}_5, \ddot{x}_6, t) \\ I_{xx}\ddot{x}_4 = F_4(x_2, x_3, x_4, x_5, x_6, \dot{x}_2, \dot{x}_3, \dot{x}_4, \dot{x}_5, \dot{x}_6, \ddot{x}_2, \ddot{x}_3, \ddot{x}_4, \ddot{x}_5, \ddot{x}_6, t) \\ I_{yy}\ddot{x}_5 = F_5(x_2, x_3, x_4, x_5, x_6, \dot{x}_2, \dot{x}_3, \dot{x}_4, \dot{x}_5, \dot{x}_6, \ddot{x}_2, \ddot{x}_3, \ddot{x}_4, \ddot{x}_5, \ddot{x}_6, t) \\ I_{zz}\ddot{x}_6 = F_6(x_2, x_3, x_4, x_5, x_6, \dot{x}_2, \dot{x}_3, \dot{x}_4, \dot{x}_5, \dot{x}_6, \ddot{x}_2, \ddot{x}_3, \ddot{x}_4, \ddot{x}_5, \ddot{x}_6, t) \end{cases}, \quad (3.2.1)$$

where m: ship mass, I_{xx}: moment of inertia of ship mass in roll, I_{yy}: moment of inertia of ship mass in pitch, I_{zz}: moment of inertia of ship mass in yaw, t: time and F_j: force or moment in the j direction. A dot denotes differentiation with time. Here, to avoid the estimation of added resistance due to waves, we assume that the surge motion x_1 is zero, i.e. the ship runs with a constant velocity U. The forces are modelled according to

$$F_j = F_j^{\,B} + F_j^{\,FK} + F_j^{\,EG} + F_j^{\,R} + F_j^{\,D} + F_j^{\,MLS} + F_j^{\,DEL}, \quad (3.2.2)$$

where the superscript B indicates the component due to hydrostatic pressure, FK the component due to incident wave pressure, EG the component due to gravity, R the radiation component, D the diffraction component, MLS the hull force due to manoeuvring motion and DEL the force due to rudder action.

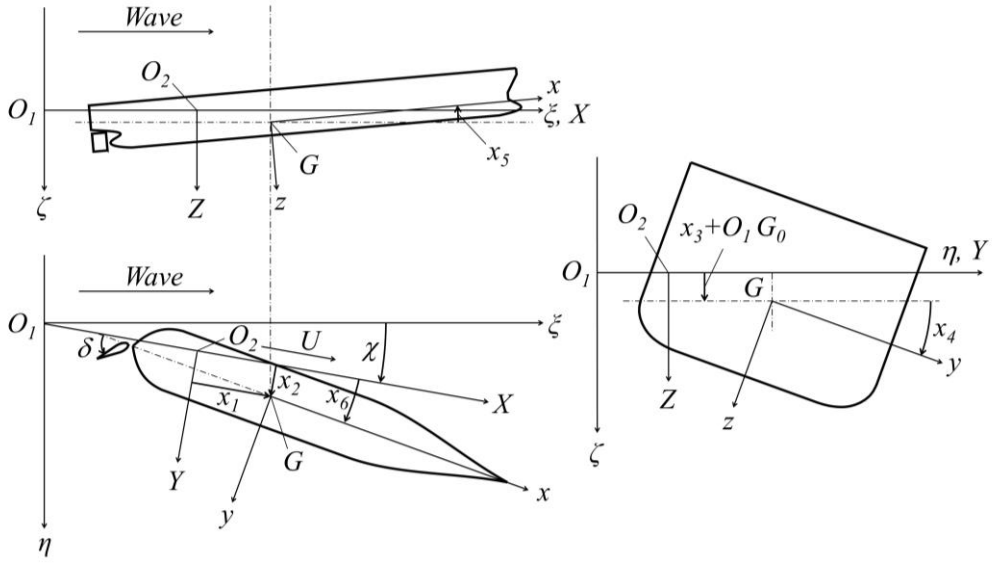

Figure 3.2.1 Coordinate systems

3.3 Modeling of External Forces

The external forces are divided into the seven components, which are explained following subsections, as Eq. 3.2.2. The buoyancy, Froude-Krylov, and gravitational forces are shown in subsection 3.3.1. The radiation and diffraction forces are shown in subsection 3.3.2 based on a

seakeeping theory. However, since the roll damping moment is dominated by the viscous effect, the roll damping and inertia coefficients are estimated by roll decay test as shown in subsection 3.3.3. The manoeuvring hull and rudder forces are shown in subsection 3.3.4.

3.3.1 Buoyancy and Froude Krylov Forces

Assuming that the incident waves are sinusoidal, their elevation, ζ_w, and wave pressure, p, are given by

$$\zeta_w = \zeta_a \cos\left(\frac{\omega_k^{\,2}}{g}\xi - \omega_k t\right), \tag{3.3.1.1}$$

$$p = \rho g \zeta_a \exp\left(-\frac{\omega_k^{\,2}}{g}(\zeta - \zeta_w)\right)\cos\left(\frac{\omega_k^{\,2}}{g}\xi - \omega_k t\right), \tag{3.3.1.2}$$

where ρ: water density, ζ_a: wave amplitude, g: gravitational acceleration, ω_k: wave circular frequency and t: time. Here, water pressure is adjusted to be zero at the wave surface, although this is a higher-order correction under the assumption of small wave steepness.

The sectional submerged hull contour, S_H, can then be determined by

$$S_H = S_H(\zeta_w, x_1, x_2, x_3, x_4, x_5, x_6; x). \tag{3.3.1.3}$$

By integrating the water pressure on the sectional submerged hull contour, the buoyancy, F_j^B, and Froude Krylov forces, F_j^{FK}, can be calculated as Eq. 3.3.1.4 and 3.3.1.5:

$$F_j^B = \rho g \int_L dx \int_{S_H} -\zeta n_j ds, \tag{3.3.1.4}$$

$$F_j^{FK} = -\int_L \int_{S_H} p n_j ds dx, \tag{3.3.1.5}$$

where L indicates the range of the hull in the x direction and n_j is the vector normal to the hull surface. The gravitational force, F_3^{EG}, in the vertical direction is given by

$$F_3^{EG} = mg. \tag{3.3.1.6}$$

3.3.2 Radiation and Diffraction Forces

When parametric roll occurs, the frequency of roll is definitely smaller than the wave encounter frequency. Thus the hydrodynamic coefficients could depend on not only the frequency but also the instantaneous roll angle. Thus, the radiation and diffraction coefficients are calculated at each roll angle based on the strip theory. The radiation force, F_i^R, can be calculated as Eq. 3.3.2.1:

$$F_i^R = \sum_{j=2}^{6}\left[-A_{ij}(x_4)\ddot{x}_j - B_{ij}(x_4)\dot{x}_j - C_{ij}(x_4)x_j\right], \tag{3.3.2.1}$$

where A_{ij}, B_{ij} and C_{ij} are the added mass, wave damping coefficient and restoring coefficient, respectively. If the ship motions are harmonic, the terms in C_{ij} in analytical formulae for determining

the ship motions are equivalent to the terms in A_{ij} divided by ω_e^2. If we do not replace the parts of A_{ij} with C_{ij}, we could face difficulty in accurate calculation when ω_e^2 tends to zero. Actually, Lee and Kim (1982) did not use the C_{ij} to estimate motion of a ship who had an asymmetric submerged hull. This was because they considered a damaged ship, so that the encounter frequency was not so small. By extending the equations without coupling between vertical and horizontal motions (Takaishi & Kuroi, 1977) to those with coupling, the following equations are obtained:

$$A_{22}=\int_L A_{H22}dx,\ A_{23}=\int_L A_{H23}dx,\ A_{24}=\int_L A_{H24}dx,\ A_{25}=-\int_L xA_{H23}dx,$$
$$A_{26}=\int_L xA_{H22}dx,\ A_{32}=\int_L A_{H32}dx,\ A_{33}=\int_L A_{H33}dx,\ A_{34}=\int_L A_{H34}dx,$$
$$A_{35}=-\int_L xA_{H33}dx,\ A_{36}=\int_L xA_{H32}dx,\ A_{42}=\int_L A_{H42}dx,$$
$$A_{43}=\int_L A_{H43}dx,\ A_{45}=-\int_L xA_{H43}dx,\ A_{46}=\int_L xA_{H42}dx,$$
$$A_{52}=-\int_L xA_{H32}dx,\ A_{53}=-\int_L xA_{H33}dx,\ A_{54}=-\int_L xA_{H34}dx,$$
$$A_{55}=\int_L x^2A_{H33}dx,\ A_{56}=-\int_L x^2A_{H32}dx,\ A_{62}=\int_L xA_{H22}dx,$$
$$A_{63}=\int_L xA_{H23}dx,\ A_{64}=\int_L xA_{H24}dx,\ A_{65}=-\int_L x^2A_{H23}dx,$$
$$A_{66}=\int_L x^2A_{H22}dx, \qquad (3.3.2.2)$$

$$B_{22}=\int_L B_{H22}dx-U\left[A_{H22}\right]_{x_a}^{x_f},\ B_{23}=\int_L B_{H23}dx-U\left[A_{H23}\right]_{x_a}^{x_f},$$
$$B_{24}=\int_L B_{H24}dx-U\left[A_{H24}\right]_{x_a}^{x_f},$$
$$B_{25}=-\int_L xB_{H23}dx+U\int_L A_{H23}dx+U\left[xA_{H23}\right]_{x_a}^{x_f},$$
$$B_{26}=\int_L xB_{H22}dx-U\int_L A_{H22}dx+U\left[xA_{H22}\right]_{x_a}^{x_f},$$
$$B_{32}=\int_L B_{H32}dx-U\left[A_{H32}\right]_{x_a}^{x_f},\ B_{33}=\int_L B_{H33}dx-U\left[A_{H33}\right]_{x_a}^{x_f},$$
$$B_{34}=\int_L B_{H34}dx-U\left[A_{H34}\right]_{x_a}^{x_f},$$
$$B_{35}=-\int_L xB_{H33}dx+U\int_L A_{H33}dx+U\left[xA_{H33}\right]_{x_a}^{x_f},$$
$$B_{36}=\int_L xB_{H32}dx-U\int_L A_{H32}dx-U\left[xA_{H32}\right]_{x_a}^{x_f},$$
$$B_{42}=\int_L B_{H42}dx-U\left[A_{H42}\right]_{x_a}^{x_f},\ B_{43}=\int_L B_{H43}dx-U\left[A_{H43}\right]_{x_a}^{x_f},$$
$$B_{45}=-\int_L xB_{H43}dx+U\int_L A_{H43}dx+U\left[xA_{H43}\right]_{x_a}^{x_f},$$
$$B_{46}=\int_L xB_{H42}dx-U\int_L A_{H42}dx-U\left[xA_{H42}\right]_{x_a}^{x_f},$$
$$B_{52}=-\int_L xB_{H32}dx-U\int_L A_{H32}dx+U\left[xA_{H32}\right]_{x_a}^{x_f},$$
$$B_{53}=-\int_L xB_{H33}dx-U\int_L A_{H33}dx+U\left[xA_{H33}\right]_{x_a}^{x_f},$$
$$B_{54}=-\int_L xB_{H34}dx-U\int_L A_{H34}dx-U\left[xA_{H34}\right]_{x_a}^{x_f},$$
$$B_{55}=\int_L x^2B_{H33}dx-U\left[x^2A_{H33}\right]_{x_a}^{x_f},$$

$$B_{56} = -\int_L x^2 B_{H32} dx + U\int_L x A_{H32} dx + U\left[x^2 A_{H32}\right]_{x_a}^{x_f},$$
$$B_{62} = \int_L x B_{H22} dx - U\int_L A_{H22} dx - U\left[x A_{H22}\right]_{x_a}^{x_f},$$
$$B_{63} = \int_L x B_{H23} dx + U\int_L A_{H23} dx - U\left[x A_{H23}\right]_{x_a}^{x_f},$$
$$B_{64} = \int_L x B_{H24} dx + U\int_L A_{H24} dx - U\left[x A_{H24}\right]_{x_a}^{x_f},$$
$$B_{65} = -\int_L x^2 B_{H23} dx + U\left[x^2 A_{H23}\right]_{x_a}^{x_f},\quad B_{66} = \int_L x^2 B_{H22} dx - U\left[x^2 A_{H22}\right]_{x_a}^{x_f}, \tag{3.3.2.3}$$

$$C_{25} = U\int_L B_{H23} dx - U^2\left[A_{H23}\right]_{x_a}^{x_f},\quad C_{26} = -U\int_L B_{H22} dx + U^2\left[A_{H22}\right]_{x_a}^{x_f},$$
$$C_{35} = U\int_L B_{H33} dx - U^2\left[A_{H33}\right]_{x_a}^{x_f},\quad C_{36} = -U\int_L B_{H32} dx + U^2\left[A_{H32}\right]_{x_a}^{x_f},$$
$$C_{45} = U\int_L B_{H43} dx - U^2\left[A_{H43}\right]_{x_a}^{x_f},\quad C_{46} = -U\int_L B_{H24} dx + U^2\left[A_{H24}\right]_{x_a}^{x_f},$$
$$C_{55} = -U\int_L x B_{H33} dx - U^2\int_L A_{H33} dx + U^2\left[x A_{H33}\right]_{x_a}^{x_f},$$
$$C_{66} = -U\int_L x B_{H22} dx - U^2\int_L A_{H22} dx + U^2\left[x A_{H22}\right]_{x_a}^{x_f}, \tag{3.3.2.4}$$

where

$$A_{Hij} - i\frac{B_{Hij}}{\omega} = -\rho\int_{S_H} \phi_j n_i ds. \tag{3.3.2.5}$$

Here, ϕ_j is the velocity potential of the two-dimensional flow under hull and linear free surface conditions. These coefficients are calculated as ω is ω_ϕ for j = 2, 4 and 6 and as ω_e is ω_e for j = 3 and 5 This is because upon the occurrence of parametric roll, the frequency of lateral motion is approximately ω_ϕ rather than ω_e. The added mass and damping in roll are estimated by using roll decay test as shown in subsection 3.3.3 because the viscous effect is dominant in roll motion. The diffraction force, F_j^D, can be calculated as Eq. 3.3.2-5 (Salvesen et al., 1970):

$$F_j^D = \zeta_a F_{kj}^D\left(x_4\right)\cos\left(-\omega_e t - \varepsilon_{kj}^D\left(x_4\right)\right), \tag{3.3.2.6}$$

where

$$F_{kj}^D = \left|E_{kj}^D\right|, \tag{3.3.2.7}$$

$$\varepsilon_{kj}^D = \arg E_{kj}^D, \tag{3.3.2.8}$$

$$E_{kj}^{\ D} = \frac{\rho g \zeta_a}{i\omega}\int_L dx\int_{S_H} (i\omega_k - U\frac{\partial}{\partial x})\phi_D n_j ds, \tag{3.3.2.9}$$

$$\omega_e = \omega_k - \frac{\omega_k^2}{g} U\cos\chi. \tag{3.3.2.10}$$

Here, ϕ_D is the diffraction potential of two-dimensional flow under the hull and linear free surface conditions in incident waves. All the above radiation and diffraction forces are calculated for the hull

with the instantaneous heel angle at every time step of the numerical simulation in time domain.

3.3.3 Estimation of Roll Damping

The roll damping coefficients and inertia are estimated as Eq. 3.3.3.1 and 3.3.3.2:

$$I_{xx} + A_{44} = W \cdot GM \left(\frac{T_\phi + T_{corr}}{2\pi} \right)^2, \tag{3.3.3.1}$$

$$B_{44}\dot{x}_4 = \alpha \dot{x}_4 + \gamma \dot{x}_4^{\,3}, \tag{3.3.3.2}$$

where T_{corr} is the correction factor of the roll inertia due to the nonlinearity of the added inertia. A roll decay test without advance speed is conducted to obtain the roll damping coefficient and roll inertia for the 5-dof numerical simulation.

3.3.4 Manoeuvring Hull and Rudder Forces

Since parametric roll occurs at low speeds, it is desirable to estimate manoeuvring forces with a mathematical model suitable for a situation where the ship's forward velocity is comparable to its lateral velocity (Umeda & Yamakoshi, 1989). The hull manoeuvring force, F_i^{MLS}, can be estimated as the sum of linear lift components Y_L and N_L and non-linear cross-flow drag components Y_C and N_C:

$$F_2^{MLS} = Y_C + Y_L, \tag{3.3.4.1}$$

$$F_6^{MLS} = N_C + N_L, \tag{3.3.4.2}$$

where

$$Y_C = \frac{1}{2}\rho \int_{-L/2}^{L/2} d \cdot C_D \left| v + rx \right| \left(v + rx \right) dx, \tag{3.3.4.3}$$

$$N_C = \frac{1}{2}\rho \int_{-L/2}^{L/2} d \cdot C_D \left| v + rx \right| \left(v + rx \right) x dx, \tag{3.3.4.4}$$

$$Y_L = Y_v v + Y_r r, \tag{3.3.4.5}$$

$$N_L = N_v v + N_r r, \tag{3.3.4.6}$$

$$u = U\cos x_6 + \dot{x}_2 \sin x_6, \quad v = -U\sin x_6 + \dot{x}_2 \cos x_6, \quad r = \dot{x}_6, \tag{3.3.4.7}$$

$$Y_v = \left(\frac{1}{2}\rho L_{pp} d \cdot u \right) \cdot Y_v', \tag{3.3.4.8}$$

$$N_v = \left(\frac{1}{2}\rho L_{pp}^{\,2} d \cdot u \right) \cdot N_v', \tag{3.3.4.9}$$

$$Y_r = \left(\frac{1}{2} \rho L_{pp}{}^2 d \cdot u \right) \cdot Y_r', \tag{3.3.4.10}$$

$$N_r = \left(\frac{1}{2} \rho L_{pp}{}^3 d \cdot u \right) \cdot N_r'. \tag{3.3.4.11}$$

Here, d is the mean draft of the ship, and u and v are the surge and sway velocity defined in the body-fixed coordinate system G-xyz, respectively. C_D is the cross-flow drag coefficient when the ship is laterally towed.

The rudder-induced force, F_i^{DEL}, is calculated as Eq. 3.3.4.12 and 3.3.4.13:

$$F_2^{DEL} = -(1+a_H)\frac{1}{2}\rho A_R u_R{}^2 f_\alpha \delta, \tag{3.3.4.12}$$

$$F_6^{DEL} = -(x_R + a_H x_H)\frac{1}{2}\rho A_R u_R{}^2 f_\alpha \delta, \tag{3.3.4.13}$$

where

$$\delta = -K_P x_6, \tag{3.3.4.14}$$

$$u_R = \varepsilon_w u_p \sqrt{1+\frac{8K_T}{\pi J^2}}, \tag{3.3.4.15}$$

$$u_p = (1-w_p)U \tag{3.3.4.16}$$

$$J = \frac{u_p}{n_p D_p}, \tag{3.3.4.17}$$

$$K_T = aJ^2 + bJ + c, \tag{3.3.4.18}$$

Here, δ: rudder angle, a_H: the interaction factor for rudder force between hull and rudder, x_H: the longitudinal position of rudder force due to interaction between hull and rudder, x_R: the longitudinal rudder position, A_R: the rudder area, f_α: the hydrodynamic rudder lift slope, K_P: the rudder gain, u_p: the propeller inflow velocity, u_R: the rudder inflow velocity, n_p: the propeller revolution number, D_P: the propeller diameter, K_T: the thrust coefficient, and ε_w: the wake fraction ratio between propeller and rudder positions. From Eq. 3.3.4.15 and 3.3.4.17-18, the rudder inflow velocity can be rewritten as Eq. 3.3.4.19:

$$\begin{aligned} u_R &= \varepsilon_w u_p \sqrt{1+\frac{8}{\pi}\left(a+\frac{b}{J}+\frac{c}{J^2}\right)} \\ &= \varepsilon_w u_p \sqrt{1+\frac{8}{\pi}\left(a+\frac{b n_p D_p}{u_p}+\frac{c n_p{}^2 D_p{}^2}{u_p{}^2}\right)} \end{aligned}$$

$$= \varepsilon_w \sqrt{u_p{}^2 + \frac{8}{\pi}\left(a u_p{}^2 + b n_p D_p u_p + c n_p{}^2 D_p{}^2\right)}. \qquad (3.3.4.19)$$

The flow straightening effect is ignored because captive model experiment related to rudder forces has not been conducted for a subject ship shown in section 3.4.

3.4 Model Experiment

To validate the numerical model for parametric roll in oblique waves, experiments using a 1/48.8 scaled model of the 154 m-long ONR flare topside vessel were performed at the seakeeping and manoeuvring basin of the NRIFE. The technique of free running model experiment is shown in appendix subject ships. The principal particulars and body plan of the vessel are presented also in appendix subject ships.

The coefficients of roll damping and inertia are shown in Tab. 3.4.1. The comparison of roll decay between experiment and numerical simulation by the 5-dof model is shown in Fig. 3.4.1. The chain line indicate the roll decay in the model experiment. The time series of roll decay shows good agreement when the roll amplitude is relatively large.

The system parameters for manoeuvring forces, such as C_D and Y_v, can be estimated by captive model experiment of a ship. In this study, the coefficients measured in the circular motion tests of a C11-class post-Panamax container ship, whose hull form is similar to the ONR flare topside vessel, are used. Linear coefficients could be estimated by using the ship aspect ratio k, the block coefficient C_b and L_{pp}/B (Yoshimura et al., 2009). The cross-flow drag coefficient C_D is strongly dependent on L_{pp}/d (Yoshimura et al., 2009). As shown in Tab. 3.4.2, the differences between these parameters for the ONR flare topside vessel and C11 class post Panamax container ship are not large. The values of hydrodynamic coefficients for roll manoeuvring forces are shown in Tab. 3.4.3 (Kubo, 2012).

The free running experiment was performed for regular stern quartering waves. The wavelength to ship length ratio was 1.25 and the wave steepness was 0.03. As shown in Fig. 3.4.2, under these wave conditions, the GZ curve of the ONR flare topside vessel clearly changes due to the longitudinal waves. The auto pilot course ranged from 0° in the wave direction to –70° but no parametric roll occurred for the auto pilot course of –70°. The propeller rotated at 143 rpm in the model scale, which corresponds to *Fn* of 0.05 in calm water.

Table 3.4.1 Experimentally estimated roll damping coefficient of the ONR flare topside vessel in full scale.

Item	ONR flare topside vessel	unit
Natural roll period: T_ϕ	21.32	s
Correction factor of roll inertia: T_{corr}	1.0	s
Linear damping: α	2.509×10^{-2}	s^{-1}
Cubic damping: γ	10.39	s

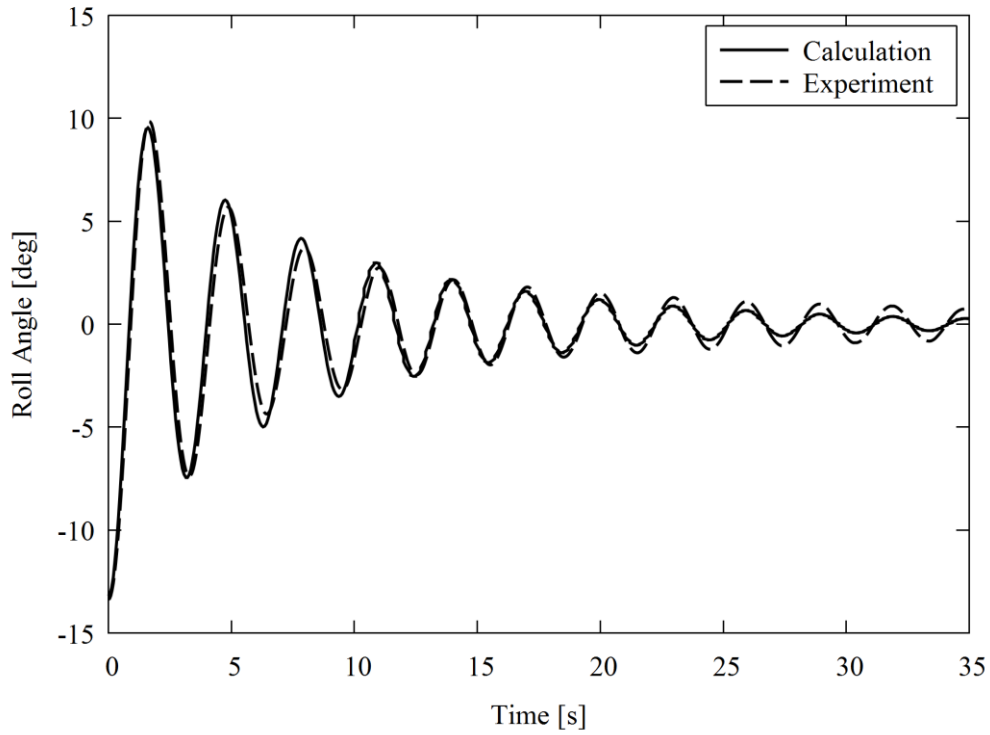

Figure 3.4.1 Comprison of roll decay of the ONR flare topside vessel in model scale.

Table 3.4.2 Comparison of the geometrical parameters for the ONR flare topside vessel and C11-class post-Panamax container ship.

Item	C11-class post-Panamax container ship	ONR flare topside vessel
k	0.0374	0.0439
C_b	0.536	0.559
L_{pp}/B	7.84	6.55
L_{pp}/d	26.8	22.8

Table 3.4.3 Experimentally estimated manoeuvring coefficients of the C11-class post-Panamax container ship.

Item	C11-class post-Panamax container ship	unit
Y_v'	−0.207	
Y_r'	0.0419	
N_v'	−0.110	
N_r'	−0.0238	
C_D	0.788	
a_H	0.25	
x_H	-66.2	m
x_R	-71.49	m
A_R	28.64	m^2
f_α	2.521	
ε_w	1.0	
1-w_P	1.0	
D_P	4.97	m
$K_T(J)$	0.6336 -0.2693 J -0.09617 J^2	

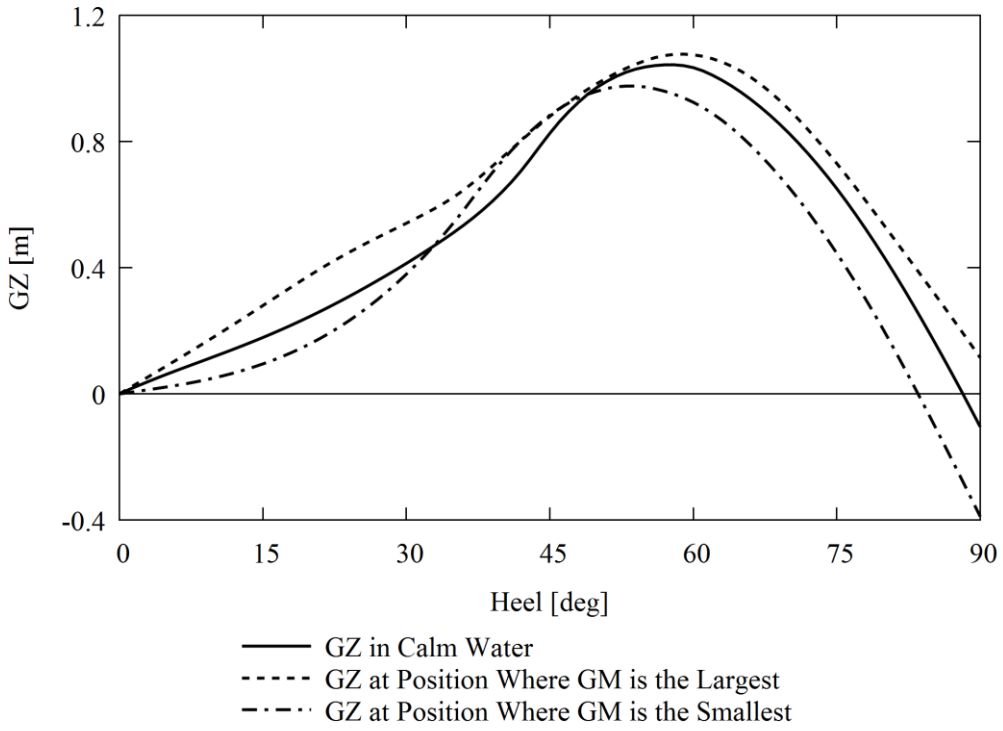

Figure 3.4-2 GZ variations of the ONR flare topside vessel in longitudinal waves with wavelength to ship length ratio of 1.25 and wave steepness of 0.03 in full scale.

3.5 Validation

The comparison between the numerical and experimental results for the steady amplitude for each condition is shown in Fig. 3.5.1. The numerical calculations are performed under the following conditions: the Froude number is 0.0365, which is the mean value of the ship speed observed in the free running experiments. The time series results of roll, pitch and heading angle with the auto pilot course of −30° of the experiment and calculation are shown in Fig. 3.5.2 and 3.5.3, respectively. In these figures, the roll period is twice the pitch period, which is equal to the wave encounter period, and the roll period is nearly equal to the ship natural roll period. Thus, this can be characterized as a typical parametric roll. The discrepancy between the auto pilot course and the heading angle in the experiment suggests the possible existence of a wave drift yaw moment.

As shown in Fig. 3.5.1, both in experiment and calculation, the largest roll amplitude occurs at the ship heading different from the wave direction. However, when the heading angle increases further, the roll amplitude decreases. This is because of the shift of encounter frequency together with the reduction in the roll restoring variation. Comparison of Fig. 3.5.2 and 3.5.3 shows that there are discrepancies between the experimental and calculated results. One reason for this is that the heading angles that determine the amplitude of restoring variation are not estimated well. Here, the 'heading angle' means the mean value of the sum of χ and x_6. Therefore, the parametric roll amplitudes are plotted as a function of the heading angle in Fig. 3.5.4. The results indicate a better agreement between the experiment and calculation than that the results in Fig. 3.5.1 do. However, the calculated values still overestimate the measured values.

The overestimation of the experimental values observed in Fig. 3.5.4 reveals that the difference in the heading angle is just one of the reasons for the overestimation of the parametric roll amplitudes. As shown in Fig. 3.5.5, ξ-η motions in experiment and calculation are then compared in order to find the origin of the discrepancy between the experimental and calculated roll values. The horizontal and vertical axes in Fig. 3.5.5 represent the longitudinal and lateral directions of the model basin, respectively, if the real scale length is used. The incident waves propagate from left to right. The trajectory in calculation is shifted in the direction opposite to wave propagation. This discrepancy could result in the inaccuracy of the calculated roll moment coupled with sway motion. There may be several reasons why the sway motion is not estimated well, with wave drift force and numerical drift being the most probable ones. Therefore, the wave drift force, which acts in the direction of wave propagation, is not considered in our model. However, since there is no restoring force in the sway direction, numerically obtained sway motion can occasionally diverge even in regular waves. This is not based on the physics of the problem but is rather a purely numerical issue (Fukasawa, 1990). However, as shown in Fig. 3.5.5, in our model, the sway motion does not diverge because the manoeuvring force is taken into account.

To further investigate this issue, numerical simulation using the measured surge, sway, and yaw motions is performed. The results with the auto pilot course of –30° are shown in Fig. 3.5.6. Here, the initial values used in the simulation are set to be the measured values. The agreement in the roll amplitude with the experimental results is slightly better than those obtained by the 5-dof simulation, while the pitch motion is in good agreement with the experimental result. This means that while an

improvement of the prediction accuracy of sway and yaw motions in waves under parametric roll conditions will enable a more accurate estimation of parametric roll, the amplitude will still be larger than experimental results. Resolving this issue could be one of the future tasks.

In addition to comparisons on time history, the Fourier series expansions of the time series of the roll in the numerical and experimental results in order to identify the dominant harmonics of roll motion as shown in Fig. 3.5.7. In the calculation, the amplitude at the frequency of half the wave encounter frequency is dominant and those at the other frequencies are negligibly small. The same conclusion can be applied also for the experiment but only with smaller auto pilot course. For larger auto pilot course, the harmonic element is dominant in the experiment. This could suggest that the experiment for large heading was not realised in steady condition assumed in the calculation. This could be a clue for the further study to validate a numerical model for oblique waves.

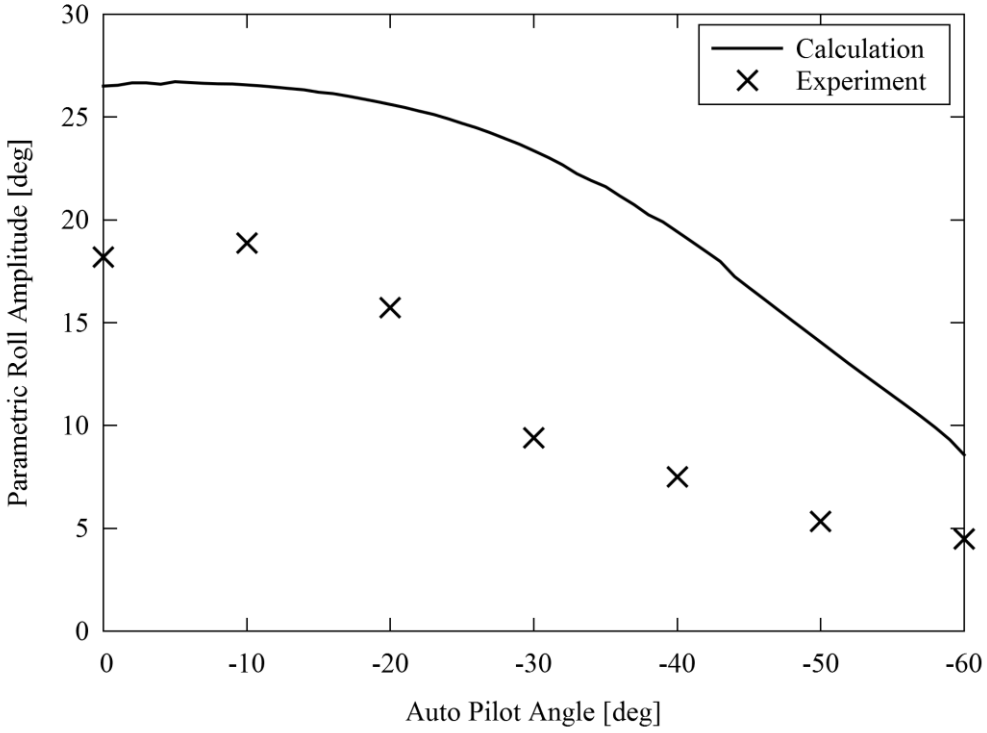

Figure 3.5.1 Steady amplitude of parametric roll in oblique waves as a function of auto pilot angle.

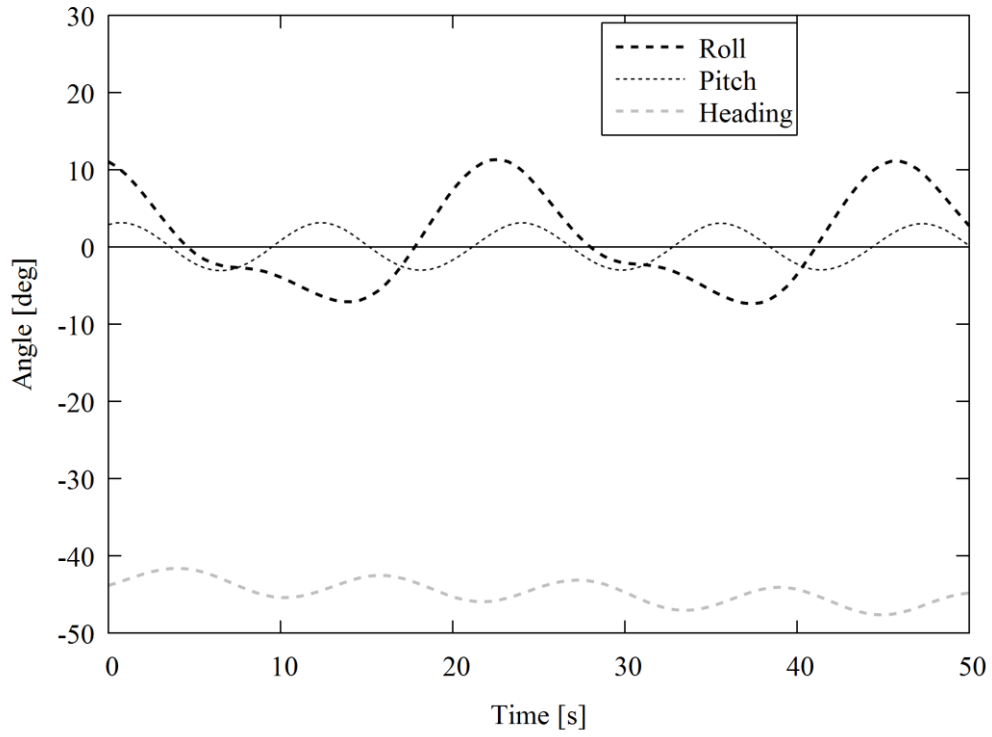

Figure 3.5.2 Time series of roll, pitch and heading angle in experiment with the auto pilot course of −30° in full scale.

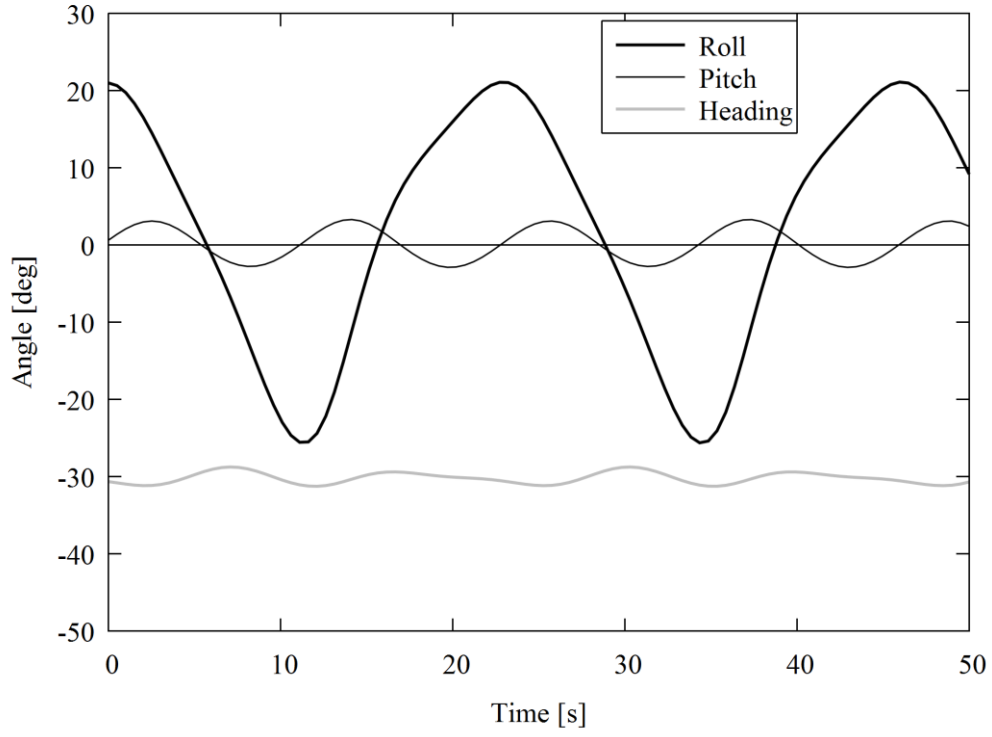

Figure 3.5.3 Time series of roll, pitch and heading angle in calculation with the auto pilot course of −30° in full scale.

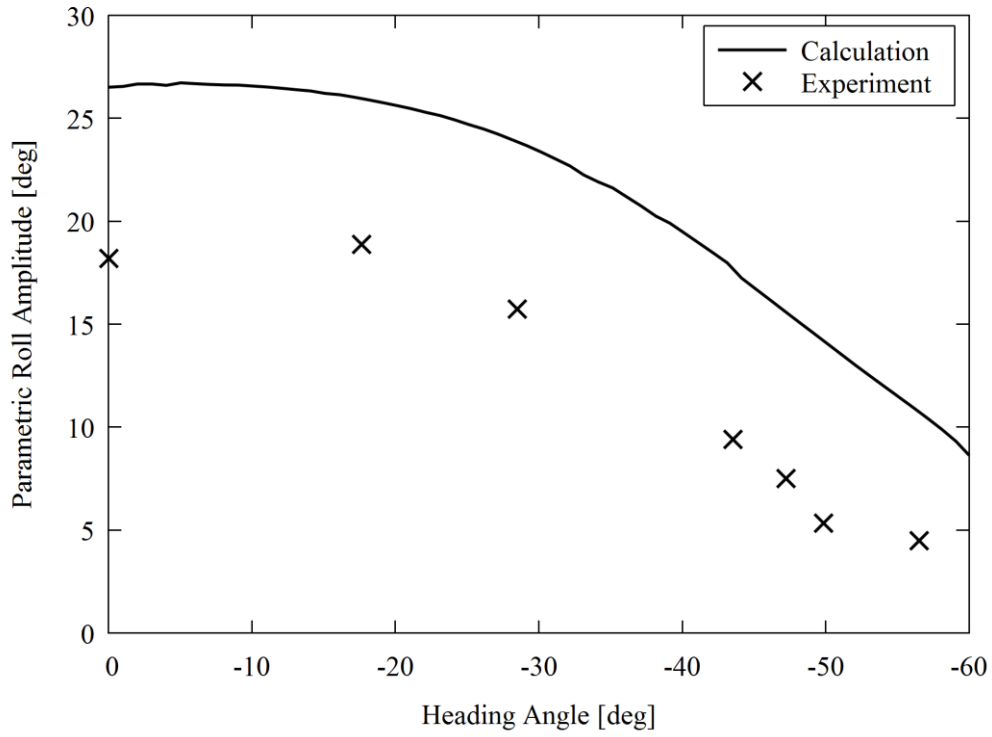

Figure 3.5.4 Steady amplitude of parametric roll in oblique waves as a function of heading angle.

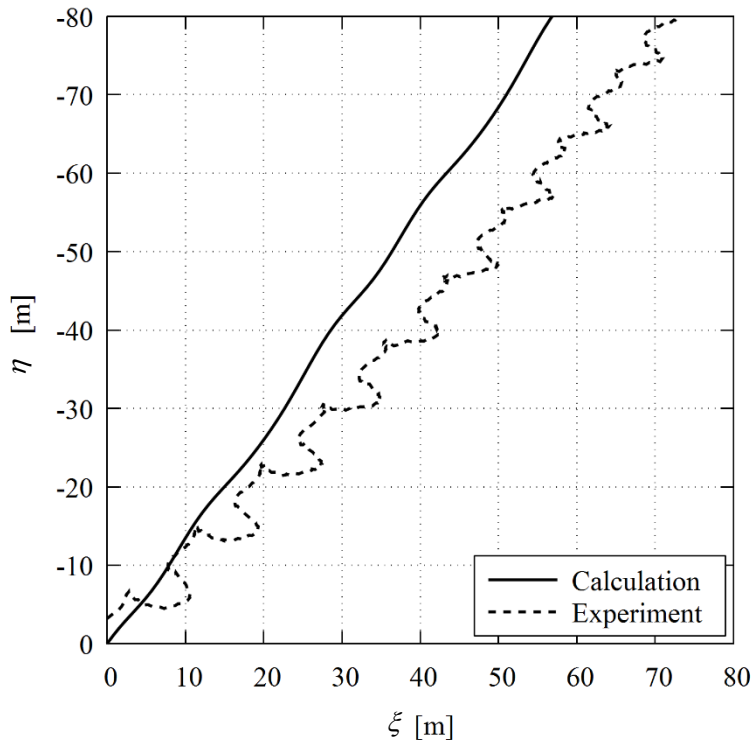

Figure 3.5.5 Ship trajectories with the auto pilot course of −30° in full scale.

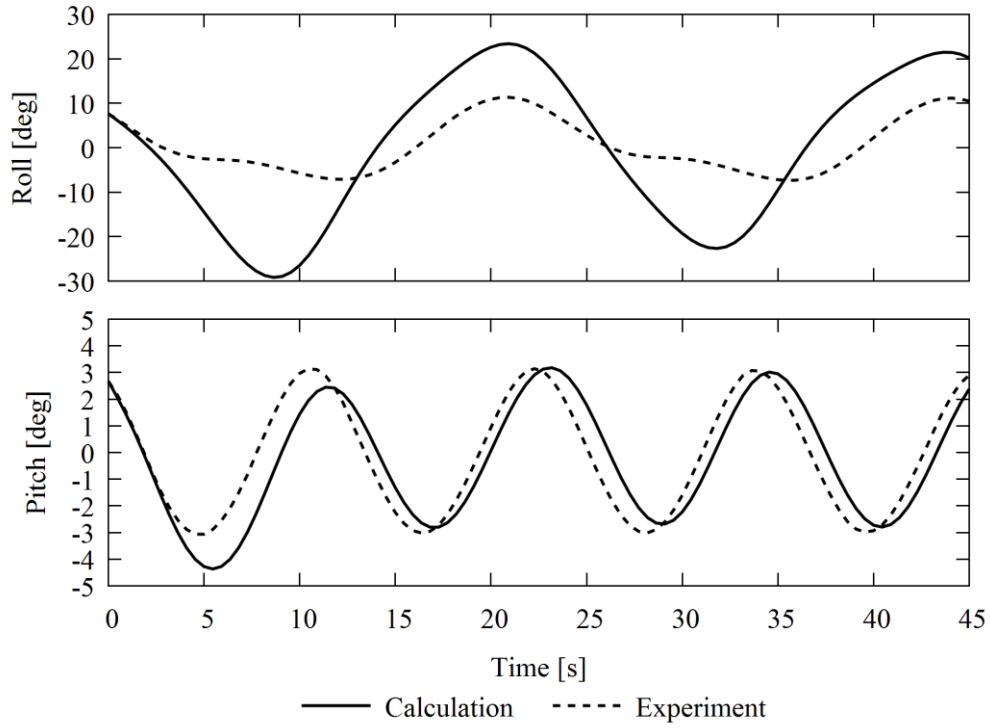

Figure 3.5.6 Roll and pitch motion comparisons in full scale.

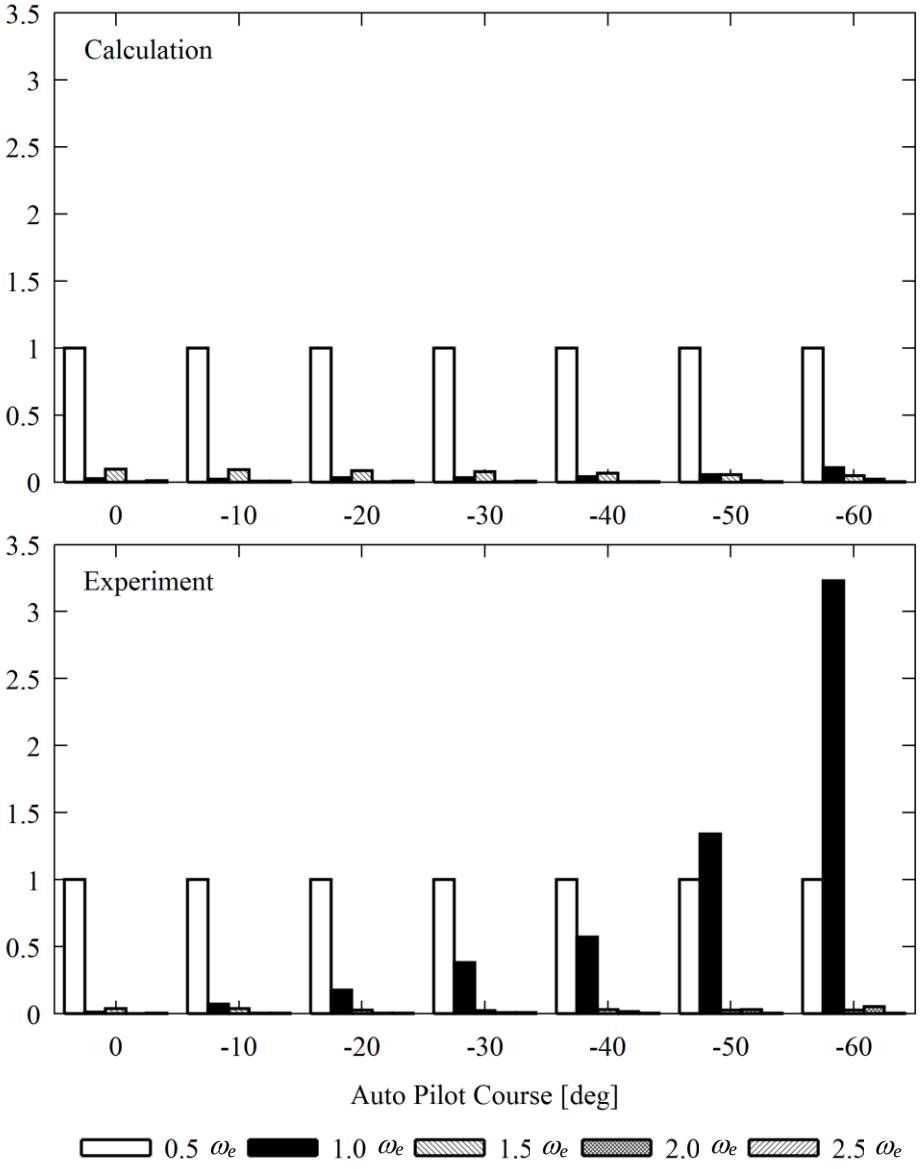

Figure 3.5.7 Roll amplitde components, which are normalized with that of the frequency of $0.5\omega_e$, for various frequencies as a result of the Fourier sries expansion of the time histories in the calculation and experiment.

3.6 Conclusions

Parametric roll in regular oblique waves was realized in free running model experiments of the ONR flare topside vessel, and its maximum amplitude was about 20°. The 5-dof numerical model captures some qualitative tendencies in the experiment but the estimated amplitudes are larger than the experiment by about seven degrees. The numerical model used here includes the nonlinear Froude Krylov components, radiation and diffraction components as functions of roll angle, and

manoeuvring forces. The roll amplitude decreases with increasing heading angle but the largest roll occurs for non-longitudinal waves in both experiment and calculation. Following this preliminary validation attempt, wider validation studies of parametric roll in oblique waves will be performed with different ships and different heading waves in the near future.

CHAPTER 4 EFFECT OF ENCOUNTER FREQUENCY

4.1 Introduction

Parametric roll is known as a ship roll motion that is excited by a periodic variation of coefficients of a roll restoring moment and occurs in an unstable region of the Mathieu equation. As for a ship roll motion in longitudinal waves, the unstable regions appear when a natural roll frequency, ω_ϕ, is almost equal to an integer multiple of half the encounter frequency, ω_e, hence $\omega_e:\omega_\phi \approx 2:n$. In this dissertation, parametric roll in the unstable region of $\omega_e:\omega_\phi \approx 2:n$ is called 2:*n* parametric roll. The widely-known parametric roll is expressed as 2:1 parametric roll in this rule.

There are few researches about the 2:2 parametric roll in the literature, so that our recognition about ship motion in this region is not enough from the view point of actual ship motion. Ogawara and Miura (1960) conducted captive model experiment and showed that 2:*n* parametric roll occurred in regular following waves. Sanchez and Nayfeh (1990a) closely investigated 2:1 and 2:2 parametric roll by using nonlinear dynamical approaches based on 1-dof roll model. Vilensky (1995) revealed that the 2:2 parametric roll is not so dangerous relative to the 2:1 parametric roll in purely following waves; however, the 2:2 parametric roll in stern quartering waves can cause a large roll motion due to the combination of the periodic GZ variation and direct exciting moment. Unfortunately, his study is not sufficiently accessible to the public. The 2:*n* parametric roll ($n > 2$), in other words, the higher advance speed region does not appear to have been investigated enough. Spyrou (2000) investigated the 2:1 and 2:2 parametric roll with different wave encounter frequencies by using the Mathieu-type nonlinear differential equation with a nonlinear roll damping. He defined very quick capsize events that occurred around a wave crest as a pure loss of stability. However, he mentioned that there was no practical reason to divide parametric roll and pure loss of stability. Moreover, Spyrou (2005) estimated that when *n* is greater than 2, 2:*n* parametric roll rarely happens mainly because the ship should run at high speed to achieve such a small encounter frequency and then the roll damping becomes too large to cause parametric roll. However, it is no more than a presumption based on the Mathieu-type equation.

In order to identify the 2:*n* parametric roll regions, the Mathieu-type 1-dof model for parametric roll, which is introduced in section 2.3, was used, and the 2:*n* parametric roll was of course confirmed. Then, actual ship roll motions in wide encounter frequency region were investigated with free running model experiments while increasing the ship advance speed. The 2:2 parametric roll was observed in the experiment; however, 2:3 and 2:4 parametric rolls were not observed as Spyrou (2005) presumed. Instead, a phenomenon which can be regarded as pure loss of stability was observed in the experiment with high ship advance speed. This indicates that the ship roll motion is not governed by the Mathieu-type equation when she runs with high speed in following waves. This might be because the coupling effect of surge motion is essential under such a condition. To explain experimentally observed roll motion, the nonlinear Mathieu equation proposed by Umeda et al. (2004) and a manoeuvring-force-based model were used. The nonlinear Mathieu equation can predict parametric roll well as shown in chapter 2; however, it could not estimate the roll motion

with higher advance speed. Then, the manoeuvring-force-based 4-dof model proposed by Kubo et al. (2012) was used to estimate ship motion with higher speed. This model was well validated by model experiment of pure loss of stability. Finally, it is experimentally and numerically revealed that parametric roll and pure loss of stability can be distinguished and there is a difference on their mechanism.

4.2 2:*n* Parametric Roll Region

Parametric roll in regular longitudinal waves has been estimated by the Mathieu-type models as introduced in section 2.3. In this section, the 1-dof model, Eq. 2.3.1, is also used to estimate 2:*n* parametric roll and is rearranged into Eq. 4.2.1:

$$\ddot{\phi} + 2\alpha\left(\phi,\, \dot{\phi}\right)\dot{\phi} + \omega_{\phi}{}^{2}\ \frac{GZ_{wave}\left(t,\, \phi\right)}{GM}\phi = 0\,. \tag{4.2.1}$$

Here, GZ_{wave} is the sum of the GM variation in waves, GM_{vari}, and GZ in calm water, GZ_{calm} and is estimated based on the Froude Krylov assumption. The roll damping coefficients are estimated based on the Ikeda's simplified method (Kawahara et al., 2012) with the lift component of Ikeda's original method (Ikeda, 2004) as shown in section 5.1. Equation 4.2.1 is numerically solved by the Runge-Kutta method with an initial condition is as follows: roll angle is –1.0 [deg], roll angular velocity is 0.0 [deg s^{-1}], and ship gravitational centre locates at a wave trough when t = 0. The incident wave is a following regular longitudinal wave whose length is equal to the ship length and steepness is 0.07. The calculated maximum and minimum roll angle under steady states are shown in Fig. 4.2.1. The 2:1, 2:2, 2:3, and 2:4 parametric rolls are obtained by the calculation. The examples of time series of 2:*n* parametric roll responses when the ship meets two waves are shown in Fig. 4.2.2. It shows that the ship rolls *n* times in two waves. Here, the 2:1 and 2:3 parametric rolls have twice the period of the wave encounter one and show the same magnitude of roll in port and starboard side. In contrast, the 2:2 and 2:4 parametric rolls have the same period as the wave encounter one and show a certain shift in roll. This shift is derived from the term whose coefficient periodically varies. For example, substituting roll whose period is the same as the wave encounter one, $\phi = A\cos\left(\omega_e t\right)$, into the term that causes parametric roll, $M\cos\left(\omega_e t\right)\phi$, a constant term is derived as Eq. 4.2.2: $T_\phi = T_e$

$$M\cos\left(\omega_e t\right)\cdot A\cos\left(\omega_e t\right) = \frac{M\,A}{2}\left[1+\cos\left(2\,\omega_e t\right)\right]. \tag{4.2.2}$$

This constant term yields the shift in the 2:2 and 2:4 parametric rolls. In contrast, if roll whose period is twice as the wave encounter one is substituted into the term, no constant term can be obtained, so that the 2:1 and 2:3 parametric rolls are symmetrical.

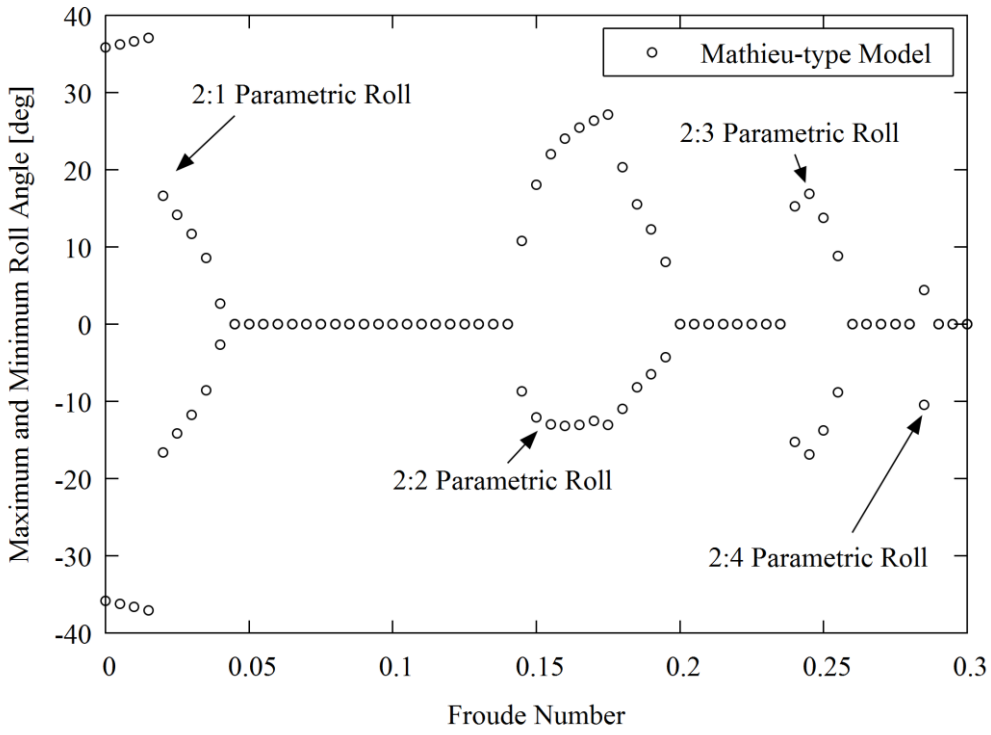

Figure 4.2.1 Maximum and minimum roll angle estimated by the Mathieu-type model.

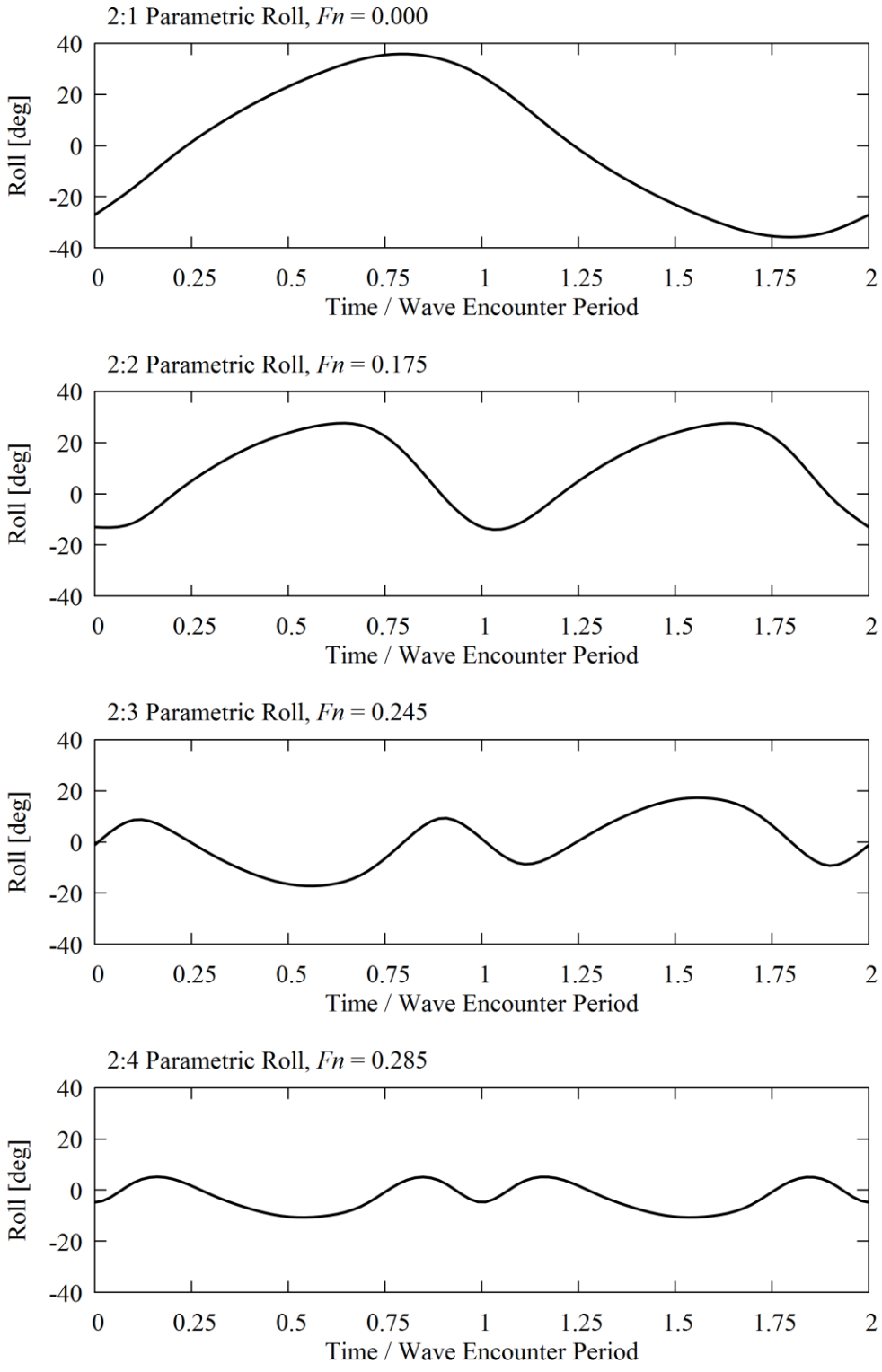

Figure 4.2.2 Examples of 2:*n* parametric roll responses in time series.

4.3 Mathematical Model

Ship motions in following waves are estimated by using the surge-sway-yaw-roll coupled 4-dof model proposed by Kubo et al. (2012). The coordinate systems are shown in Fig. 4.3.1. The 4-dof model is based on a ship maneuvering model as Eq. 4.3.1:

$$
\begin{aligned}
&\left(m+m_x\right)\dot{u} = T\left(u;n_p\right) - R\left(u\right) + \alpha_{corr}\, X_W\left(\xi_G,\eta_G,t,\chi\right) + X_H,\\
&\left(m+m_y\right)\dot{v} = -\left(m+m_x\right)u\,r + Y_W\left(\xi_G,\eta_G,t,u,\chi;n_p\right) + Y_H + Y_R,\\
&\left(I_{zz}+J_{zz}\right)\dot{r} = N_W\left(\xi_G,\eta_G,t,u,\chi;n_p\right) + N_H + N_R,\\
&\left(I_{xx}+J_{xx}\right)\dot{p} = m_x\, z_H\, u\,r + K_W\left(\xi_G,\eta_G,t,u,\chi;n_p\right) + K_H + K_R\\
&\qquad -\left(I_{xx}+J_{xx}\right)\left(\frac{4a}{T_\phi}\dot{\phi} + \frac{3b}{4}\left|\dot{\phi}\right|\dot{\phi}\right) - W\,GZ\left(\zeta_{eff}\left(\xi_G,\eta_G,\chi,\,t\right),\phi\right).
\end{aligned}
\tag{4.3.1}
$$

Here, a space-fixed coordinate system is denoted by O–$\xi\eta\zeta$, and a body-fixed coordinate system is denoted by G–xyz with setting the downward direction as positive in ζ and z. The terms u, v, r, and p are surge, sway, yaw, and roll velocities, respectively. The terms m, I_{xx}, and I_{zz} are a ship mass and inertia moments in roll and yaw, respectively, and m_x, m_y, J_{xx}, and J_{zz} are added masses in surge and sway and added inertia moments in roll and yaw, respectively. The term $T(u;\, n_p)$ is an effective propeller thrust, n_p is a propeller revolution number, $R(u)$ is a ship resistance, and α_{corr} is an empirical correction factor of a diffraction effect proposed by Ito et al. (2014). The terms a and b are linear and quadratic roll extinction coefficients, W is a ship displacement, GZ is a ship roll restoring arm estimated based on Grim's effective wave concept (Grim, 1961), and ζ_{eff} is the effective wave elevation. The coefficients with subscripts G, W, H, and R represent the forces concerned with gravity, wave, hull reaction, and rudder, respectively.

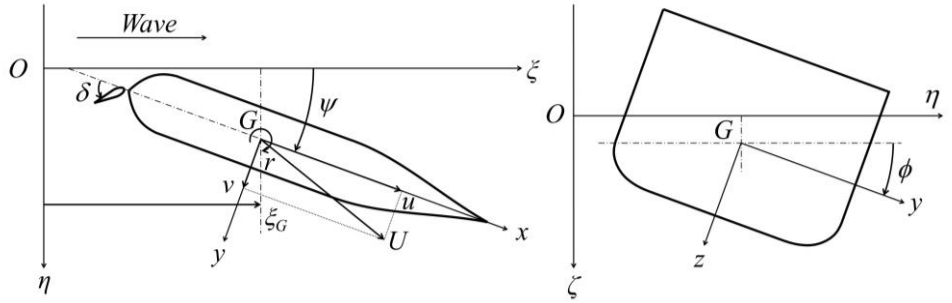

Figure 4.3.1 Coordinate systems

4.4 Modelling of External Forces

The gravity component, i.e. the roll restoring moment, is estimated by using Grim's effective wave concept (Grim, 1961) as shown in subsection 2.5.1.1. The GZ in waves for Grim's effective wave is estimated by changing heave and pitch quasi-statically, i.e. heave and pitch always comply equilibrium in waves for each wave amplitude and heel angle.

The wave induced forces are estimated by the slender body theory with low encounter frequency

assumption (Umeda et al., 1995b) except surge force, which is estimated by Froude Krylov forces with its empirical correction (Ito et al., 2014).

The added masses except that of roll are estimated by using Motora's charts (1959; 1960a; 1960b) and the roll inertia and extinction coefficients are estimated from free roll experiments as shown in section 4.5.1. Yoshimura's experimental values (Yoshimura, 1986) are used as the maneuvering, rudder, and propeller thrust coefficients. The manoeuvring hull, rudder, and propeller thrust coefficients are shown in appendix subject ships.

The ship resistance is estimated to reproduce the free running speed trial tests. When the ship runs at constant speed with a constant propeller revolution number in calm water, the thrust and resistance balance as:

$$R(u) = T(u; n_p). \tag{4.4.1}$$

Since the thrust is estimated by using the constant ship speed and propeller revolution number observed in the speed trial test, the ship resistance at speed u is estimated to comply with Eq. 4.4.1. However, since the ship resistance should be estimated by captive model experiment basically, the estimation of the ship resistance is one of the future tasks in this chapter.

4.4.1 Wave Induced Forces

The wave induced forces are estimated based on the slender body theory with low encounter frequency assumption (Umeda et al., 1995b) and assumed to be proportional to the wave amplitude as Eq. 4.4.1.1-4:

$$X_W(\xi_G, \eta_G, t, \chi) = \zeta_a \left| H_X(\omega, \chi) \right| \cos\left(\omega t - k\xi_G + \varepsilon_X(\omega, \chi)\right), \tag{4.4.1.1}$$

$$\begin{aligned} &Y_W(\xi_G, \eta_G, t, u, \chi; n_p) \\ &= \zeta_a \Big[\left| H_{YF}(\omega, \chi) \right| \cos\left(\omega t - k\xi_G + \varepsilon_{YF}(\omega, \chi)\right) \\ &\quad + \left| H_{YD2}(\omega, \chi) \right| \cos\left(\omega t - k\xi_G + \varepsilon_{YD2}(\omega, \chi)\right) \\ &\quad + \left| H_{YR}(\omega, \chi) \right| \cos\left(\omega t - k\xi_G + \varepsilon_{YR}(\omega, \chi)\right) \Big], \end{aligned} \tag{4.4.1.2}$$

$$\begin{aligned} &N_W(\xi_G, \eta_G, t, u, \chi; n_p) \\ &= \zeta_a \Big[\left| H_{NF}(\omega, \chi) \right| \cos\left(\omega t - k\xi_G + \varepsilon_{NF}(\omega, \chi)\right) \\ &\quad + \left| H_{ND2}(\omega, \chi) \right| \cos\left(\omega t - k\xi_G + \varepsilon_{ND2}(\omega, \chi)\right) \\ &\quad + \left| H_{ND3}(\omega, \chi) \right| \cos\left(\omega t - k\xi_G + \varepsilon_{ND3}(\omega, \chi)\right) \\ &\quad + \left| H_{NR}(\omega, \chi) \right| \cos\left(\omega t - k\xi_G + \varepsilon_{NR}(\omega, \chi)\right) \Big], \end{aligned} \tag{4.4.1.3}$$

$$\begin{aligned} &K_W(\xi_G, \eta_G, t, u, \chi; n_p) \\ &= \overline{OG}\, Y_W(\xi_G, \eta_G, t, u, \chi; n) \end{aligned}$$

$$
\begin{aligned}
&+\zeta_a\Big[\left|H_{KF1}(\omega,\chi)\right|\cos\left(\omega t-k\,\xi_G+\varepsilon_{KF1}(\omega,\chi)\right)\\
&\quad+\left|H_{KF2}(\omega,\chi)\right|\cos\left(\omega t-k\,\xi_G+\varepsilon_{KF2}(\omega,\chi)\right)\\
&\quad+\left|H_{KD2}(\omega,\chi)\right|\cos\left(\omega t-k\,\xi_G+\varepsilon_{KD2}(\omega,\chi)\right)\\
&\quad+\left|H_{KR}(\omega,\chi)\right|\cos\left(\omega t-k\,\xi_G+\varepsilon_{KR}(\omega,\chi)\right)\Big],
\end{aligned}
\tag{4.4.1.4}
$$

where the wave elevation at the ship centre of gravity ζ_w is:

$$
\zeta_w=\zeta_a\cos\left(\omega t-k\,\xi_G+\varepsilon_X(\omega,\chi)\right).
\tag{4.4.1.5}
$$

Here, H and ε with subscripts are the transfer functions and phase differences, respectively: the subscripts F indicates Froude Krylov components, D does diffraction components, and R does rudder components. The term ζ_a, k, and ω are the wave amplitude, number, and frequency, respectively. The above mentioned transfer functions are calculated as follows:

$$
\begin{aligned}
&H_X(\omega,\chi)=H_{XC}(\omega,\chi)+i\,H_{XS}(\omega,\chi),\\
&\begin{cases}
H_{XC}(\omega,\chi)=-\rho\,g\,k\cos\chi\int_{AE}^{FE}C_1(x)\,S(x)\,e^{-k\,d(x)/2}\sin\left(k\,x\cos\chi\right)dx\\
H_{XS}(\omega,\chi)=\rho\,g\,k\cos\chi\int_{AE}^{FE}C_1(x)\,S(x)\,e^{-k\,d(x)/2}\cos\left(k\,x\cos\chi\right)dx
\end{cases},
\end{aligned}
\tag{4.4.1.6}
$$

$$
\begin{aligned}
&H_{YF}(\omega,\chi)=H_{YFC}(\omega,\chi)+i\,H_{YFS}(\omega,\chi),\\
&\begin{cases}
H_{YFC}(\omega,\chi)=\rho\,g\,k\sin\chi\int_{AE}^{FE}C_1(x)\,S(x)\,e^{-k\,d(x)/2}\sin\left(k\,x\cos\chi\right)dx\\
H_{YFS}(\omega,\chi)=-\rho\,g\,k\sin\chi\int_{AE}^{FE}C_1(x)\,S(x)\,e^{-k\,d(x)/2}\cos\left(k\,x\cos\chi\right)dx
\end{cases},
\end{aligned}
\tag{4.4.1.7}
$$

$$
\begin{aligned}
&H_{YD2}(\omega,\chi)=H_{YD2C}(\omega,\chi)+i\,H_{YD2S}(\omega,\chi),\\
&\begin{cases}
H_{YD2C}(\omega,\chi)=-\omega u\sin\chi\left[\rho\,S_y(x)\,e^{-k\,d(x)/2}\cos\left(k\,x\cos\chi\right)\right]_{AE}^{FE}\\
H_{YD2S}(\omega,\chi)=-\omega u\sin\chi\left[\rho\,S_y(x)\,e^{-k\,d(x)/2}\sin\left(k\,x\cos\chi\right)\right]_{AE}^{FE}
\end{cases},
\end{aligned}
\tag{4.4.1.8}
$$

$$
\begin{aligned}
&H_{YR}(\omega,\chi)=H_{YRC}(\omega,\chi)+i\,H_{YRS}(\omega,\chi),\\
&\begin{cases}
H_{YRC}(\omega,\chi)=(1+a_H)\dfrac{\rho}{2}A_R\;f_\alpha\,\varepsilon_w(1-w_p)u\sqrt{1+\kappa_P\dfrac{8K_T}{\pi J^2}}\\
\qquad\qquad\cdot\omega\sin\chi\exp\left(-k\,z_R\right)\cos\left(k\,x_R\cos\chi\right)\\
H_{YRS}(\omega,\chi)=(1+a_H)\dfrac{\rho}{2}A_R\;f_\alpha\,\varepsilon_w(1-w_p)u\sqrt{1+\kappa_P\dfrac{8K_T}{\pi J^2}}\\
\qquad\qquad\cdot\omega\sin\chi\exp\left(-k\,z_R\right)\sin\left(k\,x_R\cos\chi\right)
\end{cases},
\end{aligned}
\tag{4.4.1.9}
$$

$$
H_{NF}(\omega,\chi)=H_{NFC}(\omega,\chi)+i\,H_{YFS}(\omega,\chi),
$$

$$\begin{cases} H_{NFC}(\omega,\chi)=\rho g k \sin\chi \int_{AE}^{FE} C_1(x) S(x) e^{-k d(x)/2}\, x \sin(k x\cos\chi)\, dx \\ H_{NFS}(\omega,\chi)=-\rho g k \sin\chi \int_{AE}^{FE} C_1(x) S(x) e^{-k d(x)/2}\, x \cos(k x\cos\chi)\, dx \end{cases}, \tag{4.4.1.10}$$

$$H_{ND2}(\omega,\chi)=H_{ND2C}(\omega,\chi)+i\,H_{YD2S}(\omega,\chi),$$
$$\begin{cases} H_{ND2C}(\omega,\chi)=\omega u \sin\chi \int_{AE}^{FE} \rho S_y(x) e^{-k d(x)/2} \cos(k x\cos\chi)\, dx \\ H_{ND2S}(\omega,\chi)=\omega u \sin\chi \int_{AE}^{FE} \rho S_y(x) e^{-k d(x)/2} \sin(k x\cos\chi)\, dx \end{cases}, \tag{4.4.1.11}$$

$$H_{ND3}(\omega,\chi)=H_{ND3C}(\omega,\chi)+i\,H_{YD3S}(\omega,\chi),$$
$$\begin{cases} H_{ND3C}(\omega,\chi)=-\omega u \sin\chi \left[\rho S_y(x) e^{-k d(x)/2}\, x\cos(k x\cos\chi)\right]_{AE}^{FE} \\ H_{ND3S}(\omega,\chi)=-\omega u \sin\chi \left[\rho S_y(x) e^{-k d(x)/2}\, x\sin(k x\cos\chi)\right]_{AE}^{FE} \end{cases}, \tag{4.4.1.12}$$

$$H_{NR}(\omega,\chi)=H_{NRC}(\omega,\chi)+i\,H_{NRS}(\omega,\chi),$$
$$\begin{cases} H_{NRC}(\omega,\chi)=(x_R+a_H\, x_H)\dfrac{\rho}{2} A_R\, f_\alpha\, \varepsilon_w (1-w_p) u \sqrt{1+\kappa_P \dfrac{8K_T}{\pi J^2}} \\ \qquad\qquad \cdot \omega \sin\chi \exp(-k\, z_R)\cos(k\, x_R \cos\chi) \\ H_{YRS}(\omega,\chi)=(x_R+a_H\, x_H)\dfrac{\rho}{2} A_R\, f_\alpha\, \varepsilon_w (1-w_p) u \sqrt{1+\kappa_P \dfrac{8K_T}{\pi J^2}} \\ \qquad\qquad \cdot \omega \sin\chi \exp(-k\, z_R)\sin(k\, x_R \cos\chi) \end{cases}, \tag{4.4.1.13}$$

$$H_{KF1}(\omega,\chi)=H_{KF1C}(\omega,\chi)+i\,H_{KF1S}(\omega,\chi),$$
$$\begin{cases} H_{KF1C}(\omega,\chi)=\rho g k \sin\chi \int_{AE}^{FE} C_1(x) \dfrac{B(x)}{2}\left[d(x)\right]^2 \\ \qquad\qquad \cdot e^{-k d(x)/2} \sin(k x\cos\chi)\, dx \\ H_{KF1S}(\omega,\chi)=-\rho g k \sin\chi \int_{AE}^{FE} C_1(x) \dfrac{B(x)}{2}\left[d(x)\right]^2 \\ \qquad\qquad \cdot e^{-k d(x)/2} \cos(k x\cos\chi)\, dx \end{cases}, \tag{4.4.1.14}$$

$$H_{KF2}(\omega,\chi)=H_{KF2C}(\omega,\chi)+i\,H_{KF2S}(\omega,\chi),$$

$$\begin{cases} H_{KF2C}(\omega,\chi) = \rho g k^2 \sin\chi \int_{AE}^{FE} C_4(x)\left[\dfrac{B(x)}{2}\right]^3 d(x) \\ \qquad\qquad \cdot e^{-k\,d(x)/2}\sin\left(k\,x\cos\chi\right)dx \\ H_{KF2S}(\omega,\chi) = -\rho g k^2 \sin\chi \int_{AE}^{FE} C_4(x)\left[\dfrac{B(x)}{2}\right]^3 d(x) \\ \qquad\qquad \cdot e^{-k\,d(x)/2}\cos\left(k\,x\cos\chi\right)dx \end{cases}, \tag{4.4.1.15}$$

$$H_{KD2}(\omega,\chi) = H_{KD2C}(\omega,\chi) + i\,H_{KD2S}(\omega,\chi),$$

$$\begin{cases} H_{KD2C}(\omega,\chi) = -\omega u \sin\chi\left[\rho S_y(x) l_\eta(x) e^{-k\,d(x)/2}\cos\left(k\,x\cos\chi\right)\right]_{AE}^{FE} \\ H_{KD2S}(\omega,\chi) = -\omega u \sin\chi\left[\rho S_y(x) l_\eta(x) e^{-k\,d(x)/2}\sin\left(k\,x\cos\chi\right)\right]_{AE}^{FE} \end{cases}, \tag{4.4.1.16}$$

$$H_{KR}(\omega,\chi) = H_{KRC}(\omega,\chi) + i\,H_{KRS}(\omega,\chi),$$

$$\begin{cases} H_{KRC}(\omega,\chi) = -(1+a_H) z_{HR} \dfrac{\rho}{2} A_R\, f_\alpha\, \varepsilon_w (1-w_p) u \sqrt{1+\kappa_P \dfrac{8K_T}{\pi J^2}} \\ \qquad\qquad \cdot \omega \sin\chi \exp\left(-k\,z_R\right)\cos\left(k\,x_R\cos\chi\right) \\ H_{KRS}(\omega,\chi) = -(1+a_H) z_{HR} \dfrac{\rho}{2} A_R\, f_\alpha\, \varepsilon_w (1-w_p) u \sqrt{1+\kappa_P \dfrac{8K_T}{\pi J^2}} \\ \qquad\qquad \cdot \omega \sin\chi \exp\left(-k\,z_R\right)\sin\left(k\,x_R\cos\chi\right) \end{cases}, \tag{4.4.1.17}$$

where

$$C_1(x) = \frac{\sin\left(k\dfrac{B(x)}{2}\sin\chi\right)}{k\dfrac{B(x)}{2}\sin\chi}, \tag{4.4.1.18}$$

$$C_4(x) = \frac{2\left[\sin\left(k\dfrac{B(x)}{2}\sin\chi\right) - k\dfrac{B(x)}{2}\sin\chi\cos\left(k\dfrac{B(x)}{2}\sin\chi\right)\right]}{\left[k\dfrac{B(x)}{2}\sin\chi\right]^3}, \tag{4.4.1.19}$$

$$J = \frac{(1-w_P)u}{n_p D_P}, \quad f_\alpha = \frac{6.13\Lambda}{2.25+\Lambda}. \tag{4.4.1.20}$$

Here, $B(x)$, $d(x)$, $S(x)$, $l_\eta(x)$, and $S_y(x)$ are the breadth, depth, sectional area, lever of added mass, and added mass in sway direction which are defined on each cross section located at a position by x away from midship in longitudinal direction of the ship, respectively. The term a_H: the interaction factor

for rudder force between hull and rudder, x_H: the longitudinal position of rudder force due to interaction between hull and rudder, x_R: the longitudinal rudder position, A_R: the rudder area, f_α: the hydrodynamic rudder lift slope, D_P: the propeller diameter, K_T: the thrust coefficient, w_P: the wake ratio between hull and propeller, and ε_w: the wake fraction ratio between propeller and rudder positions. The phase differences ε are calculated by using real and imaginary part of the transfer functions as Eq. 4.4.1.21:

$$\varepsilon = -\mathrm{Arctan}\left(\frac{\mathrm{Im}(H)}{\mathrm{Re}(H)}\right) = -\mathrm{Arctan}\left(\frac{H_S}{H_C}\right). \tag{4.4.1.21}$$

4.4.2 Manoeuvring Hull and Rudder Forces

Yoshimura's experimental values (Yoshimura, 1986) is used as the hull reaction, rudder, and propeller thrust coefficients. The nondimensionalized values are shown in appendix subject ships. He used the similar ship with the subject ship in this chapter. The manoeuvring hull and rudder forces are modelled as Eq. 4.4.2.1-8:

$$X_H = \frac{1}{2}\rho L d U^2 \left(X_{vv}' v'^2 + X_{vr}' v' r' + X_{rr}' r' + X_{vvvv}' v'^4 + X_{vvvr}' v'^3 r' \right), \tag{4.4.2.1}$$

$$Y_H = \frac{1}{2}\rho L d U^2 \left(Y_v' v' + Y_r' r' + Y_{vvv}' v'^3 + Y_{vvr}' v'^2 r' + Y_{vrr}' v' r'^2 + Y_{rrr}' r'^3 \right), \tag{4.4.2.2}$$

$$\begin{aligned} Y_R = &-(1+a_H)\frac{\rho}{2} A_R f_\alpha \varepsilon_R^2 (1-w_p)^2 u^2 \left(1+\kappa_P \frac{8K_T}{\pi J^2}\right)\delta \\ &-(1+a_H)\frac{\rho}{2} A_R f_\alpha \gamma_R \varepsilon_R (1-w_p) u \sqrt{1+\kappa_P \frac{8K_T}{\pi J^2}} (v + l_R r), \end{aligned} \tag{4.4.2.3}$$

$$\begin{aligned} N_H = &\frac{1}{2}\rho L^2 d U^2 \left(N_v' v' + N_r' r' \right. \\ &\left. + N_{vvv}' v'^3 + N_{vvr}' v'^2 r' + N_{vrr}' v' r'^2 + N_{rrr}' r'^3 \right), \end{aligned} \tag{4.4.2.4}$$

$$\begin{aligned} N_R = &-(x_R + a_H x_H)\frac{\rho}{2} A_R f_\alpha \varepsilon_R^2 (1-w_p)^2 u^2 \left(1+\kappa_P \frac{8K_T}{\pi J^2}\right)\delta \\ &-(x_R + a_H x_H)\frac{\rho}{2} A_R f_\alpha \gamma_R l_R \varepsilon_R (1-w_p) u \sqrt{1+\kappa_P \frac{8K_T}{\pi J^2}} (v + l_R r), \end{aligned} \tag{4.4.2.5}$$

$$K_H = -z_H Y_H, \tag{4.4.2.6}$$

$$K_R = -z_{HR} Y_R, \tag{4.4.2.7}$$

$$U = \sqrt{u^2 + v^2}, \quad v' = \frac{v}{U}, \quad r' = \frac{rL}{U}. \tag{4.4.2.8}$$

Here, L is a ship length, δ is rudder angle, z_H is a vertical position of the centre of the lateral manoeuvring force and z_{HR} is vertical position of the rudder. The flow straightening effect is included as linear effects on the rudder forces.

4.4.3 Thrust and Ship Resistance

Yoshimura's experimental values (Yoshimura, 1986) is used as the propeller thrust coefficients and the values are available in section 5.4. However, since the ship resistance is not available in his paper, speed trial data in the experiment are used to estimate the ship resistance. Generally, the ship resistance is estimated by a captive model experiment, so that it is a future task. First, the effective thrust T is estimated as Eq. 4.3.3-1:

$$T\left(u;n_p\right)=\left(1-t_p\right)\rho n_p{}^2 D_p^4 K_T\left(J\right). \tag{4.4.3.1}$$

Here, t_p: thrust reduction coefficient. When the ship runs with constant speed in calm water, the thrust and ship resistance balance as Eq. 4.4.1. The thrust coefficient is approximated by quadratic equation as Eq. 4.4.3.2:

$$\begin{aligned} K_T\left(J\right) &= \tau_0+\tau_1 J+\tau_2 J^2 \\ &= \tau_0+\tau_1\frac{\left(1-w_P\right)}{D_P}\frac{u}{n_p}+\tau_2\frac{\left(1-w_P\right)^2}{D_P{}^2}\left(\frac{u}{n_p}\right)^2. \end{aligned} \tag{4.4.3.2}$$

Substituting Eq. 4.4.3.2 into Eq. 4.4.3.1, the thrust is expressed as Eq. 4.3.3.3:

$$\begin{aligned} T\left(u;n_p\right) &= \left(1-t_p\right)\rho n_p{}^2 D_p^4\left[\tau_0+\tau_1\frac{\left(1-w_P\right)}{D_P}\frac{u}{n_p}+\tau_2\frac{\left(1-w_P\right)^2}{D_P{}^2}\left(\frac{u}{n_p}\right)^2\right] \\ &= \left(1-t_p\right)\rho D_p^4\left[\tau_0 n_p{}^2+\tau_1\frac{\left(1-w_P\right)}{D_P}u n_p+\tau_2\frac{\left(1-w_P\right)^2}{D_P{}^2}u^2\right]. \end{aligned} \tag{4.4.3.3}$$

Approximating the propeller revolution number n_p as a quadratic function of the ship speed u from the speed trial test, the calm-water resistance is expressed as a quartic function of the ship speed u.

4.5 Model Experiment

To investigate the 2:n parametric roll in following waves, experiments using a 1/53.471 scaled model of the 180 m-long pure car carrier were performed at the seakeeping and manoeuvring basin of the National Research Institute of Fisheries Engineering. The technique of free running model experiment is shown in appendix subject ships. The principal particulars of the vessel are listed also in appendix subject ships.

4.5.1 Roll Decay with Advance Speed

To treat nonlinear roll motions in a wide frequency range i.e. wide speed range, the speed effect on the roll damping should be considered. Thus, roll decay tests with several advance speeds are conducted by rotating a propeller installed on the model with propeller revolution speed of 0, 300,

450, 600, 900, and 1200 rpm. The observed ship speeds are 0.0, 0.067, 0.078, 0.13, 0.20, and 0.26 in Froude number, respectively. The obtained linear roll extinction coefficients are shown in Fig. 4.3-1. Here, speed effect on quadratic roll extinction coefficient is neglected because enough large initial heel cannot be given in running roll decay tests.

Roll damping can be divided in friction, eddy, lift, wave making, and bilge keel components. It is known that the eddy one decreases linearly with advance speed, the lift one increases linearly with advance speed, and the others excepting the wave making one are almost constant against variance of advance speed (Ikeda et al., 1978). The wave making component is actually affected by the ship advance speed and the qualitative change appears at Hanaoka's parameter of 0.25. The point indicates the change of wave pattern induced by the advancing ship. Hanaoka's parameter τ is calculated as Eq. 4.5.1.1:

$$\tau = \frac{U\,\omega_e}{g}. \tag{4.5.1.1}$$

Here, the encounter frequency ω_e indicates the frequency of ship motion in waves, so that the natural roll frequency is used instead to estimate τ of the roll decay test with advance speed. The Froude number that complies τ = 0.25 is 0.217 for this ship. Thus, although the wave making component is affected with advance speed around *Fn* of 0.217, the effect cannot be clearly seen in the experimental results (Fig. 4.5.1.1). Then, the qualitative change around τ = 0.25 is neglected and the wave making component is assumed to be constant with a ship speed in this study. Finally, the roll extinction coefficients are approximated as Eq. 4.5.1.2:

$$a(Fn) = \begin{cases} 0.0562 + 0.703Fn & (Fn < 0.0696) \\ 0.00420 + 1.45Fn & (Fn \geq 0.0696) \end{cases},$$
$$b = 0.0110. \tag{4.5.1.2}$$

The linear extinction coefficient (*Fn* is smaller than 0.0696) is approximated by using three points from lower speed in Fig. 4.3-1 and the linear extinction coefficient (*Fn* is greater than or equal to 0.0696) is approximated by using five points from higher speed in Fig. 4.5.1.1. The natural roll period is determined to express the large amplitude of roll decay without advance speed in Fig. 4.5.1.2. The time series of roll decay with advance speed shows good agreement for each advance speed but the estimated roll period is a little longer than that of the experiment. An example of roll decay comparison with advance speed, *Fn* of 0.128, is shown can be seen in Fig. 4.5.1.3.

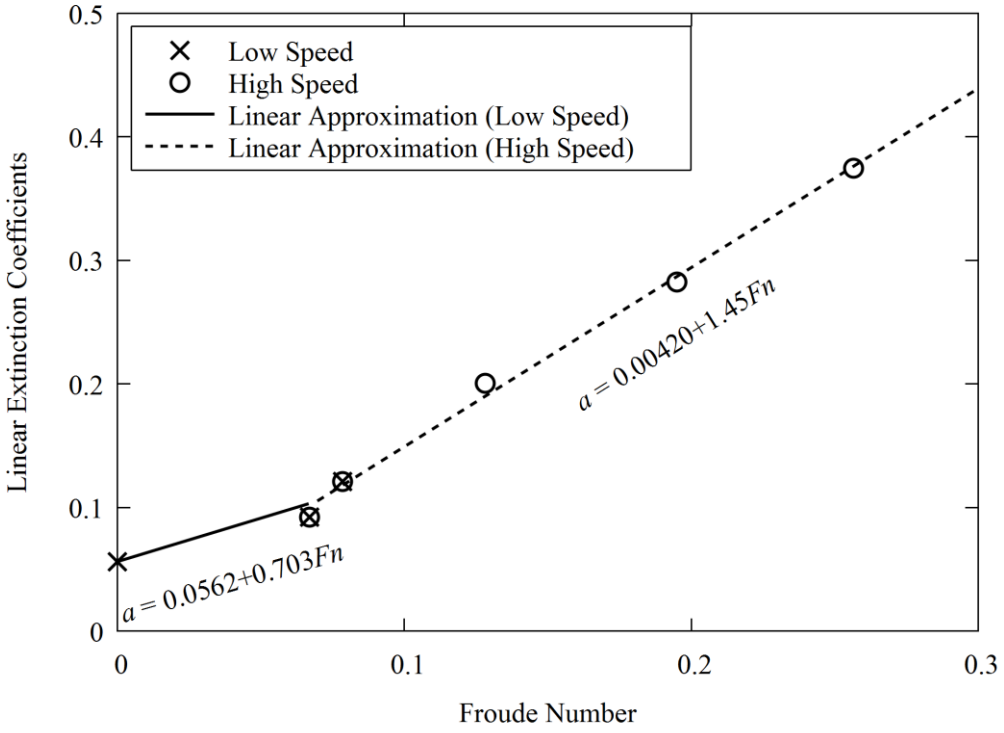

Figure 4.5.1.1 Linear roll extinction coeficients with several advance speeds.

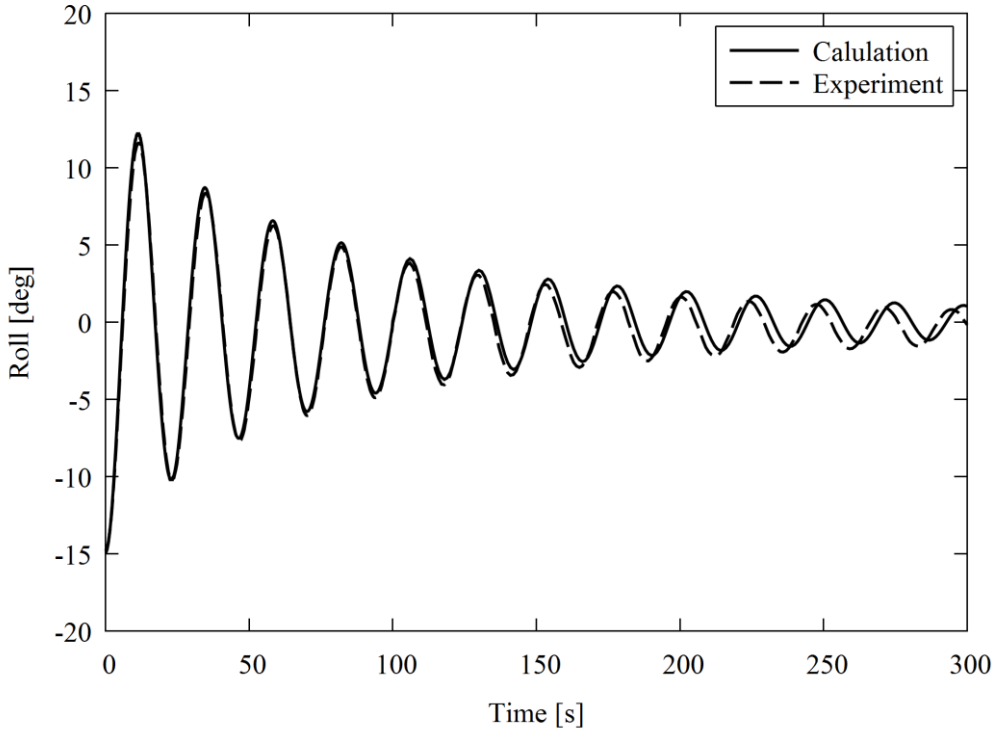

Figure 4.5.1.2 Roll decay witohut advance speed.

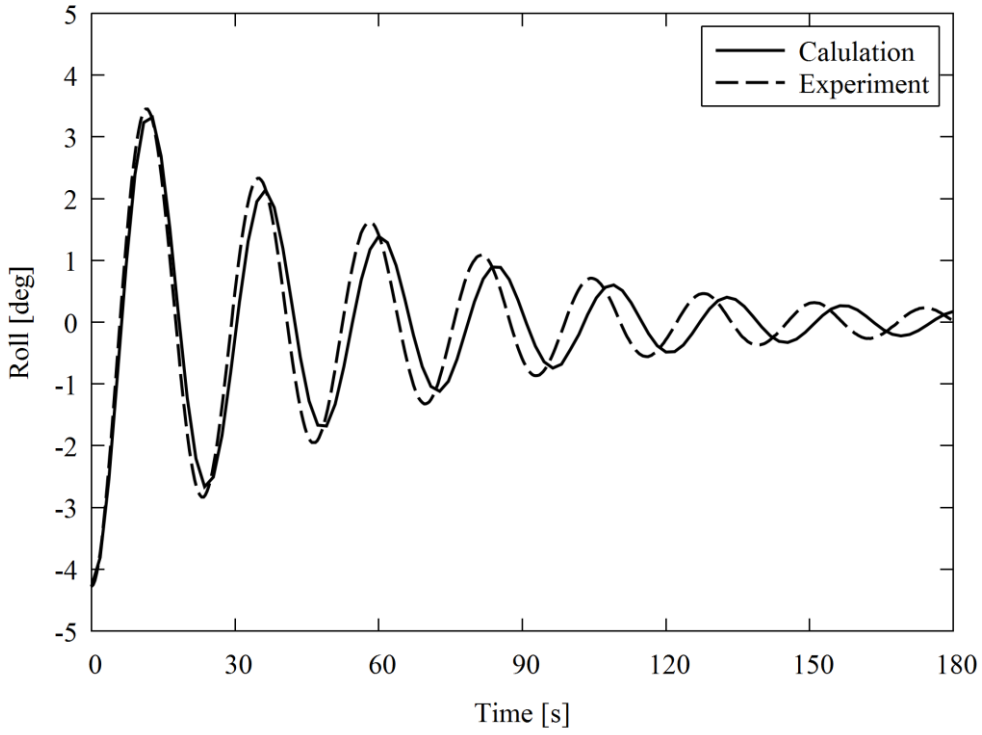

Figure 4.5.1.3 Example of roll decay with advance speed, *Fn* of 0.128.

4.5.2 Speed Trial Test

The ship resistance is estimated by speed trial test. Figure 4.5.2.1 shows the relationship between propeller revolution number and ship speed in the speed trial tests in the full scale. The propeller revolution number is approximated by a quadratic equation that passes the point (u, n_p) = (0, 0). The quadratic equation is as Eq. 4.5.2.1:

$$n_p = 0.2361u + 0.003212u^2 . \tag{4.5.2.1}$$

Following Eq. 4.4.1, 4.4.3.3, and 4.5.2.1, the ship resistance are estimated as Eq. 4.5.2.2:

$$R(u) = 1058u^2 + 42.11u^3 + 0.3475u^4 . \tag{4.5.2.2}$$

The ship resistance estimated from speed trial tests with and without polynomial fitting as Eq. 4.5.2.2 are compared in Fig. 4.5.2.2.

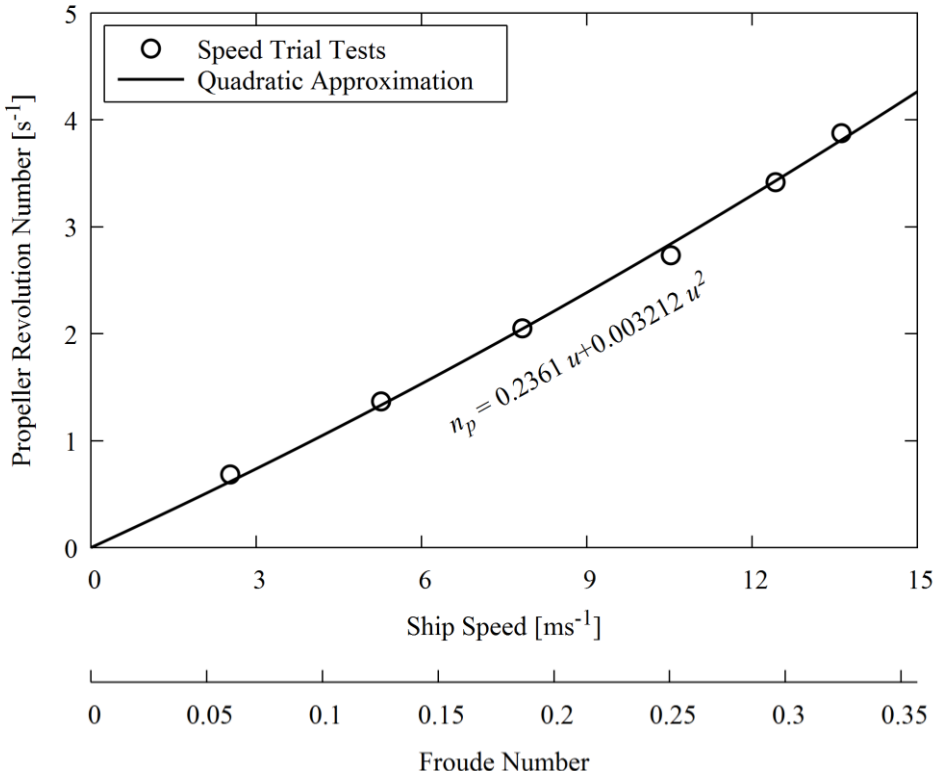

Figure 4.5.2.1 Relationship between propeller revolution number and ship speed in the speed trial test.

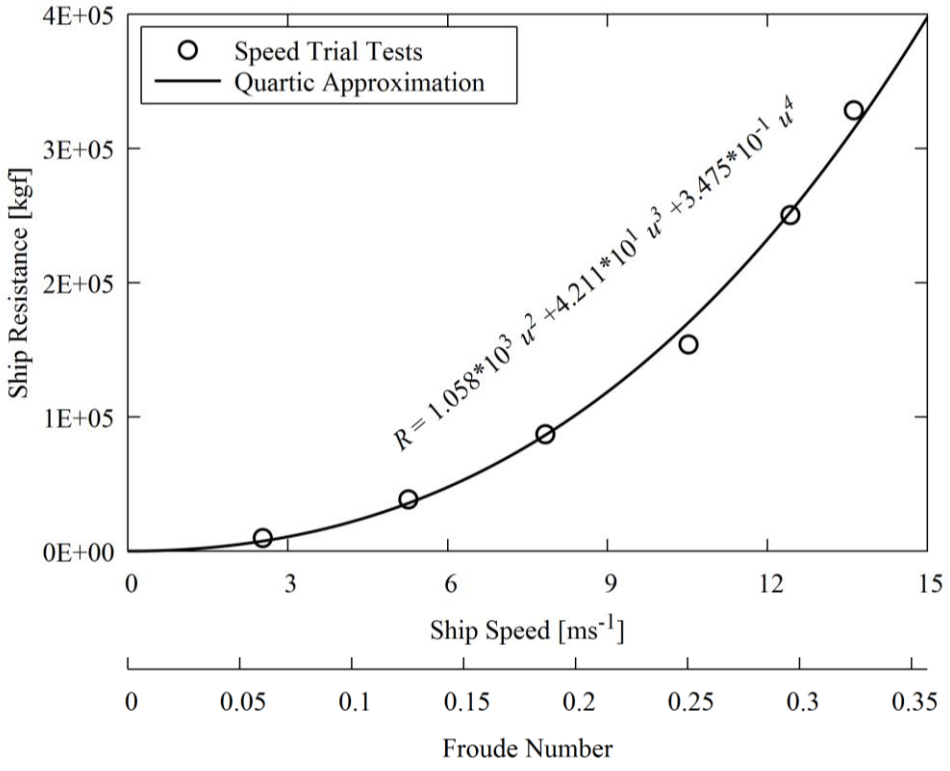

Figure 4.5.2.2 Ship resistance in calm water in real ship scale.

4.5.3 Free Running Experiment

The free running experiment was performed for regular following waves. The wavelength to ship length ratio was 1.00, and the wave steepness was 0.07. The auto pilot course was set to –10° in the wave direction because the ship course cannot be estimated in pure-following waves due to the asymmetric roll of 2:2 parametric roll. The rudder angle was controlled according to proportional and differential control with the proportional gain of 3.0 and differential gain of 38.35 [s] in the model scale. The propeller revolution number ranged from 550 to 1700 [rpm] with an interval of 100 [rpm] in the model scale. Here, 1750 [rpm] could not be achieved due to the limitation of the motor, so that the maximum propeller revolution was set to 1700 [rpm].

The observed maximum and minimum roll angle are shown in Fig. 4.5.3.1 without the result of 1650 [rpm]. This is because the observed motion in the case of 1650 [rpm] showed very large heading less than –40°, although the auto pilot course was set to –10° and the observed heading angles in other cases were more than –20°. This may be because the too large heading was given in this case when the ship model was launched. In spite of the small interval of the propeller revolution number change, the observed ship speed changed discontinuously as shown in Fig. 4.5.3.1. To show the discontinuity more clearly, the relationship between the propeller revolution number and ship speed is plotted in Fig. 4.5.3.2. This figure clarifies the discontinuous change of the ship speed around propeller revolution number of 1250 and 1350 [rpm].

The time series of roll, pitch, yaw, and wave elevation at the centre of gravity in some cases are shown in Fig. 4.5.3.3-7. These figures show the observed ship model motions while the ship model meets three waves so that steady state of motions can be seen. Figure 4.5.3.3 (Fn of 0.135) and 4.5.3.4 (Fn of 0.177) show that the maximum peaks of roll and pitch have almost the same phase of –90° from a wave trough. By contrast, Fig. 4.5.3.5 (Fn of 0.217) shows that the phase difference between roll and pitch is 90° and that the maximum peaks of roll has the phase of –180° from a wave trough. These differences in the phases indicate that the roll motion of $Fn < 0.2$ is different from that of $Fn > 0.2$ in Fig. 4.5.3.1. In Fig. 4.5.3.6-7, no significant roll motion cannot be seen, and pitch and wave elevation indicate that the ship model stays longer time around a down slope of a wave. This motion is close to surf-riding, and the ship model may suffer surf-riding after a while or with a little larger propeller revolution number. However, surf-riding is not observed due to the limitation of the length of the basin and motor of the propeller. In this chapter, only the large roll motions of $Fn < 0.25$ in Fig. 4.5.3.1 are discussed. This is because the experimental result shows that the roll motions of $Fn > 0.25$ is not so significant.

Parametric roll is excited by a periodic variation of a roll restoring coefficient: the restoring coefficient is small when the roll increases, and it is large when the roll decreases. Since it varies depending on the water area, it is small when the wave crest locates amidship, and it is large when a wave trough locates amidship for general ships. Thus, a maximal roll due to parametric roll appears after a wave crest passes through the ship gravitational center. From this point of view, the phenomenon in Fig. 4.5.3.3-4 is parametric roll; however, the phenomenon in Fig. 4.5.3.5 is not parametric roll because the maximal roll appears when the wave crest locates around the ship gravitational center. On the other hand, pure loss of stability is a large heel caused by a long time

decrease of stability. This mechanism indicates that the maximum heel due to pure loss of stability appears when the wave crest locates around the ship gravitational center. Thus, the phenomenon in Fig. 4.5.3.5 can be judged as pure loss of stability.

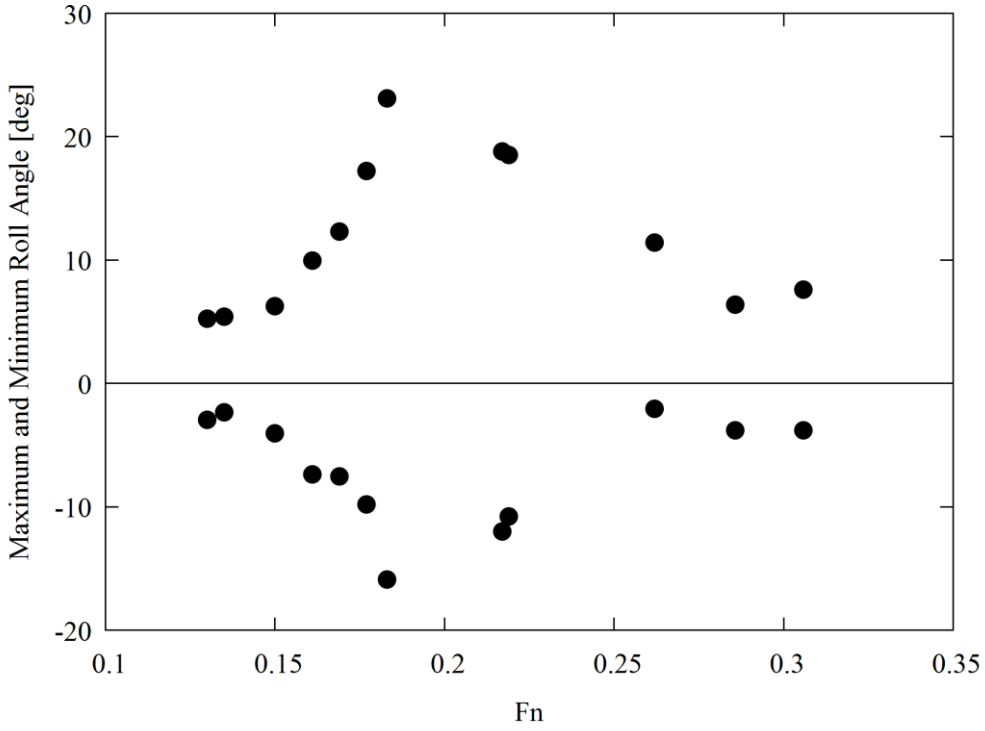

Figure 4.5.3.1 Maximum and minimum roll angle observed in the free running model experiment.

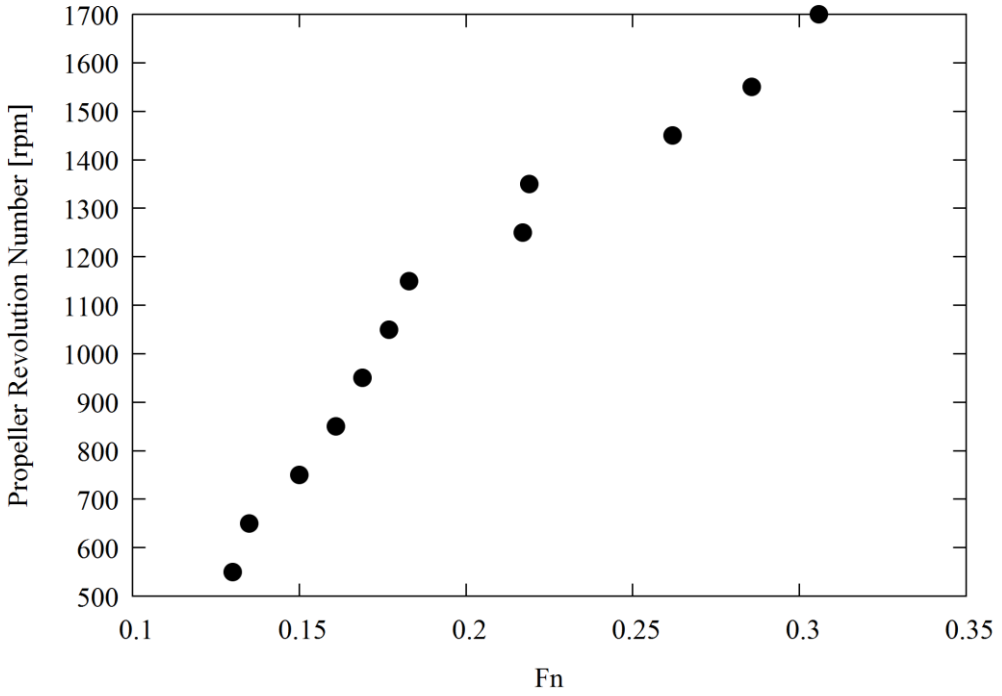

Figure 4.5.3.2 Relationship between propeler revolution number and ship speed under free running condition in waves.

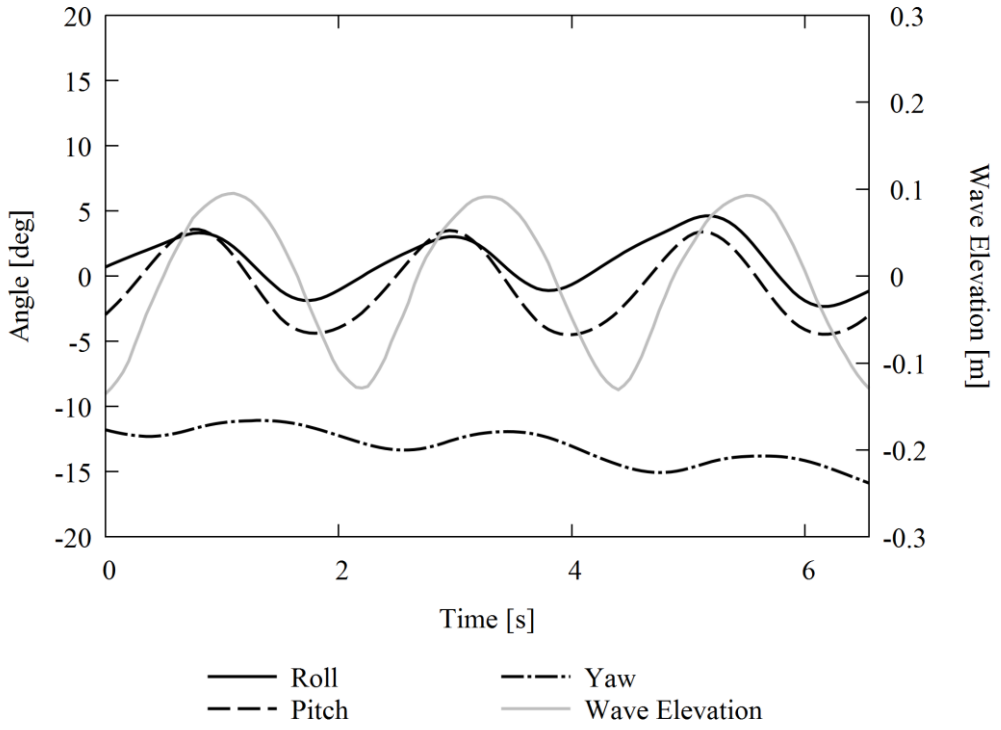

Figure 4.5.3.3 Time series of roll, pitch, yaw, and wave elevation in the case of 650 [rpm] (*Fn* of 0.135).

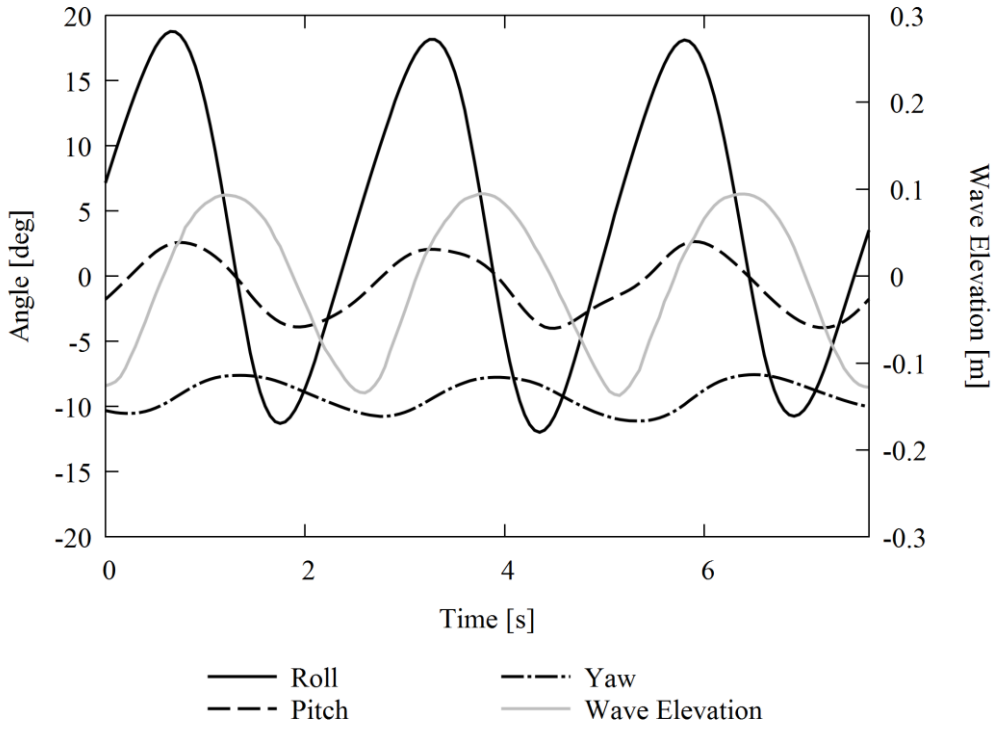

Figure 4.5.3.4 Time series of roll, pitch, yaw, and wave elevation in the case of 1050 [rpm] (*Fn* of 0.177).

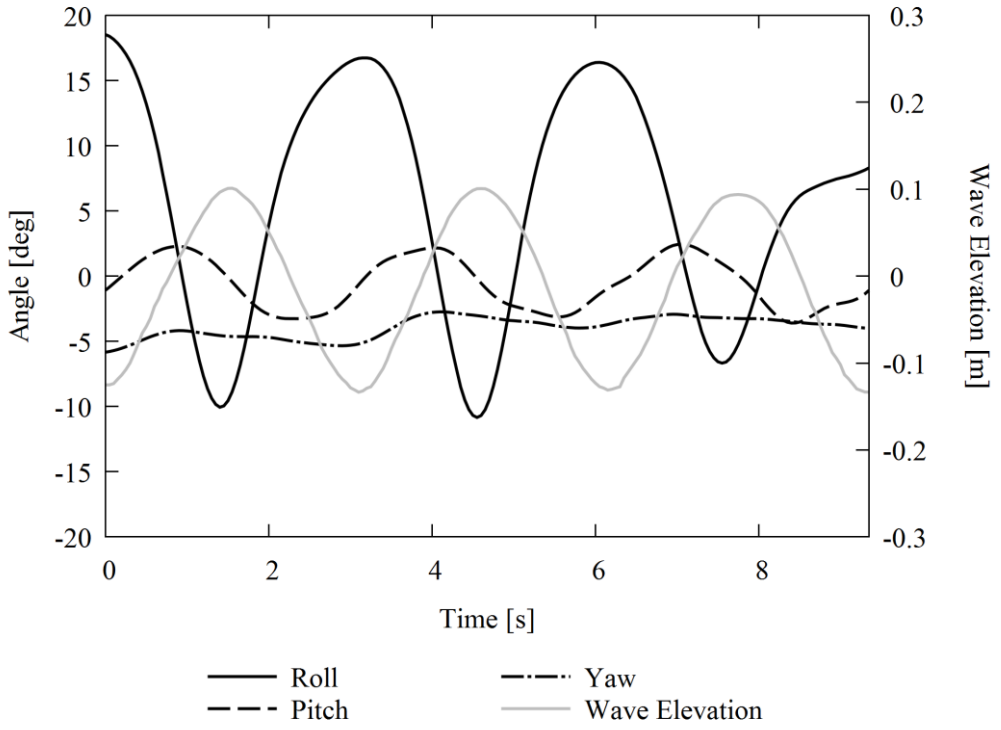

Figure 4.5.3.5 Time series of roll, pitch, yaw, and wave elevation in the case of 1250 [rpm] (*Fn* of 0.217).

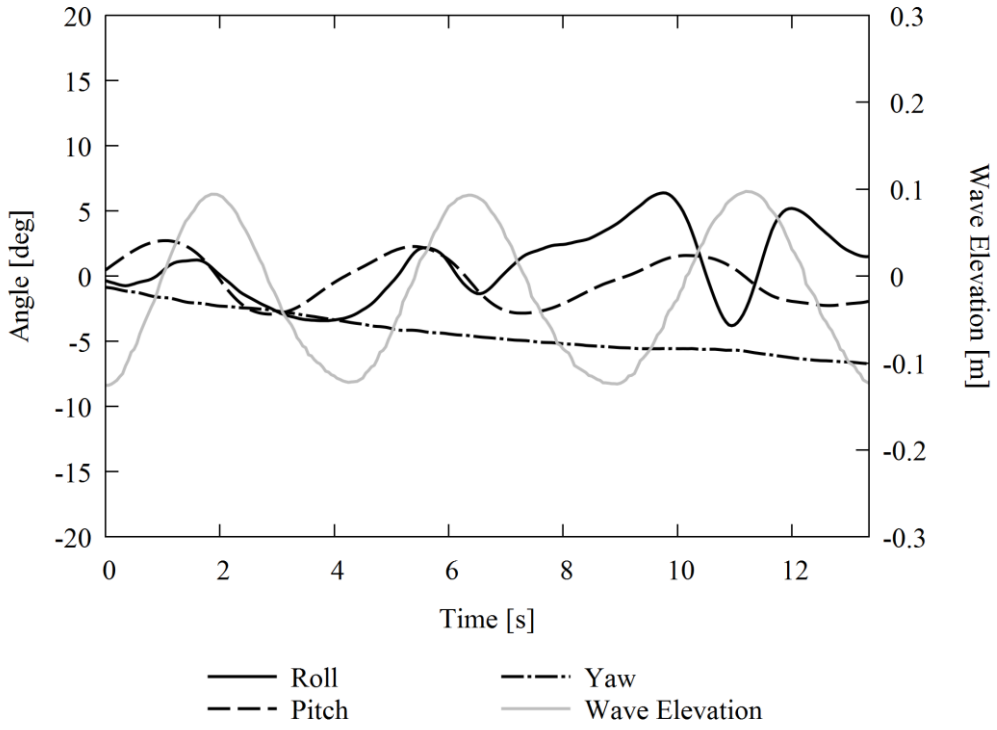

Figure 4.5.3.6 Time series of roll, pitch, yaw, and wave elevation in the case of 1450 [rpm] (*Fn* of 0.262).

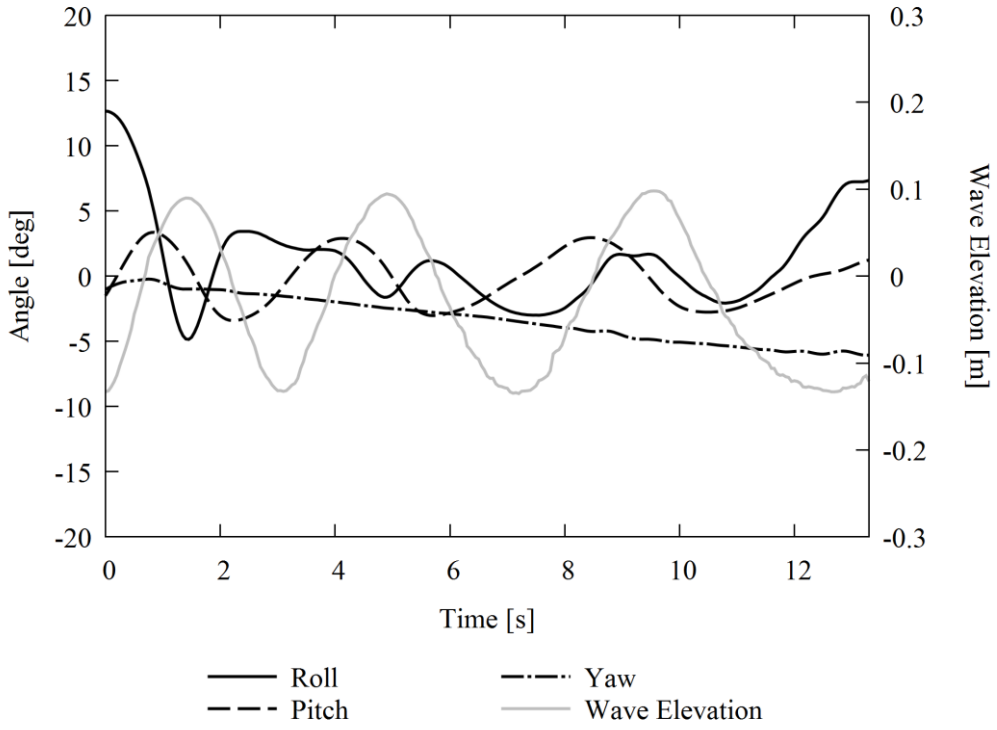

Figure 4.5.3.7 Time series of roll, pitch, yaw, and wave elevation in the case of 1700 [rpm] (*Fn* of 0.306).

4.6 Ship Roll Response in Following Waves

In this section, experimental results are investigated by using the nonlinear Mathieu equation as shown in section 4.2 and 4-dof model as shown in section 4.3 and 4.4. The experimentally obtained ship roll responses in regular following waves as shown in section 4.5.3 show that two kinds of roll responses appear when the propeller rotational number is changed little by little.

4.6.1 Parametric Roll Region by the Nonlinear Mathieu Equation

The maximum and minimum roll angle in the experiment and nonlinear Mathieu equation are compared in Fig. 4.6.1.1. As section 4.5.3, roll response of $Fn < 0.2$ can be judged as 2:2 parametric roll from the viewpoint of the phase between roll and wave elevation. Moreover, the nonlinear Mathieu equation estimates the 2:2 parametric roll around Fn of 0.15 to 0.2. Thus, the experimentally obtained roll response of $Fn < 0.2$ can be also judged as 2:2 parametric roll from this point of view. However, the amplitude is not estimated well. For the roll response of $Fn > 0.2$, the nonlinear Mathieu equation cannot explain the experimental result at all. This is because pure loss of stability can be estimated by taking into account manoeuvring motions but they are not included in the nonlinear Mathieu equation.

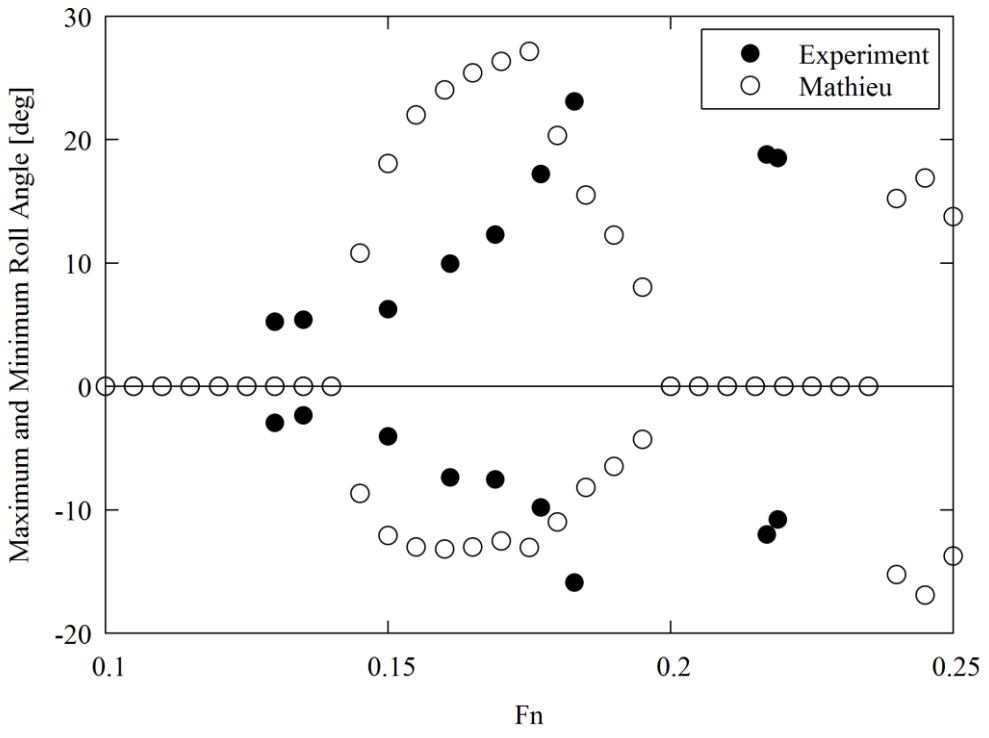

Figure 4.6.1.1 Maximum and minimum roll angle in the nonlinear Mathieu equation and experiment.

4.6.2 Pure Loss of Stability Region by 4-degree-of-freedom Model

Numerically simulated and experimentally observed maximum and minimum roll angles are compared in Fig. 4.6.2.1. The 4-dof model shows good agreement with experimental results of $Fn >$

0.2. This indicates that the 4-dof model, which is based on maneuvering model by assuming long-period motions, can accurately estimate the ship roll motion with higher advance speed. From the contraposition of this, the ship roll motion is not based on manoeuvring model but frequency-based model where the 4-dof model cannot provide good estimation. This also suggests that the two kinds of observed roll motions are based on the other mechanism. Further, the phase difference of maximum and minimum roll from the trough of the wave elevation at the ship gravitational centre are shown in Fig. 4.6.2.2-3. Since the phase differences show good agreement in whole range, it can be said that the 4-dof model can also explain 2:2 parametric roll qualitatively but not quantitatively.

Although the propeller revolution number is changed little by little, the experimental data around Froude number of 0.2 was not obtained. On the other hand, the result of 4-dof model shows very smooth transition of roll motion from the 2:2 parametric roll to pure loss of stability. This conflict should be examined by using a numerical simulation which can estimate both frequency-based motion and manoeuvring-based motion in the future.

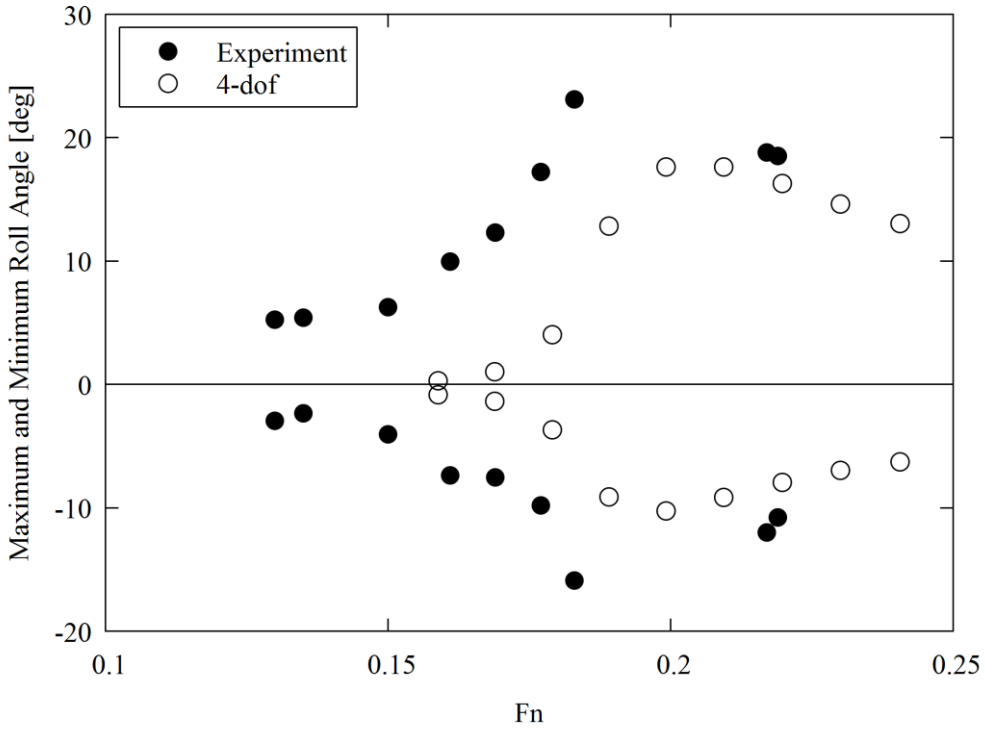

Figure 4.6.2.1 Maximum and minimum roll angle in the 4-dof model and experiment.

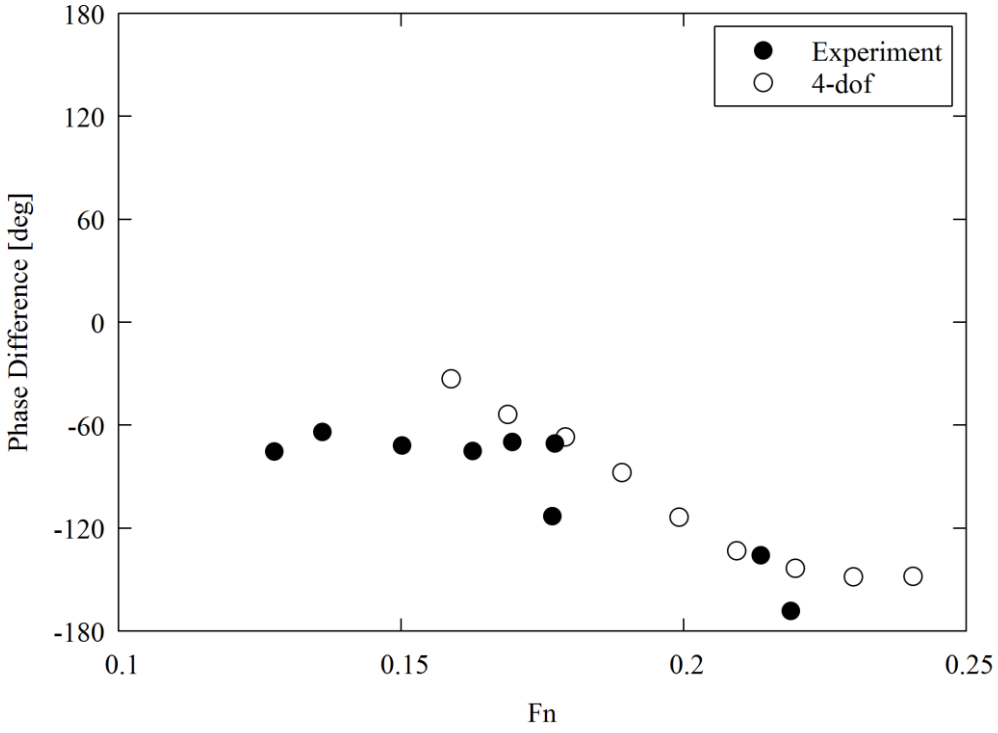

Figure 4.6.2.2 Phase difference of maximum roll angle from a trough of the incident wave.

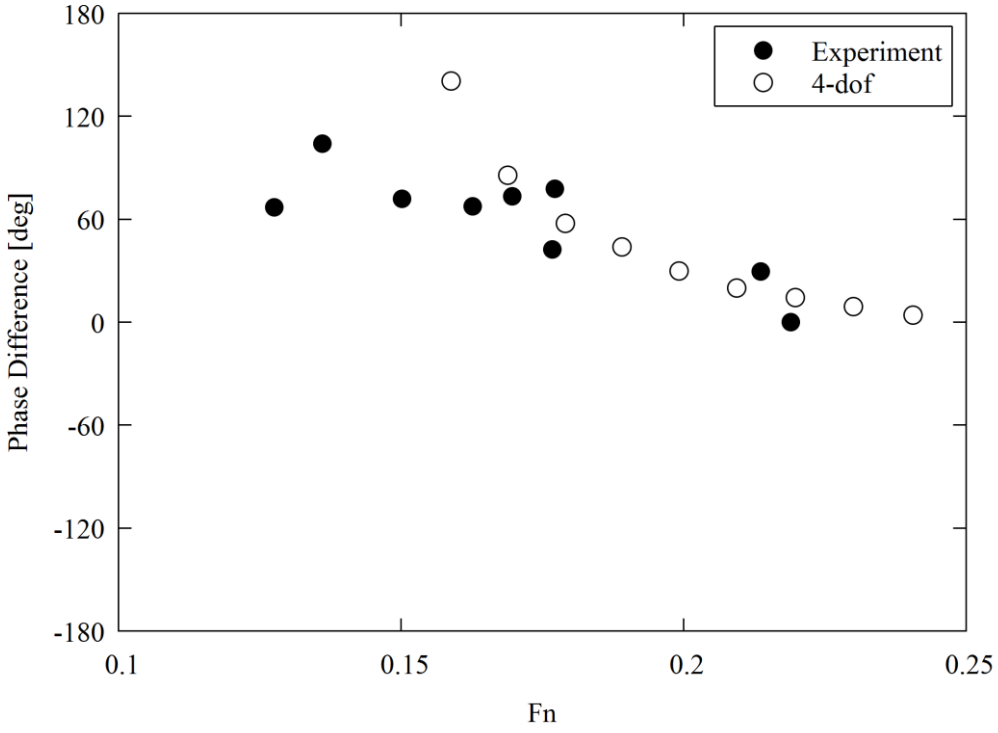

Figure 4.6.2.3 Phase difference of minimum roll angle from a trough of the incident wave.

4.7 Conclusions

The 2:*n* parametric roll is investigated by model experiment and numerical simulation. The 2:*n* parametric roll ($n > 2$) does not occur in the experiment; instead, pure loss of stability is observed in Mathieu's unstable regions for 2:*n* parametric roll ($n > 2$). This indicates that the ship roll motion with relatively high ship speed is governed by manoeuvring equation instead of Mathieu's equation. Then, 4-dof model proposed by Kubo et al. (2012) is used to reproduce the experiment, and it can estimate roll motion in a higher speed case. This supports that the parametric roll and pure loss of stability have different mechanism. However, the 4-dof model, which is based on manoeuvring model, cannot explain the 2:2 parametric roll observed in the experiment due to lack of frequency-based hydrodynamic forces. To more precisely investigate roll responses in following waves, a numerical simulation that takes frequency-based and manoeuvring-based forces into account should be used in the future. Further, the danger of 2:2 parametric roll in quartering waves that is mentioned Vilensky (1995) is also remaining stability problem.

CHAPTER 5 CONCLUSIONS

In this dissertation, parametric roll, which is one of the dynamic ship instability problems, is discussed from following three viewpoints: approximate analytical estimation by using an averaging method; parametric roll estimation at low speed in oblique waves; effect of variation frequency in wide encounter frequency region in following waves. These results could contribute to discussion on the new second generation intact stability criteria, which is almost ready for their trial period from 2021.

In chapter 2, averaging methods are applied to the 1-dof parametric roll model proposed by Umeda et al. (2004), and the usefulness of the approximate analytical approaches on a design stage is shown. There are two aspects of utilization of averaging methods: improvement of accuracy and design criteria. For the first aspect, averaging methods are applied by considering following three effects: 1) superharmonic components; 2) actual GZ curve in calm water; 3) vertical motions. Then, following remarks are concluded:

1) Adding superharmonic components to the assumed form of solution in the averaging method improves the estimation accuracy;

2) The effect of calm-water GZ on parametric roll response is revealed;

3) Taking account of linearly-estimated vertical motions resolves overestimation of the model experiment especially around low speed region.

For the second aspect, 4) the way to estimate the critical ship speed for parametric roll is proposed by using the averaged equation proposed by Umeda et al. (2004) and its partial derivative with a ship speed; 5) the simplification related to the wave encounter frequency in the second check of the level 2 of the second generation intact stability criteria for parametric roll is compared with more rigorous method, which is based on the mean encounter frequency obtained from Grim's effective wave spectrum. Then, following remarks are concluded:

4) The critical ship speed for parametric roll can be estimated by using averaging method;

5) The wave encounter frequency used in the draft second check is verified, and the number of samples of operational conditions should be at least 24.

In chapter 3, for more precise estimation for parametric roll in oblique waves, the heave-roll-pitch coupled 3-dof model (Hashimoto & Umeda, 2010) is expanded to the 5-dof model by adding sway and yaw. Thus, the frequency-based model is combined to the low-speed manoeuvring model. Further, the 5-dof model is validated with the model experiment. As a result, following remarks are concluded:

6) the 5-dof model can reproduce the free running model experiment qualitatively but there are still some quantitative discrepancies. The main reason of the discrepancy may be the estimation of the low-speed manoeuvring motion in waves.;

7) While substituting experimentally observed manoeunvring motions into the 5-dof model a little improves the accuracy of the estimated roll amplitude, the model still overestimates the experiment.

As a result of the validation, it can be said that the new suggestion for the future works are clearly shown although there appears to be more difficulties to be resolved especially related to manoeuvring motion at low speed.

In chapter 4, the 2:*n* parametric roll is experimentally and numerically investigated. Here, the free running model experiment was conducted by increasing the propeller revolution number in regular following waves. Further, the experimental results are compared with numerically estimated roll motion based on the nonlinear Mathieu equation and 4-dof manoeunvring based model (Kubo et al., 2012). As a result, following remarks are concluded:

8) 2:2 parametric roll was observed in the model experiment but 2:*n* parametric roll ($n > 2$) was not observed;

9) Pure loss of stability occurred in high speed region instead of 2:*n* parametric roll ($n > 2$);

10) The 2:2 parametric roll and pure loss of stability can be distinguished by the phase differences between roll, pitch, and wave elevation at the centre of gravity;

11) The nonlinear Mathieu equation can estimate the roll response in lower speed cases but not in higher speed cases. By contrast, the 4-dof manoeuvring-based model shows opposite results. This fact supports that the roll responses in lower speed cases are 2:2 parametric roll, and that of higher speed cased are pure loss of stability.

However, the transitions between 2:2 parametric roll and pure loss of stability is still our future task. This is because parametric roll is mainly governed frequency-based forces but pure loss of stability is by manoeuvring-based forces. Hence, a numerical model that takes both frequency-based and manoeuvring-based forces into account should be used.

ACKNOWLEDGEMENTS

Firstly, I would like to express my sincere gratitude to my supervisor Prof. N. Umeda. He continuously supported my bachelor, master, and Ph.D. studies and related researches. Furthermore, he gave me a lot of opportunities to have valuable experiences such as domestic and international conferences. I could not have imagined having a better supervisor.

Besides my supervisor, I would like to thank Dr. A. Maki, the associate professor of the laboratory I belong to. He gave me precious opinion related to my researches. Also, I would like to thank the rest of my dissertation committee Prof. K. Iijima for his insightful comments.

I would like to thank Mr. A. Matsuda and Dr. D. Terada for helping model experiments at the National Research Institute of Fisheries Engineering. I am grateful for the useful guidance on numerical modelling from Prof. H. Hashimoto. Also, I would like to thank my labmates for stimulating discussion.

This work was supported by a Grants-in-Aid for Scientific Research from the Japan Society for the Promotion of Science (JSPS KAKENHI Grant No. 24360355 and 15H02327) and Fundamental Research Developing Association for Shipbuilding and Offshore (REDAS). It was partly carried out as a research activity of Goal-based Stability Criteria Project of Japan Ship Technology Research Association in the fiscal years of 2013 and 2016 funded by the Nippon Foundation.

Lastly, I would like to thank my parents, grandparents and sister for supporting me throughout writing this dissertation and my life in general.

APPENDIX SUBJECT SHIPS

A.1 Introduction

For the sake of validation study, captive and free-running experiment with several ship models are introduced in this dissertation. The experiments were conducted at the towing tank of Osaka University or seakeeping and manoeuvring basin of National Research Institute of Fisheries Engineering (NRIFE) based on the ITTC recommended procedure for intact stability model tests (ITTC, 2008). Roll, pitch, and yaw motions were observed by using a fiber optical gyroscope. In free running experiment, the ship position was observed by using a total station system. The ships were propelled with an electric motor, the propeller RPM were controlled to be constant, and the auto-pilot course keeping was used with a certain rudder gain.

In this appendix, principal particulars, damping coefficients, and restoring coefficients of subject ships are shown. The subject ships were following four ships: a C11-class post Panamax container ship, ITTC A-1 container ship, ONR flare topside vessel, and pure car career. The linear roll damping coefficient is derived by using Ikeda's simplified method (Kawahara et al., 2012) with the lift component of Ikeda's original method (Ikeda, 2004). Its linear component a is divided into the two components; one is ship-speed-independent and another is proportional to the ship speed U as Eq. A.1.1:

$$a = B_{44}\left(\phi_{am} = 1^\circ\right) = a_0 + a_1 U \,, \tag{A.1.1}$$

where $B_{44}(\phi_{am})$ is the Ikeda's roll damping with an amplitude of ϕ_{am} and natural roll frequency. The roll damping is expressed as the sum of linear term and cubic term in this study and it was accepted in the draft second check of the level 2 for parametric roll in the second generation intact stability criteria. The linear roll damping component is estimated as the Ikeda's roll damping coefficient with an amplitude of 1° and natural roll frequency. The cubic damping is estimated as Eq. A.1.2:

$$c = \frac{B_{44}\left(\phi_{am} = 25^\circ\right) - B_{44}\left(\phi_{am} = 1^\circ\right)}{\left(\frac{25\pi}{180}\right)^2} \,. \tag{A.1.2}$$

Since the a_1 is independent of the amplitude in the Ikeda's original method, the cubic component is a ship-speed-independent term. The roll damping coefficients α and γ are as Eq. A.1.3-4:

$$\alpha = \frac{2}{T_\phi} a = \frac{2}{T_\phi}\left(a_0 + a_1 U\right) = \alpha_0 + \alpha_1 U \,, \tag{A.1.3}$$

$$\gamma = \frac{4 T_\phi}{3\pi^2} c \,. \tag{A.1.4}$$

A.2 C11-Class Post-Panamax Container Ship

Towing model experiment was conducted with a C11-class post-Panamax container ship by

Hashimoto and Umeda (2010). In the experiment, the loading condition of MARIN's experiment was used (Levadou & van't Veer, 2006). On the other hand, the loading condition when she suffered parametric roll in actual seas (France et al., 2003) is a little different. Table A.2.1 shows principal particulars of both loading conditions. The estimated roll damping coefficients and coefficients of polynomial approximation of calm-water GZ curves are shown in Tab. A.2.2. The linear roll damping coefficient is divided into two components that is proportional to the ship speed and that is ship-speed-independent term as Eq. A.1.3. The body plan is shown in Fig. A.2.1 and the calm-water GZ curve is compared with its polynomial fitting in Fig. A.2.2.

Table A.2.1 Principal particulars of the C11-class post-Panamax container ship.

Item	MARIN	ACCIDENT	Unit
Length: L_{pp}	262.0		m
Breadth: B	40.0		m
Draught: d	11.5	12.34	m
Service speed: V_s	23.6	25.0	knot
trim	0.0		m
Metacentric height: GM	1.965		m
Natural roll period: T_ϕ	25.1	25.7	s
Block coefficient: C_b	0.5511	0.576	
Midship section coefficient: C_m	0.9573	0.962	
Ration of gravitational centre height: OG/d	-0.6764	-0.489	
Bilge keel length ratio: L_{bk}/L_{pp}	0.292		
Bilge keel breadth ratio: B_{bk}/B	0.01		

Table A.2.2 Coefficients of roll damping and calm-water GZ curve of the C11-class post-Panamax container ship.

Item	MARIN	ACCIDENT	Unit
Ship-speed-independent component of linear roll damping: α_0	1.872×10^{-3}	1.632×10^{-3}	s^{-1}
Coefficient of linear component of linear roll damping: α_1	1.576×10^{-4}	1.407×10^{-4}	m^{-1}
Cubic damping coefficient: γ	4.260	3.917	s
Cubic restoring coefficient: l_3	0.3500	0.5716	
Quintic restoring coefficient: l_5	-0.7721	-1.163	

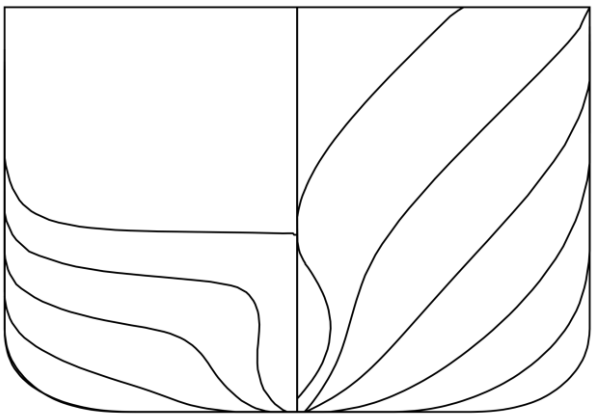

Figure A.2.1 Body plan of the C11-class post-Panamax conatiner ship.

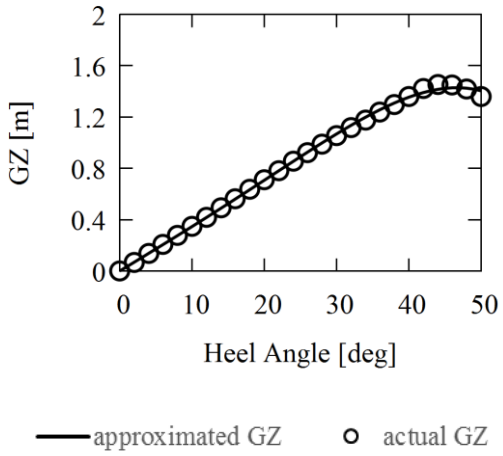

Figure A.2.2 Calm-water GZ curve and its polunomial fitting of the C11-class post-Panamax conatainer ship.

A.3 ITTC A-1 Container Ship

Free running model experiment was conducted with an ITTC A-1 container ship by Umeda et al. (2008). The principal particulars are shown in Tab. A.3.1 and the estimated roll damping coefficients and coefficients of polynomial approximation of calm-water GZ curves are shown in Tab. A.3.2. The body plan is shown in Fig. A.3.1 and the calm-water GZ curve is compared with its polynomial fitting in Fig. A.3.2.

Table A.3.1 Principal particulars of the ITTC A-1 container ship.

Item	ITTC A-1 container ship	Unit
Length: L_{pp}	150.0	m
Breadth: B	27.2	m
Draught: d	8.5	m
Service speed: V_s	23.0	knot
trim	0.0	m
Metacentric height: GM	1.000	m
Natural roll period: T_ϕ	20.1	s
Block coefficient: C_b	0.6672	
Midship section coefficient: C_m	0.9841	
Ration of gravitational centre height: OG/d	-0.2512	
Bilge keel length ratio: L_{bk}/L_{pp}	0.250	
Bilge keel breadth ratio: B_{bk}/B	0.0201	

Table A.3.2 Coefficients of roll damping and calm-water GZ curve of the ITTC ship A-1 container ship.

Item	ITTC A-1 container ship	Unit
Ship-speed-independent component of linear roll damping: α_0	3.954×10^{-3}	s^{-1}
Coefficient of linear component of linear roll damping: α_1	2.310×10^{-4}	m^{-1}
Cubic damping coefficient: γ	4.871	s
Cubic restoring coefficient: l_3	3.196	
Quintic restoring coefficient: l_5	-5.655	

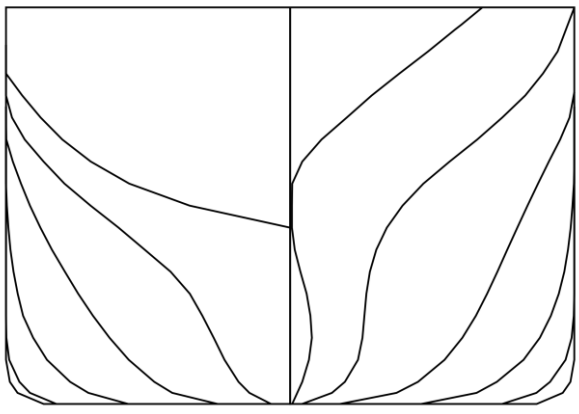

Figure A.3.1 Body plan of the ITTC A-1 conatiner ship.

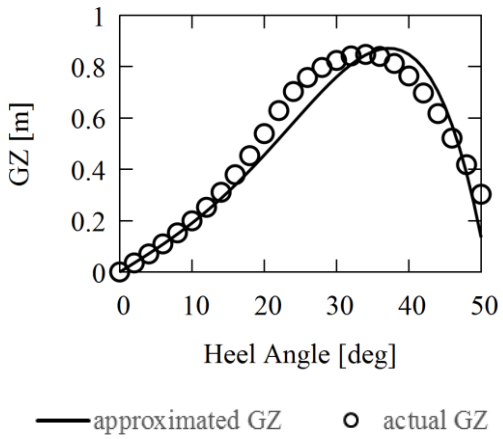

Figure A.3.2 Calm-water GZ curve and its polynomial fitting of the ITTC A-1 contianer ship.

A.4 ONR Flare Topside Vessel

Free running model experiment was conducted with an ONR flare topside vessel. The principal particulars are shown in Tab. A.4.1 and the estimated roll damping coefficients and coefficients of polynomial approximation of calm-water GZ curves are shown in Tab. A.4.2. The values of C_m and B_{bk}/B are out of the fitting range of Ikeda's simplified method, so that the roll damping coefficients in Tab. A.4.2 are estimated by setting C_m to 0.90 and B_{bk}/B to 0.06. The body plan is shown in Fig. A.4.1 and the calm-water GZ curve is compared with its polynomial fitting in Fig. A.4.2.

Table A.4.1 Principal particulars of the ONR flare topside vessel.

Item	ONR flare topside vessel	Unit
Length: L_{pp}	154.0	m
Breadth: B	18.8	m
Draught: d	5.42	m
Service speed: V_s	26.44	knot
trim	0.0	m
Metacentric height: GM	0.7735	m
Natural roll period: T_ϕ	20.84	s
Block coefficient: C_b	0.5695	
Midship section coefficient: C_m	0.8579 (0.90)	
Ration of gravitational centre height: OG/d	-0.747	
Bilge keel length ratio: L_{bk}/L_{pp}	0.3483	
Bilge keel breadth ratio: B_{bk}/B	0.0707 (0.06)	

Table A.4.2 Coefficients of roll damping and calm-water GZ curve of the ONR flare topside vessel.

Item	ONR flare topside vessel	Unit
Ship-speed-independent component of linear roll damping: α_0	7.126×10^{-3}	s^{-1}
Coefficient of linear component of linear roll damping: α_1	2.357×10^{-4}	m^{-1}
Cubic damping coefficient: γ	10.41	s
Cubic restoring coefficient: l_3	-0.5552	
Quintic restoring coefficient: l_5	1.311	

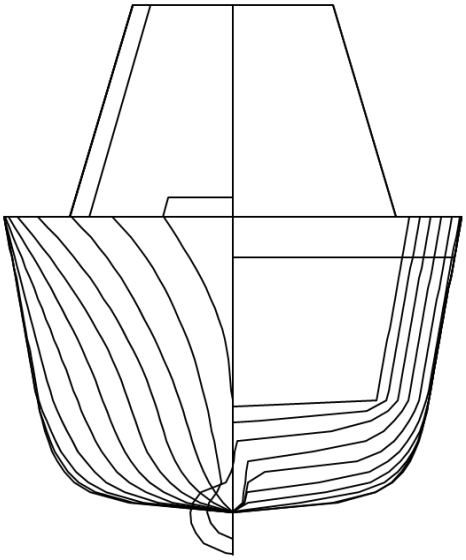

Figure A.4.1 Body plan of the ONR flare topside vessel.

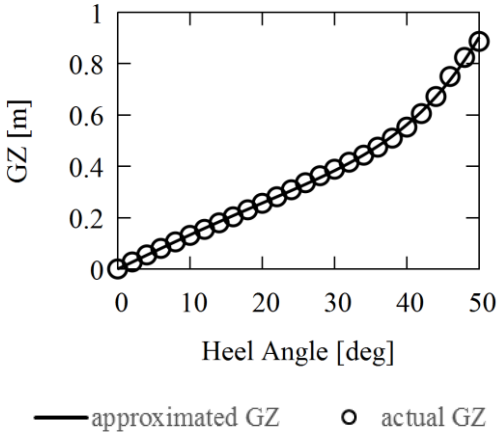

Figure A.4.2 Calm-water GZ curve and its polynomial fitting of the ONR flare topside vessel.

A.5 Pure Car Carrier

Free running model experiment was conducted with a pure car carrier. The principal particulars

are shown in Tab. A.5.1. Yoshimura et al. (1986) conducted low-speed manoeuvring test with a similar pure car carrier, so that the manoeuvring hull, rudder, and propeller thrust coefficients estimated Yoshimura et al. (1986) are used and the values are shown in Tab. A.5.2. The body plan and GZ curve are not available due to a commercial reason.

Table A.5.1 Principal particulars of the pure car carrier.

Item	Pure car carrier	Unit
Length: L_{pp}	180.0	m
Breadth: B	32.20	m
Draught: d	8.2	m
trim	0.0	m
Metacentric height: GM	1.27	m
Natural roll period: T_{ϕ}	23.4	s

Table A.5.2 Manoeuvring hull, rudder, and propeller coefficients of the similar pure car career (Yoshimura et al., 1986).

Item	Pure car carrier	Unit
X_{vv}'	-0.0368	
X_{vr}'	0.140	
X_{rr}'	0.0125	
X_{vvvv}'	0.469	
X_{vvvr}'	-0.11	
Y_v'	-0.2629	
Y_r'	0.0381067	
Y_{vvv}'	-1.55	
Y_{vvr}'	-0.655	
Y_{vrr}'	-0.738	
Y_{rrr}'	-0.0566	
N_v'	-0.0977	
N_r'	-0.0505	
N_{vvv}'	-0.173	
N_{vvr}'	-0.627	
N_{vrr}'	-0.0954	
N_{rrr}'	-0.0353	
l_P'	-0.49	
l_R'	-0.811	
$1-w_P$	0.640	
$1-t_P$	0.838	
a_H	$0.283 + 0.263\ J_P$	
x_H'	-0.467	
ε	1.170	
κ_P	0.513	
$K_T(J)$	$0.3304 - 0.2299\ J - 0.1617\ J^2$	

REFERENCE LIST

Abicht, W. (1975) On Capsizing of Ships in Regular and Irregular Seas. *Proceedings of the 1st International Stability of Ships and Ocean Vehicles*, 159-179.

Bhattacharyya, R. (1978). *Dynamics of marine vehicles*. John Wiley & Sons Inc.

Blocki, W. (1980). Ship Safety in Connection with Parametric Resonance of the Roll. *International Shipbuilding Progress*, *27*(306), 36-53.

Boroday, I.K. (1990). Ship Stability in Waves: On the Problem of Righting Moment Estimations for Ships in Oblique Waves. *Proceedings of the 4th International Conference on Stability of Ships and Ocean Vehicles*, 441-451.

Bulian, G. (2004). Approximate Analytical Response Curve for a Parametrically Excited Highly Nonlinear 1-DOF System with an Application to Ship Roll Motion Prediction. *Nonlinear Analysis: Real World Applications*, *5*(4), 725-748.

Cardo, A., Ceschia, M., Francescutto, A., and Nabergoj, R. (1980). Effects of the angle-dependent damping on the rolling motion of ships in regular beam seas. *International Shipbuilding Progress*, *27*, 135-138.

Cardo, A., Francescutto, A., amd Nabergoj, R. (1981). Ultraharmonics and subharmonics in the rolling motion of a ship: steady-state solution. *International Shipbuilding Progress*, *28*(326), 234-251.

Cardo, A., Francescutto, A., and Nabergoj, R. (1984). Nonlinear rolling response in a regular sea. *International shipbuilding progress*, *31*(360), 204-206.

Danish Maritime Accident Investigation Board. (2014). Marine Accident Report September 2014.

de Kat, J. O. and Paulling, J. R. (1989). The Simulation of Ship Motions and Capsizing in Severe Seas. *SNAME transactions*, *97*, 139-168.

de Kat, J. O., & Paulling, J. R. (2001). Prediction of extreme motions and capsizing of ships and offshore marine vehicles. *Proceedings of OMAE 2001-20th Conference on Offshore Mechanics and Arctic Engineering*.

France, W. N., Levadou, M., Treakle, T. W., Paulling, J. R., Michel, R. K. and Moore, C. (2003). An Investigation of Head-Sea Parametric Rolling and its Influence on Container Lashing System. *Marine Technology*, *40*(1), 1-19.

Francescutto, A. (2001). An Experimental Investigation of Parametric Rolling in Head Waves. *Journal of Offshore Mechanics and Arctic Engineering*, *123*(2), 65-69.

Fukasawa, T. (1990). On the Numerical Time Integration Method of Nonlinear Equations for Ship Motions and Wave Loads in Oblique Waves. *Journal of the Society of Naval Architects of*

Japan, *167*, 69-79. (in Japanese).

Grim, O. (1952). Rollschwingungen, Stabilitat und Sicherheit im Seegang. *Schiffstechnik*, *1*, 10-21. (in German).

Grim, O. (1961). Beitrag zu dem Problem der Sicherheit des Schiffes in Seegang. *Schiff und Hafen*, *6*, 490-497. (in German).

Hamamoto, M. and Akiyoshi, T. (1988). Study on Ship Motions and Capsizing in Astern Seas -1st Report-. *Journal of the Society of Naval Architects of Japan*, *179*, 77-87.

Hashimoto, H., and Umeda, N. (2004). Nonlinear analysis of parametric rolling in longitudinal and quartering seas with realistic modeling of roll-restoring moment. *Journal of Marine Science and Technology*, *9*(3), 117-126.

Hashimoto, H., Umeda, N., Ogawa, Y., Taguchi, H., Iseki, T., Bulian, G., Toki, N., Ishida, S., and Matsuda, A. (2008). Prediction Methods for Parametric Rolling with Forward Velocity and Their Validation –Final Report of SCAPE Committee (Part 2)-. *Proceedings of the sixth Osaka Colloquium on Seakeeping and Stability of Ships* (*OC 2008*), 265-275.

Hashimoto, H. and Umeda, N. (2010). A Study on Quantitative Prediction of Parametric Roll in Regular Waves. *Proceedings of the 11th International Ship Stability Workshop* (*ISSW2010*), 295-301.

Hayashi, C. (1985). *Nonlinear oscillations in physical systems*. Princeton University Press.

Hua, J., Palmquist, M. and Lindgren, G. (2006) An Analysis of the Parametric Roll Events Measured Onboard the PCTC AIDA. *Proceedings of the 9th International Stability of Ships and Ocean Vehicles*, 109-118.

Ikeda, Y., Himeno, Y., and Tanaka, N. (1978). A Prediction Method for Ship Roll Damping, *DNAUOP Report 405*.

Ikeda, Y. (2004). Prediction Methods of Roll Damping of Ships and Their Application to Determine Optimum Stabilization Devices. *Marine Technology*, *41*(2), 89-93.

Ikeda, Y., Umeda, N., Shin, C., Naito, S. (2013). *Naval Architecture and Ocean Engineering Series Vol. 5, Ship Motion: Seakeeping, Basic Edition*. Seizando-Shoten Publishing co., Ltd. (in Japanese).

IMO. (2015). Report of the working group (part 1). *SDC 2/WP.4*

IMO. (2016). Report of the working group (part 1). *SDC 3/WP.5*.

Ito, Y., Umeda, N., and Kubo, H. (2014). Hydrodynamic Aspects on Vulnerability Criteria for Surf-Riding of Ships. *Jurnal Teknologi (Sciences & Engineering)*, *66*(2), 127-132.

ITTC. (2008). Recommended Procedures, Model Tests on Intact Stability. 7.5-02-07-04.

Kan, S., Saruta, T., Taguchi, H., Yasuno, M. (1990). Capsizing of a Ship in Quartering Seas (Part 1.

Model Experiments on Mechanism of Capsizing). *Journal of the Society of Naval Architects of Japan*, *167*, 81-90. (in Japanese)

Kawahara, Y., Maekawa, K. and Ikeda, Y. (2012) A Simple Prediction Formula of Roll Damping of Conventional Cargo Ships on the Basis of Ikeda's Method and Its Limitation. *Journal of Shipping and Ocean Engineering*, *2*(4), 201-210.

Kerwin, J. E. (1955). Notes on Rolling in Longitudinal Waves. *International Shipbuilding Progress*, *2*(16), 597-614.

Kobylinski, L. (1975). Rational Stability Criteria and Probability of Capsizing. *Proceedings of the 1st International Stability of Ships and Ocean Vehicles*, 48-60.

Krappinger, O. (1975). Stability of Ships and Modern Safety Concepts. *Proceedings of the 1st International Stability of Ships and Ocean Vehicles*, 27-30.

Krylov, N.M., Bogoliubov N.N. (1947). *Introduction to Non-Linear Mechanics*. Princeton Univ. Press. (Translated from Russian).

Kubo, H., Umeda, N., Yamane, K., and Matsuda, A. (2012). Pure Loss of Stability in Astern Seas – Is it Really Pure?-. *the 6th Asia-Pacific Workshop on Marine Hydrodynamics.* 307-312.

Kubo, H. (2012). Designing New Generation Intact Stability Criteria on Pure Loss of Stability in Astern Seas. *Master thesis*.

Lee, C. M. and Kim, K. H. (1982). Prediction of motion of ships in damaged condition in waves. *Proceedings of 2nd International Conference on Stability of Ships and Ocean Vehicles*, 287-301.

Levadou, M. and van't Veer, R. (2006). Parametric Roll and Ship Design. *Proceedings of the 9th International Conference of Ships and Ocean Vehicles*, 191-206.

Lloyd's Register. (2018). Lloyd's List Intelligence Casualty Statistics.

Maki, A., Umeda, N., Shiotani, S. and Kobayashi, E. (2011). Parametric Rolling Prediction in Irregular Seas Using Combination of Deterministic Ship Dynamics and Probabilistic Wave Theory. *Journal of Marine Science and Technology*, *16*, 294-310.

Motora, S. (1959). On the Measurement of Added Mass and Added Moment of Inertia for Ship Motions. *Journal of the Society of Naval Architects of Japan*, *105*, 83-92. (in Japanese).

Motora, S. (1960a). On the Measurement of Added Mass and Added Moment of Inertia for Ship Motions (Part 2. Added Mass Abstract for the Longitudinal Motions). *Journal of the Society of Naval Architects of Japan*, *106*, 59-62. (in Japanese).

Motora, S. (1960b). On the Measurement of Added Mass and Added Moment of Inertia for Ship Motions (Part 3. Added Mass for the Transverse Motions). *Journal of the Society of Naval Architects of Japan*, *106*, 63-68. (in Japanese).

Morimoto, A. (2012). Prediction of Parametric Roll in Oblique Waves. *Bachelor thesis*.

Nayfeh, A. H., and Khdeir, A. A. (1986a). Nonlinear rolling of ships in regular beam seas. *International shipbuilding progress*, *33*(379), 40-49.

Nayfeh, A. H., and Khdeir, A. A. (1986b). Nonlinear rolling of biased ships in regular beam waves. *International Shipbuilding Progress*, *33*(381), 84-93.

Neves, M.A.S. and Valerio, L. (2000) Parametric Resonance in Waves of Arbitrary Heading. *Proceedings of the 7th International Conference on Stability and Operational Safety of Ships and Ocean Vehicles*, 680-687.

Neves, M. A. S. and Rodriguez, C. A. (2006). On Unstable Ship Motions Resulting from Strong Non-Linear Coupling. *Ocean Engineering*, *33*, 1853-1883.

Ogawara, Y. and Miura, M. (1960) An experimental Study on the Rolling of Ships in Longitudinal Waves, *The Society of Naval Architects of Japan, 60th Anniversary Series*, *6*, 139-145.

Paulling, J. R. and Rosenberg, R., M. (1959). On unstable ship motions resulting from nonlinear coupling. *Journal of Ship Research*, *3*, 36-46.

Paulling, J. R., Kastner, S., and Schaffran, S. (1972). Experimental studies of capsizing of intact ships in heavy seas. *Report Department of Naval Architecture, University of California, Berkley*.

Reed, A.M. (2011). 26th ITTC Parametric Roll Benchmark Study. *Proceedings of the 12th International Ship Stability Workshop*, 195-204.

Sadat-Hosseini, H., Stern, F., Olivieri, A., Campana, E. F., Hashimoto, H., Umeda, N., Bulian, G., and Francescutto, A. (2010). Head-wave parametric rolling of a surface combatant. *Ocean Engineering*, *37*(10), 859-878.

Salvesen, N., Tuck, E.O. and Faltinsen, O. (1970). Ship Motions and Sea Loads. *Transaction of the Society of Naval Architects and Marine Engineers*, *78*, 250-287.

Sanchez, N. E. and Nayfeh, A. H. (1990a). Prediction of Bifurcations in a Parametrically Excited Duffing Oscillator. *International Journal of Non Linear Mechanics*, I(2), 163-176.

Sanchez, N.E. and Nayfeh, A.H. (1990b). Rolling of Biased Ships in Quartering Seas. *Proceedings of the 18th Symposium on Naval Hydrodynamics*, 133-140.

Sato, C. (1977). *Nonlinear Oscillation Theory*. Asakura Publishing co., Ltd. (in Japanese).

Shin, Y. S., Belenky, V. L., Lin, W. M., Weems, K. M., and Engle, A. H. (2003). Nonlinear Time Domain Simulation Technology for Seakeeping and Wave-Load Analysis for Modern Ship Design. *Transactions – Society of Naval Architects and Marine Engineers*, *111*, 557-578.

Soliman, M. S., and Thompson, J. M. T. (1992). Indeterminate sub-critical bifurcations in parametric resonance. *Proc. R. Soc. Lond. A*, *438*(1904), 511-518.

Spanos, D. and Papanikolaou A. (2009). SAFEDOR International Benchmark Study on Numerical Simulation Methods for the Prediction of Parametric Rolling of Ships in Wave. *Proceedings of the 10th International Conference on Stability of Ship and Ocean Vehicles*, 627-636.

Spyrou, K. J. (2000). Designing against parametric instability in following seas. *Ocean Engineering*, *27*(6), 625-653.

Spyrou, K. J. (2005). Design criteria for parametric rolling. *Oceanic Engineering International*, *9*(1), 11-27.

Taguchi, H. (2006). Model Experiment on Parametric Rolling of a Post-Panamax Containership in Head Waves. *Proceedings of the 9th International Conference on Stability of Ships and Ocean Vehicles*, 147-156.

Takaishi, Y. and Kuroi M. (1977). Practical Calculation Method of Ship Motions in Waves. *Proceedings of the 2nd Seakeeping Symposium, The Society of Naval Architects of Japan*, 109-133. (in Japanese).

United Nations Conference on Trade and Development. (2018). Review of Maritime Transport 2018.

Umeda, N., Hashimoto, H., Frederick, S., Nakamura, S., Sadat-Hosseini, H., Matsuda, A. and Carrica, P. (2008). Comparison Study on Numerical Prediction Techniques for Parametric Roll. *Proceedings of twenty seventh Symposium on Naval Hydrodynamics, Office of Naval Research*, 201-213.

Umeda, N., Hashimoto, H., Takaishi, Y., Chiba, Y., Matsuda, A., Sera, W., Suzuki, S., Spyrou, K. J., Watanabe, K. (1995a). Model Experiments of Ship Capsize in Astern Seas. *Journal of the Society of Naval Architects of Japan, 177*, 207-217.

Umeda, N., Hashimoto, H., Vassalos, D., Urano, S., Okou, K. (2004). Nonlinear Dynamics on Parametric Roll Resonance with Realistic Numerical Modelling. *International Shipbuilding Progress, 51*(2), 205-220.

Umeda, N. and Yamakoshi Y. (1989). Hydrodynamic Forces Acting on a Longitudinally Non-symmetric Ship Under Manoeuvring at Low Speed. *Journal of the Kansai Society of Naval Architects*, *211*, 127-137. (in Japanese).

Umeda, N., Yamakoshi, Y. (1992). 6. Probability of Ship Capsizing due to Pure Loss of Stability in Quartering Seas. *Naval architecture and ocean engineering*, *30*, 73-85.

Umeda, N., Yamakoshi, Y., and Suzuki, S. (1995b). Experimental Study for Wave Forces on a Ship Running in Quartering Seas with Very Low Encountering Frequency. *Proceedings of The Sevastianov Symposium, The International Symposium Ship Safety in a Seaway, Kaliningrad, Russia, The Kyrlov Ship Research Institute, 1995, 1*, I4.

Urabe, M. (1965). Galerkin's Procedure for Nonlinear Periodic System. *Archive for Rational Mechanics and Analysis, 20*(2), 120-152.

Van der Pol, B. (1926). LXXXVIII. On "Relaxation-Oscillations". *The London, Edinburgh, and Dublin Philosophical Magazine and Journal of Science*, *2*(11), 978-992.

Vilensky, G. V. (1995). Dangerous rolling regimes in following and quartering seas. *Proceedings of international symposium ship safety in a seaway: stability, manoeuvrability, nonlinear approach in memory of Professor Sevastianov*, 2, 7.

Watanabe, Y. (1934). On the Dynamical Properties of the Transverse Instability of a Ship due to Pitching. *Journal of the Society of Naval Architects of Japan*, *5*3, 51-70. (in Japanese)

Yoshimura, Y. (1986). Mathematical Model for the Manoeuvring Ship Motion in Shallow Water. *The Japan Society of Naval Architects and Ocean Engineers*, *200*, 41-51. (in Japanese).

Yoshimura, Y., Nakao, I. and Ishibashi, A. (2009). Unified Mathematical Model for Ocean and Harbour Manoeuvring, *Proceedings of MARSIM2009*, 116-124.

AUTHOR'S PAPER RELATED TO THIS DISSERTATION

Umeda, N., Sakai, M., Fujita, N., Morimoto, A., Terada, D., and Matsuda, A. (2016). Numerical Prediction of Parametric Roll in Oblique Waves. *Ocean Engineering, 120,* 212-219. (https://doi.org/10.1016/j.oceaneng.2016.05.014)

Sakai, M., Umeda, N., Terada, D., and Matsuda, A. (2017). The Relationship between Parametric Roll Regions and Pure Loss of Stability. *Proceedings of Annual Autumn Meeting of the Japan Society of Naval Architects and Ocean Engineers 2017,* 291-294.

Sakai, M., Umeda, N., Yano, T., Maki, A., Yamashita, N., Matsuda, A., and Terada, D. (2018). Averaging Methods for Estimating Parametric Roll in Longitudinal and Oblique Waves. *Journal of Marine Science and Technology*, *23*(3), 413-424. (https://doi.org/10.1007/s00773-017-0490-6)

Sakai, M., Umeda, N., and Maki, A. (2018), Encounter Frequency Effect on the Simplified Design Criteria against Parametric Roll. *Proceedings of the 13th International Conference of Stability of Ships and Ocean Vehicles*, 252-260.